STRUCTURE AND PROPERTIES OF LITHIUM ION CONDUCTORS IN THE Li_2O-Y_2O_3-ZrO_2 SYSTEM

STRUCTURE AND PROPERTIES OF LITHIUM ION CONDUCTORS IN THE Li_2O-Y_2O_3-ZrO_2 SYSTEM

by

YUN ZOU, B.Sc., M.Sc.

A Thesis
Submitted to the School of Graduate Studies
in Partial Fulfilment of the Requirements
for the Degree
Master of Engineering

McMaster University
June, 1993

MASTER OF ENGINEERING (1993)
(Materials Engineering)

McMASTER UNIVERSITY
Hamilton, Ontario

TITLE: Structure and Properties of Lithium Ion Conductors in the Li_2O-Y_2O_3-ZrO_2 System

AUTHOR: Yun Zou, B.Sc. (Wuhan University of Technology, China)
M.Sc. (Wuhan University of Technology, China)

SUPERVISOR: Professor Anthony Petric

NUMBER OF PAGES: xv, 127

ABSTRACT

Ceramic samples of $Li_{2+x}Y_xZr_{1-x}O_3$ with x=0 to 0.1, $Li_{8+x}Y_xZr_{1-x}O_6$ with x=0 to 0.2, $Li_{1-x}Y_xZr_{1-x}O_2$ with x=0 to 0.5 and $Li_{1+x}Zr_xY_{1-x}O_{2+x}$ with x=0 to 0.3 were prepared via conventional solid reactions. The solubilities, crystal structures and microstructures in these samples were studied by x-ray diffraction(XRD), infrared spectra, differential thermal analysis(DTA) and scanning electron microscopy(SEM). The results show that the solubilities are $0.05 \le X < 0.1$ for $Li_{2+x}Y_xZr_{1-x}O_3$ and $Li_{8+x}Y_xZr_{1-x}O_6$, $0.1 \le x < 0.15$ for $Li_{1-x}Y_xZr_{1-x}O_2$, and $x \ge 0.3$ for $Li_{1+x}Zr_xY_{1-x}O_{2+x}$, respectively. The crystal structures of the solid solutions of $Li_{2+x}Y_xZr_{1-x}O_3$ and $Li_{8+x}Y_xZr_{1-x}O_6$ are the same as Li_2ZrO_3 and Li_8ZrO_6, respectively but the cell constants change slightly with x, while the structure of $Li_{1-x}Y_xZr_{1-x}O_2$ and $Li_{1+x}Zr_xY_{1-x}O_{2+x}$ changes from monoclinic for pure $LiYO_2$(x=0) to tetragonal($x \ge 0.005$). The sinterability of Li_2ZrO_3 improves greatly with yttrium additions to Li_2ZrO_3.

The conductivities of the samples were measured by complex impedance spectroscopy and dc polarization. The results show that lithium conductivity in $Li_{2+x}Y_xZr_{1-x}O_3$ samples increases slightly from 3.9×10^{-6} to 5.0×10^{-6} S/cm at 400°C as x

increases from 0 to 0.05 and the corresponding conduction activation energy decreases slightly from 0.99 to 0.92 eV. Based on the effective medium theory, the conductivity increase in the solid solution was estimated to be 3% for x=0.05 compared with pure Li_2ZrO_3 crystal.

For $Li_{8+x}Y_xZr_{1-x}O_6$ samples, a mixture of LiOH and Li_2CO_3, which melts at about 430°C, can be formed during the processing and measurements. The ionic conductivity depends to a large degree on the microstructure(the amount and distribution of the mixture) below 430°C. The lithium conductivity at 435°C increases from $1.0x10^{-2}$ to $6.9x10^{-2}$ S/cm as x increases from 0 to 0.05. The electronic contribution to total conductivity is lower than 1% below 435°C.

The ionic conductivity in the tetragonal phase of Zr-doped $LiYO_2$ is much lower than in pure monoclinic $LiYO_2$. The conductivity values at 500°C are $1.3x10^{-2}$ for pure $LiYO_2$ and $1.2x10^{-4}$ for $Li_{1.3}Zr_{0.3}Y_{0.7}O_{2.3}$. The ionic conduction activation energy in the tetragonal Zr-doped $LiYO_2$ is much higher than pure $LiYO_2$.

The thermal stability and the hydrolysis tendency for Li_2ZrO_3, Li_8ZrO_6 and $LiYO_2$ were examined by thermodynamic calculations and by experiments.

ACKNOWLEDGMENTS

I wish to thank my supervisor, Dr. Anthony Petric, for suggesting the subject considered here and for his continuous guidance, help and encouragement throughout this study. I am indebted to my wife, Shirley, for her limitless help, support and assistance.

Thanks are due to the technical advice and help of the technical staff of the Department of Materials Science and Engineering and Institute of Materials Research. Dr. Kuo's assistance in the conductivity measurements is greatly appreciated. I also wish to thank Dr. Huchun Yi and Mr. Shiwei Guan for their technical assistance and friendship.

Engineering

TABLE OF CONTENTS

LIST OF FIGURES

LIST OF TABLES

CHAPTER 1 INTRODUCTION

The deployment of electric vehicles depends on the development of high energy density batteries with high performance. High energy density batteries also have a potentially important role to play in military, space, stationary storage and remote power sources, as well as industrial and domestic cordless products in the next century. Thus high energy density batteries have been extensively investigated in the past two decades. Of those batteries, lithium batteries have been attractive because of their very high energy density and high cell voltage due to the favourable thermodynamic properties [1,2,3,4]. In the area of lithium rechargeable batteries, research and development work is advancing in two fronts. One area receiving considerable research effort is ambient temperature rechargeable lithium batteries based on organic electrolytes. Organic electrolyte systems have the advantage of ambient temperature operation. However, problems due to dendritic deposition, low ionic conductivity of the media, problems of solvent transport and solubility of cathode active materials often exist. The other area involves high temperature rechargeable lithium/metal sulphide and lithium/sulphur battery systems with molten salt and solid electrolytes. These batteries are basically intended for electric vehicle propulsion, but, energy storage applications are also being investigated. Molten salt and solid electrolyte systems are capable of higher current densities than organic electrolytes, by virtue of their operation at elevated temperature. Molten salt systems suffer from corrosion problems, including that of the separator. Solid electrolytes, on the other hand, act as natural separators, eliminating the problem encountered in molten salts.

In lithium high temperature batteries, the lithium-sulphur battery has become most attractive because of its very high theoretical specific energy of 2600 W-hr/kg, and high emf value of 2.2 V [1, 2, 3]. But, up till now, several practical difficulties have discouraged the development of a practical cell [3-7]. The crucial problems arise from the use of molten salts as electrolytes [4-7]. One possible solution in developing a practical Li/S cell is to find a suitable solid lithium electrolyte. Although a large number of such electrolytes have been studied [8-13], most of them are thermodynamically unstable against pure lithium [8]

However, the lithium zirconates Li_2ZrO_3 and Li_8ZrO_6 and lithium yttrate $LiYO_2$ have been reported to be possible lithium ionic conductors that are thermodynamically stable against pure lithium [8], but their ionic conductivities are low.

In a totally different application, advances in the plasma physics and technology have increased our confidence that fusion can provide a reliable, long-term alternative for abundant, economically attractive energy. One advantage of fusion energy which is of paramount importance is that there is a plentiful, low cost fuel supply. A second important advantage of fusion power is that there are no polluting combustion products and very little radioactive waste. Another advantage is the inherent safety of the fusion plasma. There will be no risk of a nuclear runaway or excursion which could lead to emergency evacuations. Lithium zirconates could be potential tritium breeding blanket materials in a fusion reactor.

Although lithium zirconates and lithium yttrium oxide have relevant applications as discussed above, there has been no systematic research on the preparation and stability of these materials. Also, the conductivities need to be improved in order to justify their use in lithium high temperature batteries. To this end, doping of binary components to form solid solutions of LiO_2-Y_2O_3-ZrO_2 was investigated.

In the present work, the solubilities of yttrium in the Li_2ZrO_3 and Li_8ZrO_6 and zirconium in $LiYO_2$ were determined. The structures of solid solutions of $Li_{2+x}Y_xZr_{1-x}O_3$, $Li_{8+x}Y_xZr_{1-x}O_6$ and $Li_{1-x}Zr_xY_{1-x}O_2$ were studied and their conductivities were measured. The thermal stability and hydrolysis tendencies for these materials were also studied by calculations and by experiments.

CHAPTER 2 LITERATURE REVIEW

2-1 Solid Electrolytes

Solid electrolytes have been investigated by many researchers from battery engineers to theoreticians for several decades. Many solid electrolytes have been discovered, and a wide variety of experimental techniques have been applied to measure the properties of these materials and the theoretical understanding has improved.

Research on ionic conduction in solids, however, can be traced back to the early 19th century when it was ascertained that the relationship between the current passing through various kinds of solids and the accompanying chemical changes obey Faraday's law [14]. Stabilized zirconia, which is one of the present key solid electrolytes used for oxygen sensors and fuel cells, appeared in 1897 as a resistive-heating type light source called the "Nernst glower" [15]. However, a half century passed before a complete understanding of electric conduction phenomena in ionic crystals including zirconia was demonstrated in Wagner's thesis in 1943 [16].

There were, however, several important discoveries regarding ionic conduction phenomena in solids between the Nernst glower and Wagner which mainly concerned alkali halides. Among them, extraordinarily high ionic conductivity in AgI was found by Tubandt et al. [17,18]. They discovered that the conductivity of AgI in the solid state jumps to a value almost the equal to that in the liquid phase when it transforms from the beta to the alpha phase at 149°C. Since then, α-AgI has been studied extensively from various aspects ranging from physics to crystallographic studies. Strock [19] discovered in 1935 that the conductive Ag^+ ions (2 ions per unit cell) are statistically distributed among 42 crystallographically equivalent interstices formed by the cation (Ag^+) lattice analogous to a fused state. Although still controversial in its details, it was thus understood that extraordinarily high Ag^+ conductivity was due to the crystal structure. Numerous other solid electrolytes have been found subsequent to these studies.

Concerning the crystallographic defect theory, Joffe [20] proposed the concept of lattice defects or interstitial ions which provided a basis for the successive works of Frenkel [21] and Wagner and Schottky [22]. As a result of these studies, the thermodynamic theory of ionic conduction was established in the 1940's.

Since the 1950's, the development of new materials or devices based on this theoretical basis has been a key subject in this field. In other words, such theories enabled us to design materials or devices for practical application. A good example is the synthesis of $RbAg_4I_5$ by Bradley et al. [23] in 1966-67, which exhibits ionic conductivity at room temperature as high as liquid electrolyte solutions. They attempted to stabilize high conductive α-AgI below 149°C to room temperature at which its conductivity normally drops by 5-6 orders of magnitude. $RbAg_4I_5$ thus synthesized based on the α-AgI model may be a good example of material design, though the structures of these two materials are not analogous. Another example is NASICON ($Na_{1+x}Zr_2P_{3-x}Si_xO_{12}$), a famous Na^+ solid electrolyte synthesized by Goodenough and Hong [24] in 1967. This is a "tailored" solid electrolyte whose synthesis was based on an understanding of ionic conduction in a three-dimensional tunnel structure. Such successful material design subsequently produced various new solid electrolytes.

However, the most important discovery since 1950 may be the high sodium ion conduction in β-alumina (ideally, $Na_2O.11\ Al_2O_3$) found by Weber and Kummer [25], though existence of such a compound was known before the 1930's. At the present time, sodium sulphur batteries using this solid electrolyte are being developed for electrical vehicle propulsion. In materials science, however, we can not overlook the fact that the two-dimensional high ionic conduction of beta alumina provided a very useful guide for the development of new solid ionic conductors.

2-2 Lithium Solid Electrolytes

The low atomic weight and highly electropositive nature of lithium offers the possibility of high energy and cell voltages of up to 3 V. Furthermore, the metal is relatively easy to handle at room temperature and is also less expensive than noble metals such as silver. A number of cathode materials with high lithium diffusion coefficients are also available, some of which utilize the phenomenon of intercalation.

The recognition of lithium solid electrolytes dates from 1921, when Benrath and Drekopf [26] discovered high ionic conductivity in the high-temperature α-Li_2SO_4. Until the 1940s, however, only a handful of solids that exhibit transport of lithium ions had been recognized and studied. These were mostly alkali halides such as LiF and LiI, which have Schottky disorder and thus relatively low values of conductivity.

In 1967, much higher lithium ion conductivity was discovered in the β-alumina type layered compound. The lithium member of this family was synthesized by solid-state ion exchange from Na-β-Al_2O_3 in a molten salt. This work, as well as experimental demonstrations of rapid transport of other ions in a variety of crystal structures up to 1970 was reviewed by Pizzini [27].

The activity has continued since 1970. Therefore, a lot of solid lithium ion conductors have been investigated [9,10,11,12,13]. But none of those can be used as a solid electrolyte in a high energy density lithium battery since most of the lithium ion conductors are thermodynamically unstable against pure lithium or have other problems associated with processing or application. For example, Li-β-Al_2O_3 is one of the best lithium ion conductors, but is not stable in the presence of pure lithium. Furthermore, it is not thermally stable and will transform to the spinel $LiAl_5O_8$ at high temperature. The only alumina-based electrolyte which is stable to pure lithium is Li_5AlO_4, but it is quite hydroscopic and difficult to process outside a glove box. Li_3N is another good lithium ion conductor and it is thermodynamically stable against pure lithium , but its thermodynamic decomposition potential is only 0.44 V [28]. Li_2SO_4 has a very high conductivity, around 1 S/cm between 575°C and its melting point at 870°C [29,30]. The conductivity of the low temperature monoclinic β form is much less, however, and this structure is of little interest as a solid electrolyte, especially since it has not been possible to dope it and generate either lithium vacancies of interstitials [31,32]. LISICONS (lithium germinates and related compounds) also have high conductivities, but they are thermodynamically unstable in the presence of pure lithium and also some compositions are thermodynamically unstable below about 630°C [33,34,35].

Hellstrom and Van Gool have investigated the thermodynamic stability of solid electrolytes [8] against pure lithium and reported that there are number of possible electrolytes for lithium batteries in the Li_2O-ZrO_2 and Li_2O-Y_2O_3 systems [8].

Polezhaev and Chnukhlantsev studied the Li_2O-ZrO_2-SiO_2 system and found Li_2ZrO_3 exists between Li_2O and ZrO_2 [36]. Scholder, Rade and Schwarz further studied the Li_2O-ZrO_2 system and found the additional phases Li_4ZrO_4 and Li_8ZrO_6 exist in the system [37]. Later, $Li_6Zr_2O_7$ was also reported by Enreguez [38].

Li_2ZrO_3 has the highest melting point and is the least air-sensitive of the lithium zirconates though its stability with respect to pure lithium has not been determined. The crystal structure of Li_2ZrO_3 was determined by Dittrich and Hoppe [39]. Its conductivity was studied by Hellstrom and Van Gool and found to be 4.7×10^{-6} S/cm at 400°C, which is too low for battery applications. However, Li_2ZrO_3 has been investigated in nuclear materials research [40,41,42]. Because of the ease of tritium recovery, excellent thermal performance and good irradiation behaviour, it is considered a promising ceramic tritium breeder material in a fusion reactor. But it was found that the sinterability of Li_2ZrO_3 was poor, resulting in a product with generally about 80% theoretical density even by hot-pressing sintering [42].

Li_8ZrO_6 is a solid lithium ion conductor thermodynamically stable with respect to pure lithium [8]. Its crystal structure was determined by Hoppe et al.[43]. The formation enthalpy of Li_8ZrO_6 has been measured by Neubert and Guggi [44]. Its conductivity in the temperature range from room temperature to about 360°C has been studied by Hagenmuller [45], which is $2.1x10^{-5}$ S/cm at 227°C and $4x10^{-3}$ S/cm at 400°C by extrapolating. These are still too low for use as electrolytes in lithium batteries. But, Li_8ZrO_6 may find application in nuclear materials research [40,41,42].

$LiYO_2$ is the only compound in the Li_2O-Y_2O_3 system [46]. Its crystal structure was studied first by Hoppe et al. and was reported to be tetragonal [47]. Later work by Stewner and Hoppe showed that the structure is actually monoclinic and that the tetragonal modification is stabilized by the presence of impurity cations [48]. The conductivity is [46]:

$$\sigma=4x10^{3}exp[-79(kJ/mol)/RT]\ S/cm$$

On exposure to water vapor it shows the same increase in conductivity at about 380°C seen in Li_5AlO_4 due to the presence of LiOH [46].

Although some properties of Li_2ZrO_3, Li_8ZrO_6 and $LiYO_2$ have been reported, a systematic study on synthesis and preparation has not been done for these materials. Because of the high content of volatile lithium oxide, especially for the Li_8ZrO_6, it is very difficult to prepare single phase materials. The thermodynamic stabilities of these materials have not been studied and the heat capacity and entropy data of these materials are not available. Studies on improving the conductivity of these materials has not been reported.

CHAPTER 3 EXPERIMENTAL TECHNIQUES

3.1 Infrared Spectroscopy

The utility of infrared spectroscopy to the organic chemist is perhaps unsurpassed within the framework of most modern laboratories. Experimental, theoretical, and empirical correlations between functional organic groups and the infrared spectrum have been thoroughly studied and tabulated. The vast body of literature devoted to the results of these studies provides a rather solid base for the analytical spectroscopist. Through the efforts of several authors this accumulated data has been summarized and reviewed in several excellent publications [49,50,51,52,53,54,55].

The application of infrared spectroscopy to the identification of inorganic compounds has been somewhat less successful. Many simple inorganic compounds such as the borides, silicides, nitrides and oxides, do not absorb radiation in the region between 4000 and 600 cm^{-1} which, for many years, was the infrared region covered by most commercial spectrometers. Only within the 1960's have instruments become available which include the region below 600 cm^{-1} , and it is more recently that instrumentation has been developed to cover the far-infrared region between 200 and 10 cm^{-1}. These are the regions in which most inorganic compounds absorb infrared radiation. In addition, the infrared spectra derived from inorganic compounds usually have absorption bands that are broad and overlapping, making assignments and specific identifications of a cation-anion pair more difficult. Moreover, due to the power of the X-ray diffraction technique, the introduction of infrared spectroscopy into the field of crystalline materials has been limited. However, the infrared technique is quick, simple, relatively inexpensive and serves as a useful supplementary technique in the identification of crystal materials. Furthermore, owing to its sensitivity to local bonding forces and to symmetry properties, the infrared spectrum of inorganic solids can be taken for further structural refinement, or used for glasses and semi-amorphous materials where the diffraction methods have lost their efficiency.

Infrared spectroscopy involves absorption, originating from vibration and rotation of a molecule, of electromagnetic radiation in the infrared region of the spectrum. The energy associated with a quantum of light may be transferred to the molecule if work can be performed on the molecule in the form of displacement of charge. This requirement gives rise to the selection rule for infrared activity. A molecule will absorb infrared radiation if the charge of the vibrational state is associated with a change in the dipole moment of the molecule. For the simple case of a diatomic molecule, the absorbed frequencies (wavenumbers) can be calculated by the following formula

$$\nu = \frac{1}{2\pi c}\sqrt{\frac{f}{\mu}} \quad \ldots\ldots\ldots\ldots\ldots\ldots\ldots \quad 3\text{-}1$$

where ν = wavenumber of the vibration

c = velocity of light

f = force constant of the bond

μ = reduced mass of the atoms involved

For polyatomic molecules, certain groupings may be considered for group frequencies. These group frequencies have been compiled for a large number of molecules, and relatively reliable correlation charts have been devised.

The importance of infrared spectroscopy as a complementary technique to X-ray diffraction in the identification of minerals has become increasingly appreciated during the last two decades or so. Infrared absorption spectra can be employed for the identification of pure compounds or for the detection and identification of impurities. The infrared absorption spectrometer can also used for quantitative analysis. The infrared analytical technique is extremely sensitive to short-range site occupancy differences and thus may be contrasted with X-ray diffraction techniques which rely mainly on longer range ordering and on the periodic repetition of atoms.

For example, the IR spectrum is very useful for studying substitutional solid solutions and for identifying some polyanions. For a substitutional solid solution such as $(A_{1-x}B_x)CO_n$ in which two cations A and B substitute for each other, modifications of the spectrum as a function of x may be of two kinds (Fig.3.1).

(a) the so-called two modes behaviour, in which bands due to A-O vibrations disappear progressively and are replaced by bands due to B-O vibrations. The bands due to C-O vibration will be shifted systematically with x.

(b) the so-called one mode behaviour, in which a single band (more or less broadened) will be observed throughout the series of solid solution, at a frequency which is roughly a weighted average of the frequencies of the end-members. Therefore, from these spectrum behaviours, it is easy to identify whether a solid solution is formed.

In addition, the IR spectrum of many simple monoanions (OH^-, NO_3^-, CO_3^{2-}, PO_4^{3-}, SO_4^{2-}, etc.) has been widely investigated [56,57,58,59]. Generally speaking, and apart from some specific cases, the vibrational spectra of such anions is characterized by two groups of vibrational frequencies(corresponding to the stretching and bending motions of the anion). Therefore, it is often possible to identify an anion and distinguish a polyanion from a monoanion.

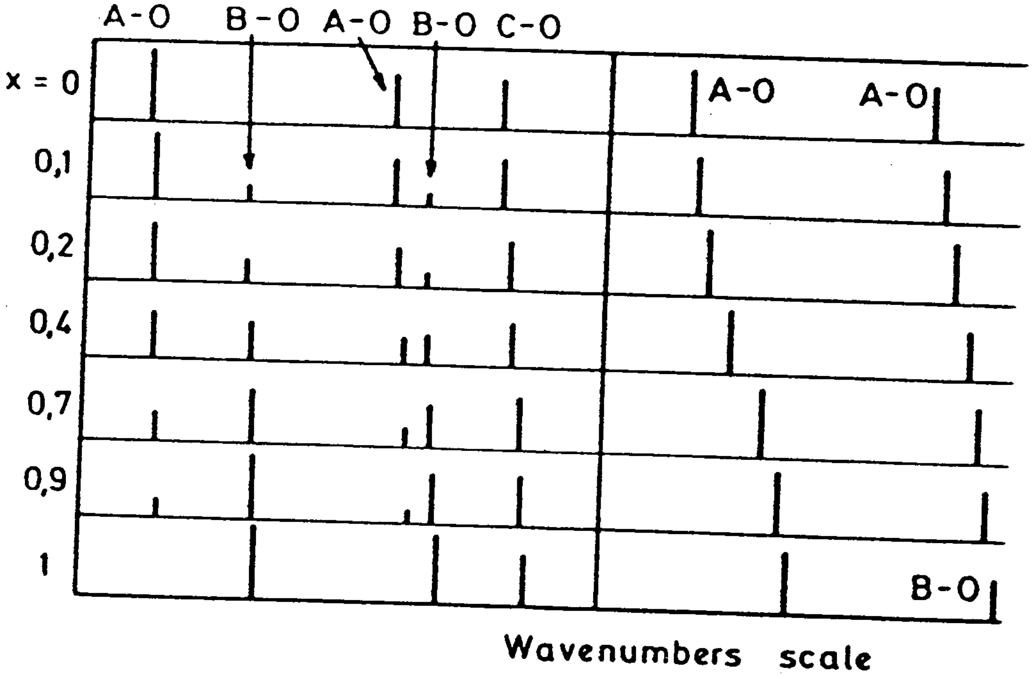

Fig.3.1 Schematic idealized vibrational behaviour of a solid solution$(A_{1-x}B_x)CO_n$. Left: Two-modes behaviour; right: one-mode behaviour.

3-2 AC Impedance Measurement

Small-signal ac impedance measurements have become a standard technique for characterizing liquid and solid electrolytes and other materials since Bauerle [60] first applied this technique to a solid electrolyte system. Analysis of small-signal data can almost always yield estimates of bulk conductivity of new materials free from the electrode polarization effects which plague steady-state dc measurements. Under favourable conditions, detailed analysis of impedance data for homogeneous materials in terms of an appropriate model of the electrode / electrolyte system can also yield accurate estimates of microscopic parameters: mobilities, dielectric constant, electrode reaction rate constants, etc., which characterize interface and bulk behavior of the system [61,62]. Even for polycrystalline solid electrolytes such as β-alumina, proper analysis may lead to valuable information about electrode reactions and intergrain properties.

The impedance Z of a RC parallel circuit is given by

$$Z(\omega)=\frac{R}{1+R\omega Ci}=\frac{R}{1+R^2\omega^2C^2}-\frac{\omega CR^2}{1+R^2\omega^2C^2}i \qquad (3-2)$$

where R and C are the equivalent parallel resistance and capacitance, respectively, ω is the frequency, and i represents the imaginary component. The admittance Y is the inverse of impedance and is expressed as

$$Y(\omega)=\frac{1}{Z(\omega)}=\frac{1}{R}+i\omega C=G+i\omega C \qquad (3-3)$$

where G=1/R

From equation 3-2, it can be derived that

$$(ReZ-\frac{R}{2})^2+(ImZ)^2=(\frac{R}{2})^2 \qquad (3-4)$$

Therefore, for an RC parallel circuit, the plot of ImZ versus ReZ will be a semicircle while the plot of ReY versus ImY will be vertical line. Similarly, a few simple examples are presented in Fig.3.2. Arrows in the diagram represent the direction of increasing frequency. Shapes of the plots vary greatly with circuit elements. In general it may be said that each semicircular arc corresponds to a lumped RC combination, a vertical line represents a lone capacitance, and a quarter

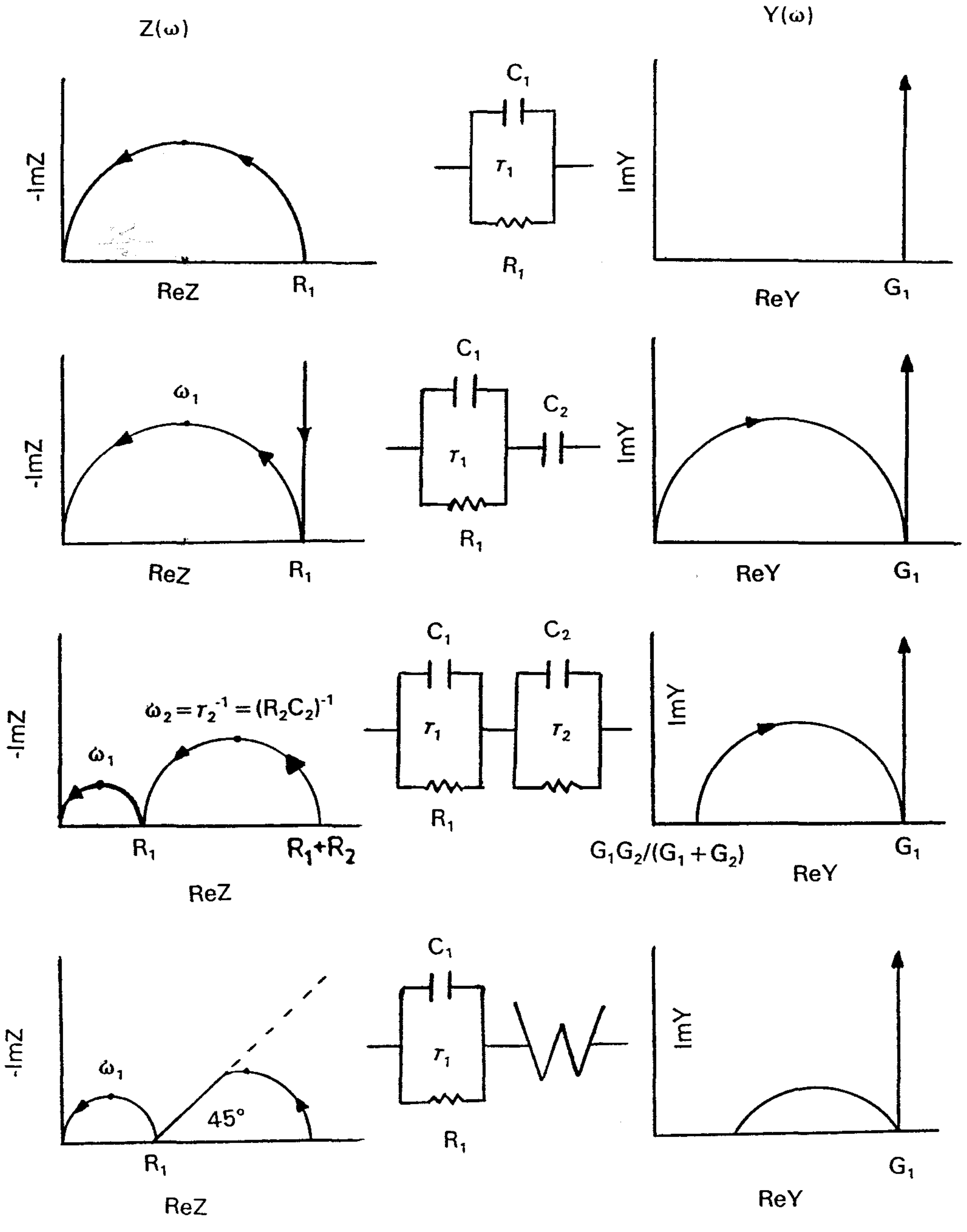

Fig.3.2 Schematic impedance and admittance diagrams for some simple RC circuits.

circle with a 45° line represents a Warburg impedance which is the electrical analog of a diffusion process (Fig.3.3). It is possible to calculate the resistance and capacitance values from the intercepts on the real axis and the highest point in the semicircles, respectively. More details regarding the theory of this technique may be obtained in references 60, 62 and 63. When similar diagrams are constructed with the real and imaginary value of dielectric constant these are known as Cole-Cole plots.

The physical processes which take place in an electric field are very often represented by analogous electrical circuits. Impedance measurement has been successful in qualitative as well as quantitative determination of such equivalent circuits and therefore provides much better insight into the transport mechanism. In principle any such equivalent circuit may be represented either by a Maxwell model (Fig.3.4a) or a Voigt model (Fig.3.4b). Mathematically they are interchangeable so that with the proper choice of element values they can have the same impedance values at all frequencies, although the transformation becomes difficult when the number of the lumped RC combination N is larger than 2. However, their powers of interpretation of the physical processes are not always the same and the final selection between them depends on the

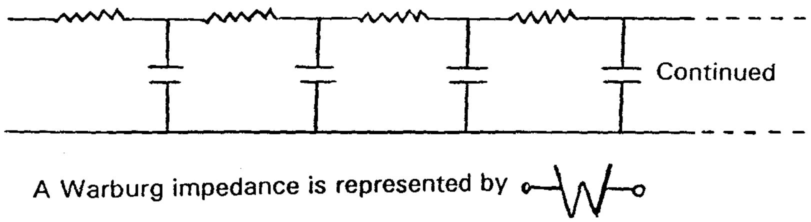

Fig.3.3 Circuit diagram for Warburg impedance.

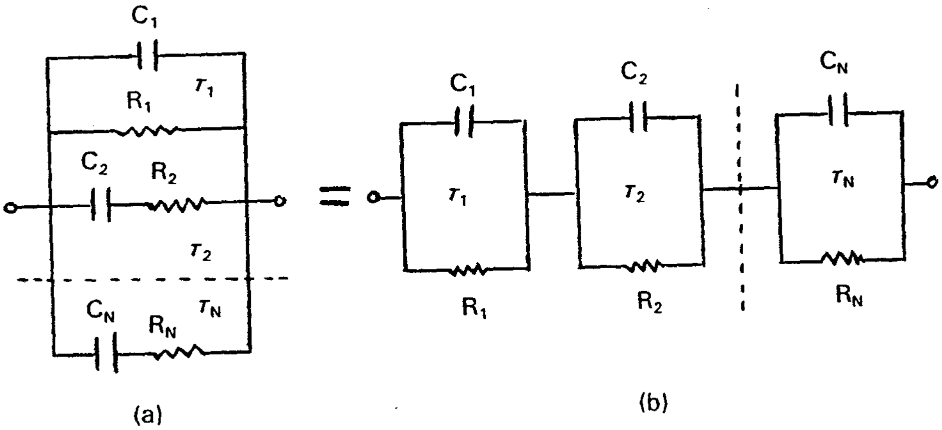

Fig.3.4 Two types of representation for equivalent circuits.

(a) Maxwell model, (b) Voigt model.

nature of the particular system under investigation. It may be mentioned that an admittance plot is preferable for a Maxwell model, while an impedance diagram will give more information for a Voigt model. Although a two layer Voigt model is very often used to describe a solid electrolyte system, the actual circuit may be quite complicated and depend on the exact nature of the transport mechanism. McDonald [64] has proposed a five-layer Voigt model (Fig.3.5a) in which each of the RC sections correspond to one of the following five impedances:(1) bulk or intragrain impedance (B), (2) intergrain impedance (G), (3) electronic impedance of the electrode (E), (4) absorption reaction impedance (A), (5) Warburg diffusion impedance (D). An impedance diagram for such a system will result in a series of connected arcs (Fig.3.5b) each associated with a single impedance provided the relaxation time (τ=RC) of those processes differs at least by two orders of magnitude. Since each of these relaxation processes follows Arrhenius behaviour, impedance measurement as a function of frequency and temperature enables determination of activation energy for each. In practice, however, it is quite common that all five arcs may not be observable at the same time. The relative sizes will also vary greatly depending on the experimental conditions. In general, the absorption impedance and the electronic impedance are too small to be observed for a pure solid electrolyte. In

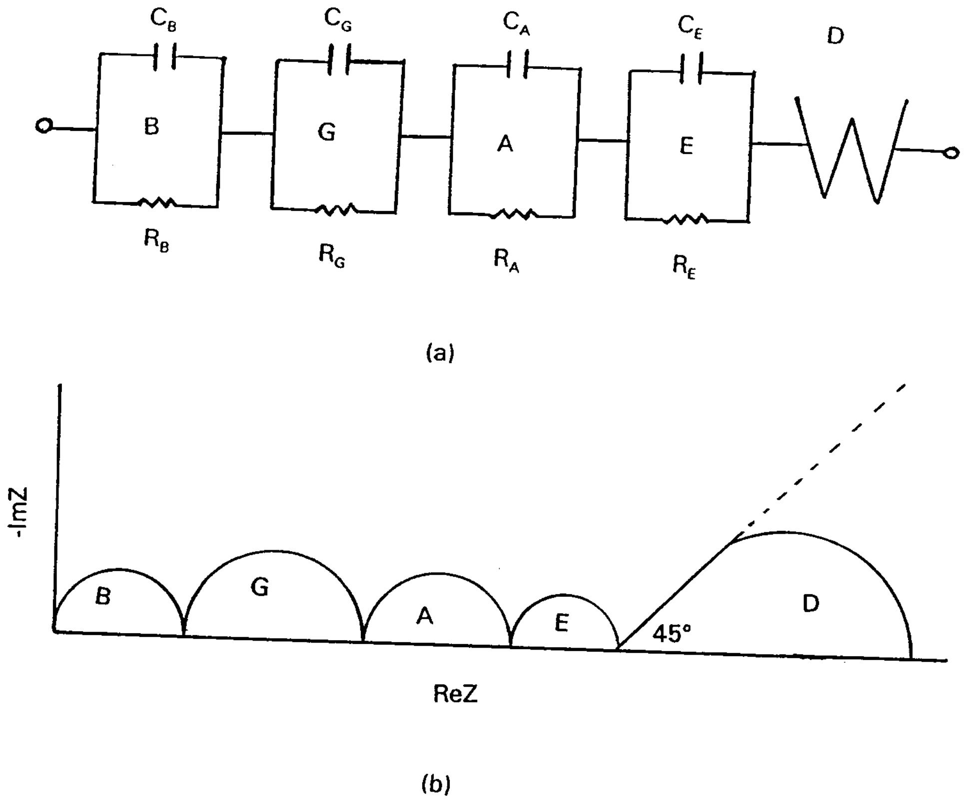

Fig.3.5 Equivalent circuit (a) and impedance diagram (b) for a solid placed between two plane parallel electrodes.

actual experiments the arcs are often less than half-circles. This is believed to be due to a distribution of relaxation times instead of a distinct one.

For example, a maximum of three arcs has been observed with CaO and Y_2O_3 stabilized ZrO_2 electrolytes [65,66,67,68]. β-alumina [69,70,71,72] and Ag_4RbI_5 [72] electrolytes have also been studied by this technique. It has been possible to make accurate estimations of electrode and electrolyte resistances in these electrolytes. It is also possible to measure the activation energy and the mobility of the charge carriers by this technique.

However, it has been found that the ac impedance spectrum of practical electrochemical cells usually shows non-ideality, i.e., deviation from ideal resistance and capacitance elements in the equivalent circuit. Then the semicircle arc will become a depressed circular arc whose center lies below the real axis. By analogy with the well-known Cole-Cole complex permittivity plot, the non-ideal impedance spectrum can be reproduced in terms of the impedance expression by introducing a depression coefficient α [73,74]

$$Z(\omega) = \frac{R}{1+(i\omega CR)^{1-\alpha}} \tag{3-5}$$

This will make the analysis for the impedance data much more complicated. But in principle, it is still possible to make accurate estimations of electrode and electrolyte resistances as well as to differentiate between the bulk and grain boundary resistances in solid electrolytes from complex function theory and curve fitting.

CHAPTER 4 MATERIALS AND PREPARATION

In this present work, the sintered samples of Y-doped Li_2ZrO_3 and Li_8ZrO_6 and Zr-doped $LiYO_2$ were prepared via conventional solid reactions. The structures of these samples were studied by XRD. The conductivity of the samples were measured by complex impedance methods and dc polarization.

4-1 Y-doped Li_2ZrO_3

The starting materials were reagent grade Li_2CO_3 and ZrO_2 and analytical grade Y_2O_3. The materials were weighed, ground and intimately mixed in an agate mortar with a suitable amount of acetone. The mixtures were calcined at 1000°C for 10 hours. The calcined samples were ground again in the mortar and pressed into 12 mm diameter by 1 to 4 mm thick pellets at 69 MPa(10^4 psi). The pellets were sintered at 1400°C for 20 hours and at 1450°C for 5 hours buried in Li_2ZrO_3 powders in an alumina crucible.

The sintered samples were polished on SiC paper with acetone. Silver paste was put on both polished surfaces and then baked at 600°C for about 4 hours to obtain the samples for conductivity measurements.

4-2 Y-doped Li_8ZrO_6

The starting materials were the oxides of reagent grade ZrO_2 and Li_2O_2 and analytical grade Y_2O_3. The appropriate amounts of oxides were weighed, mixed and ground in an agate mortar with a suitable amount of acetone. The ground powders were fired in Al_2O_3 crucibles in air first at 130 to 150°C for one day then at 900°C for 3 days. The reacted samples were ground again in the mortar and pressed into pellets of 13 mm diameter and 2 to 5 mm thickness at 70 MPa. Finally the pellets were buried in Li_8ZrO_6 powders in alumina crucibles and sintered in air at 500°C for one day, then 800°C for 8 hours and at 930°C for a half hour to obtain samples of $Li_{8+x}Y_xZr_{1-x}O_6$.

Sintered samples were stored in a desiccator for about two months and then polished, coated with silver paste and baked at 600°C for 2 hours to obtain the samples for conductivity measurements.

4-3 Zr-doped $LiYO_2$

Starting materials were reagent grade Li_2CO_3 and ZrO_2 and analytical grade Y_2O_3. Compositions of $Li_{1-x}Zr_xY_{1-x}O_2$ ($0 \leq x \leq 0.5$) and $Li_{1+x}Zr_xY_{1-x}O_2$ ($0.15 \leq x \leq 0.30$) were prepared. The appropriate amounts of oxides were weighed, mixed and ground in an agate mortar. They were fired in air at 705°C for 15 hours and at 1200°C for 12 hours and then at 1400°C for 5 hours. The reacted samples were ground again in the mortar and pressed into pellets with 13 mm diameter by 2 to 5 mm thickness at 70 MPa. Finally the pellets were sintered in alumina crucibles at 1400°C for 15 hours and 1450°C for 5 hours to obtained the sintered samples.

Sintered samples were polished on SiC papers with acetone. Then gold of about 100 nm thickness was sputtered on both polished surfaces to obtain the samples for conductivity measurements.

CHAPTER 5 EXPERIMENTAL RESULTS

The solubilities, crystal structures and microstructures for Y-doped Li_2ZrO_3, Y-doped Li_8ZrO_6 and Zr-doped $LiYO_2$ were studied by XRD, IR spectra, and SEM. The conductivities of these materials were studied by ac complex impedance and dc polarization. The tentative phase diagram of LiO_2-Y_2O_3-ZrO_2 from this study is shown in Fig.5.1.

5-1 Yttrium-doped Li_2ZrO_3

5-1-1 XRD analysis

Powder x-ray diffraction experiments were done using Cu-Kα radiation with Ni-filter for all sintered samples. The lattice parameters were determined by means of a least squares unit cell refinement program from a Guinier camera pattern and silicon as the internal standard . The powder x-ray diffraction patterns for $Li_{2+x}Y_xZr_{1-x}O_3$, where the samples with x=0, 0.01, 0.05, 0.1 were labelled as ZYNS1, ZYNS2, ZYNS3, and ZYNS4, respectively, are shown in Fig.5.2. From JCPDS card #33-843, it can be seen that the diffraction peaks for the samples with x=0, x=0.01, and x=0.05 can be matched with those

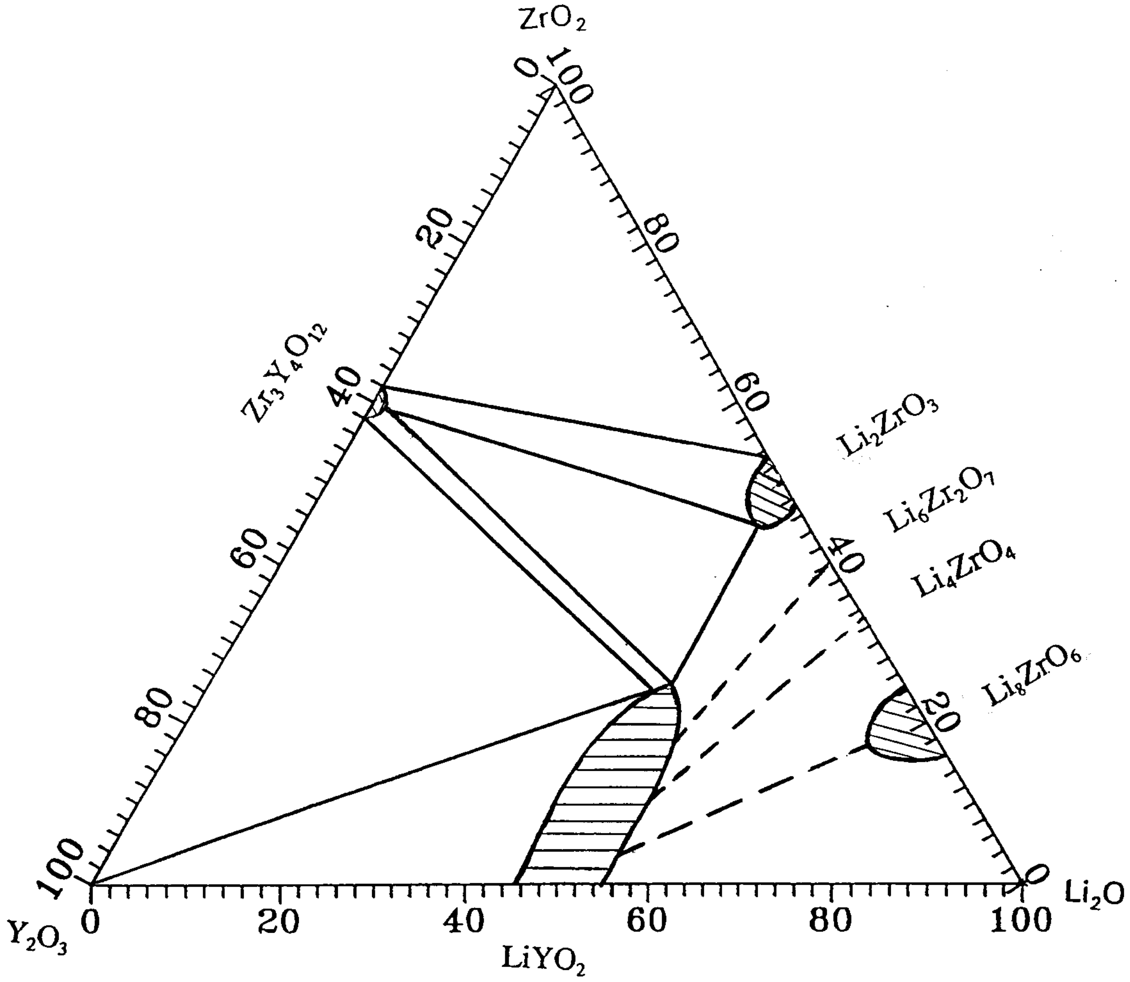

Fig.5.1 The tentative phase diagram in the LiO$_2$-ZrO$_2$-Y$_2$O$_3$ system

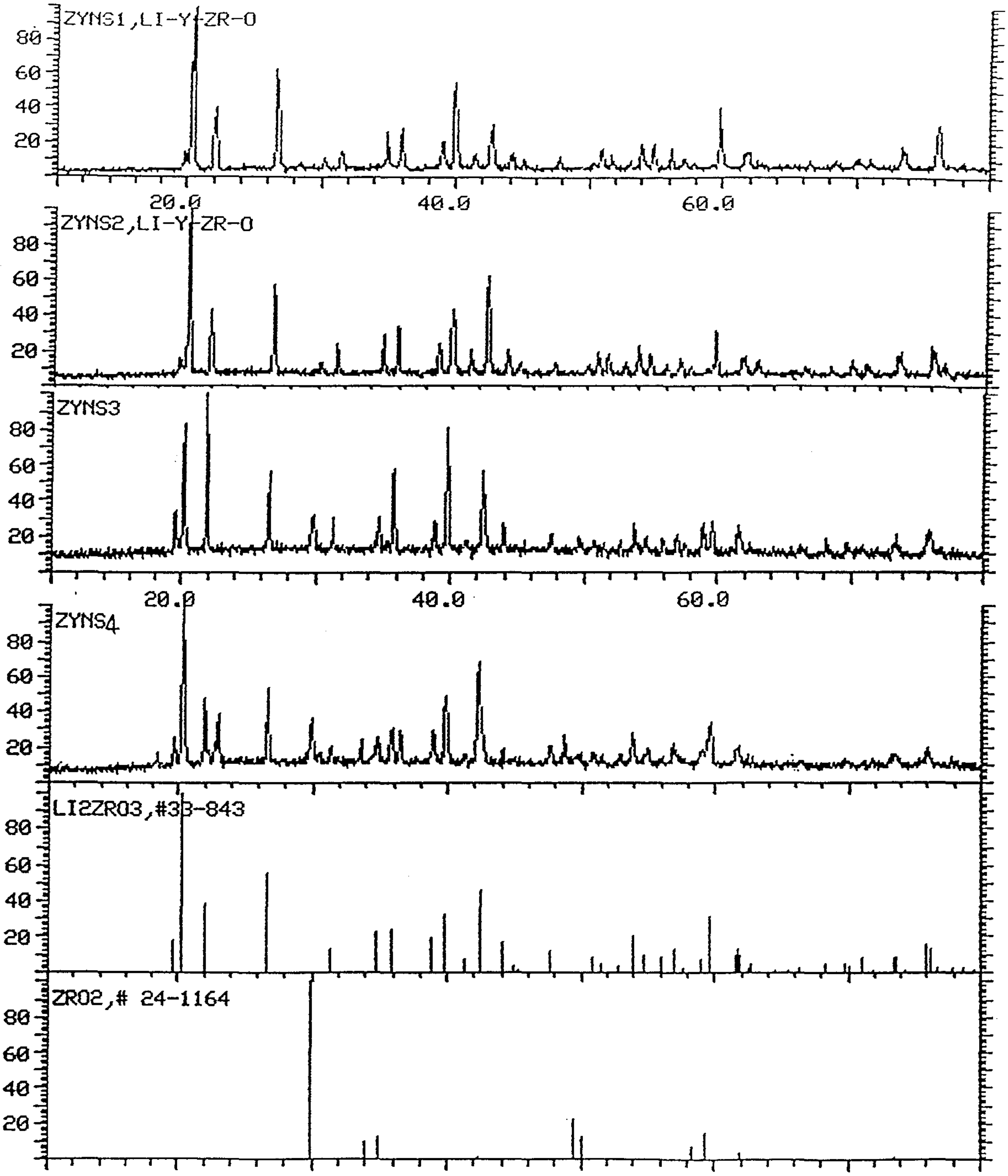

Fig.5.2 The X-ray diffraction patterns for the samples of $Li_{2+x}Y_xZr_{1-x}O_3$ with x=0 (ZYNS1), x=0.01 (ZYNS2), x=0.05 (ZYNS3), and x=0.10 (ZYNS4).

of Li_2ZrO_3 except for two small peaks, which may be assigned to zirconia. But for x=0.1, there are a number of peaks which corresponded to $Li_6Zr_2O_7$, indicating the onset of a 2-phase region. The XRD results also show that the diffraction peaks systematically shift toward lower diffraction angles and larger d spacings with the increase in x from 0 to 0.05, but those corresponding to Li_2ZrO_3 for sample ZYNS4 (with x=0.1) appear in almost the same positions as for sample ZYNS3. The lattice parameters were calculated by means of a least squares unit cell refinement program, and the results are listed in Table 5.1.

Table 5.1 Lattice parameters of $Li_{2+x}Y_xZr_{1-x}O_3$ solid solutions

x	a(Å)	b(Å)	c(Å)	$\alpha(^0)$	$\beta(^0)$	$\gamma(^0)$	v(Å^3)
0	5.4159	9.0120	5.4187	90	112.7059	90	24.3981
0.01	5.4267	9.0489	5.4212	90	112.7101	90	24.5574
0.05	5.4406	9.0598	5.4333	90	112.6037	90	24.7241

In forming the solid solution, yttrium substitutes for zirconium on the normal zirconium lattice. From the point of view of electrical neutrality, the presence of yttrium would be balanced by oxygen vacancies. However, adding yttrium and lithium as in the present case would result in lithium interstitials in unoccupied interstitial sites. This corresponds to a $Li_{2+x}Y_xZr_{1-x}O_3$ stoichiometry for the solid solution.

5-1-2 IR spectra analysis

Infrared absorption spectra analysis was carried out in a Bio-RED ETS-40 laser IR spectrometer. The IR absorption spectra for sample ZYNS1 (x=0) and sample ZYNS3 (x=0.05) are shown in Fig.5.3. From Fig.5.3, it is found that there are five main peaks at 1450, 860, 750, 500, 450 cm^{-1}. The peaks at 1450 and 860 cm^{-1} are from CO_2 and water, respectively, due to residual water or CO_2 remaining from preparation. The peaks at 750, 500 and 450 cm^{-1} from ZrO_3^{2-} [75] shift to lower wave numbers with yttrium substitution in sample ZYNS3, which is further evidence for the formation of the $Li_{2+x}Y_xZr_{1-x}O_3$ solid solution. The shift in wavenumber is due to a decrease in the vibrational constants of $[Y_xZr_{1-x}O_3]^{(2+x)-}$ relative to those of ZrO_3^{2-} due to the lower electrical charge and larger ionic radius of the Y^{3+} ion.

5-1-3 SEM analysis

Microstructures of all the samples were observed using

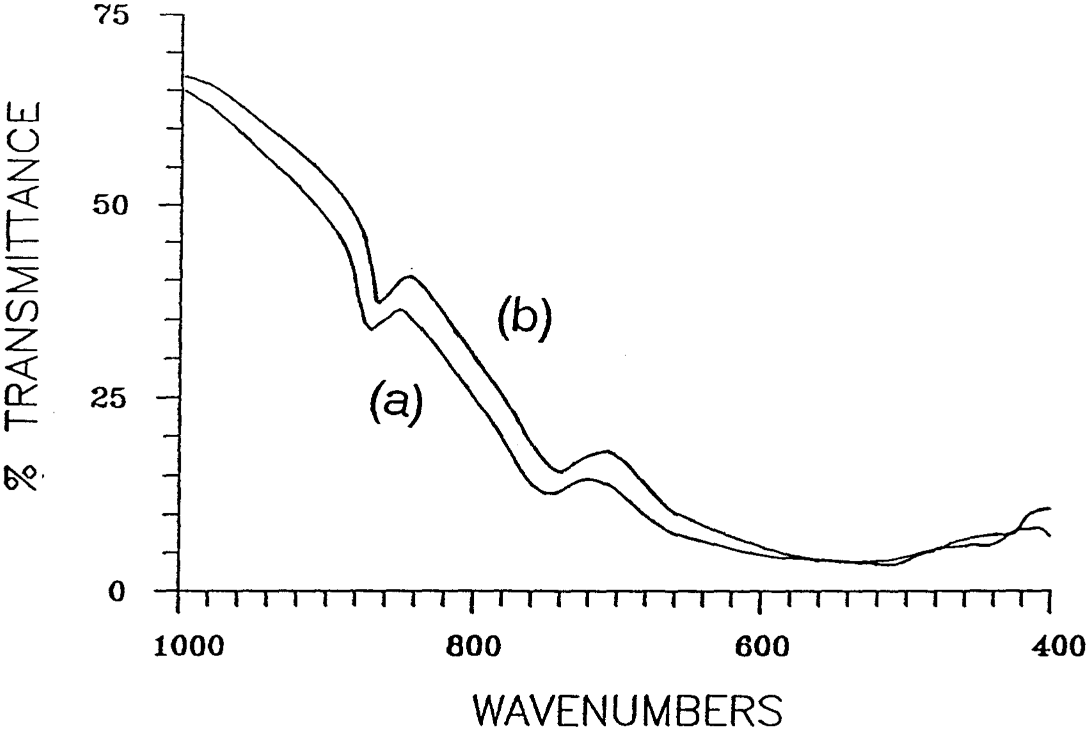

Fig.5.3 IR absorption spectra for samples a (Li_2ZrO_3) and b ($Li_{2.1}Y_{0.1}Zr_{0.9}O_3$).

a Phillips 515 SEM. The SEM micrographs of the fracture surfaces of the samples are shown in Fig.5.4. With the increase in composition x, the samples become denser, and the grain size becomes smaller and more equiaxed. Also the element analysis was carried out using an EDX LINK QX 2000 detector for all the samples. The results showed that silicon was not found in the samples.

5-1-4 pH measurements

pH values of the samples were measured using pH paper. The pH of all the samples both in distilled water and ethanol have a common value of 10.5. This shows that the Li_2ZrO_3 will hydrolyse in water and ethanol. The formation of the solid solution does not affect the reactivity of Li_2ZrO_3 with water and ethanol.

5-1-5 Density measurement

Density of the samples was measured by Archimedes' method with toluene. The density results of all the samples of $Li_{2+x}Y_xZr_{1-x}O_3$ are shown in Table 5.2 and Fig.5.5. The relative density values were calculated on the basis of the theoretical densities which were calculated based on the results from Table 5.2 and the Li_2ZrO_3 crystal structure data from JCPDS card 33-843. From Table 5.2 and Fig.5.4, it can be seen that the density and relative density increase from 3.368 g/cm^3 or

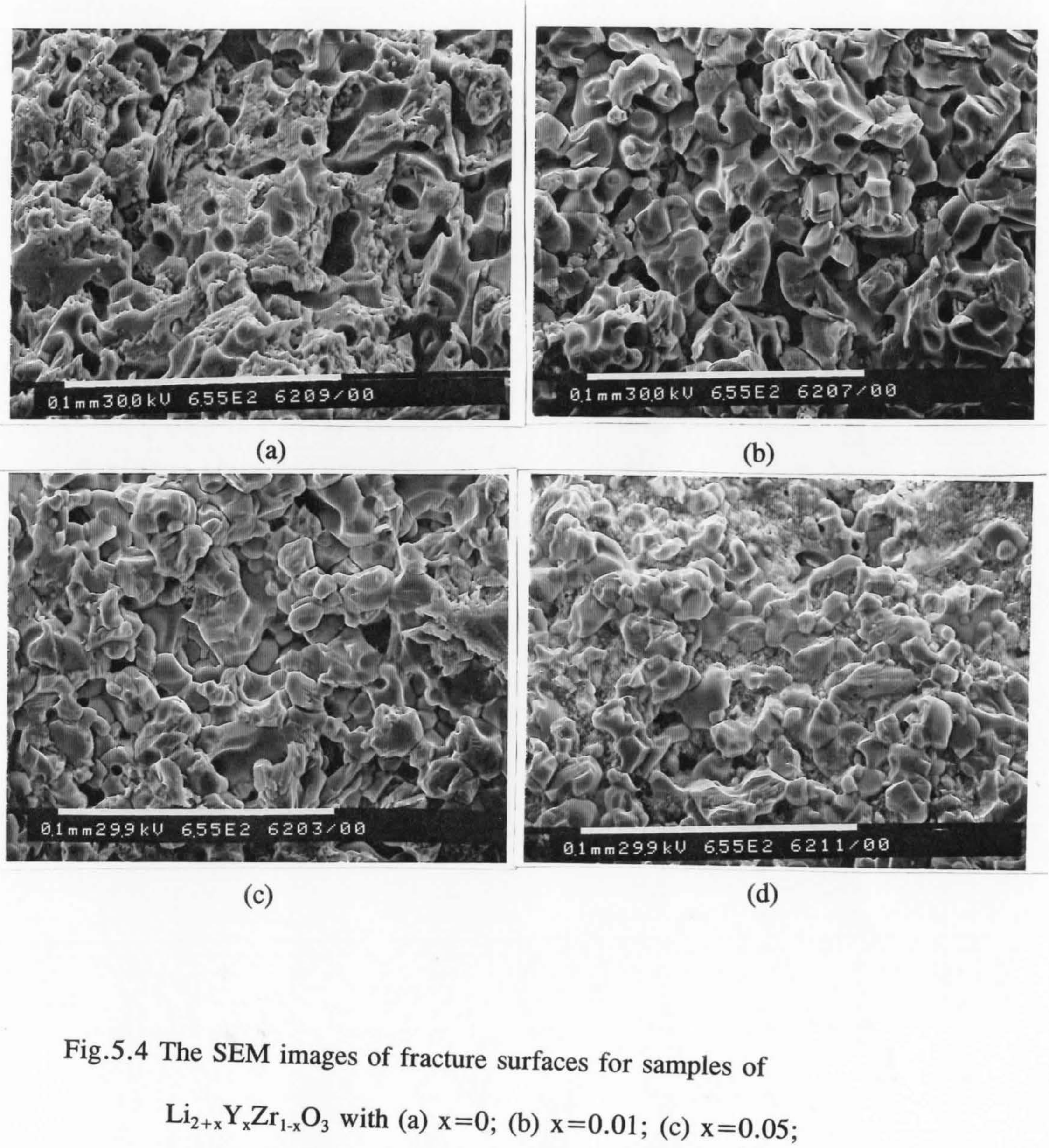

(a) (b)

(c) (d)

Fig.5.4 The SEM images of fracture surfaces for samples of $Li_{2+x}Y_xZr_{1-x}O_3$ with (a) x=0; (b) x=0.01; (c) x=0.05; and (d) x=0.10.

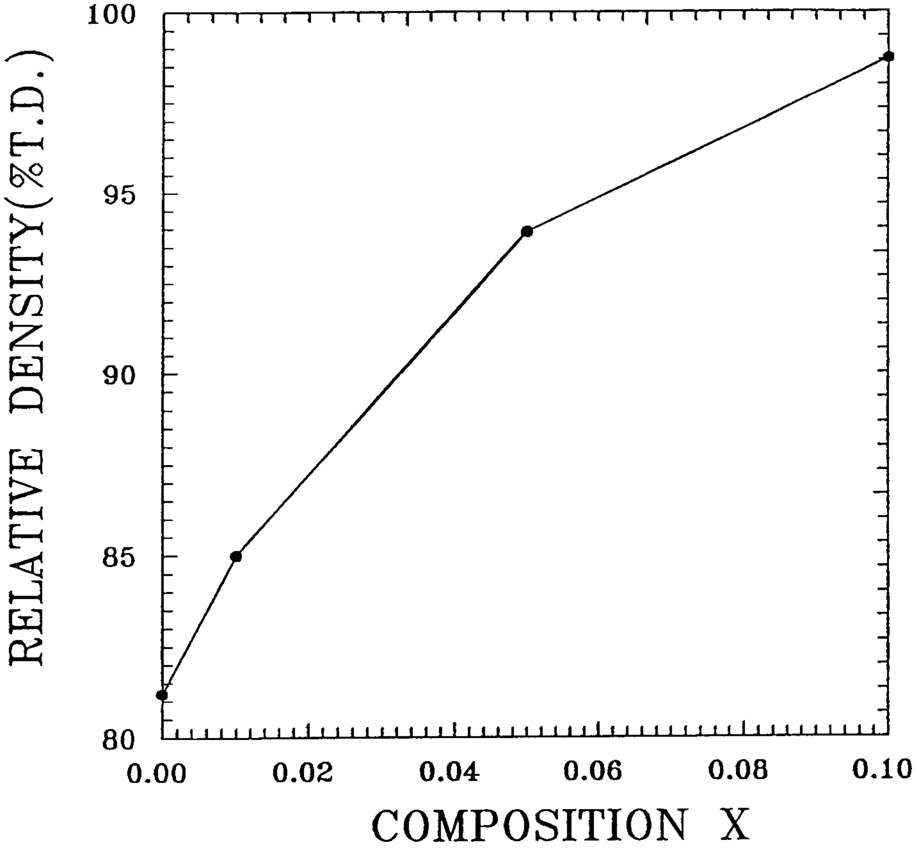

Fig.5.5 The dependence of relative density on varying composition x for samples of $Li_{2+x}Y_xZr_{1-x}O_3$. The relative density of sample ZYNS4 with x=0.1 was calculated based on the theoretical density of sample ZYNS3 with x=0.05.

80.8% T.D. to 4.094 g/cm^3 or 99.4% T.D., respectively, with x increasing from 0 to 0.1.

The combined results of XRD, IR and SEM analyses show that a single phase solid solution of $Li_{2+x}Y_xZr_{1-x}O_3$ was formed when the amount of yttrium introduced is not larger than 0.05, but the sample with x=0.1 consisted of the solid solution and a small amount of $Li_6Zr_2O_7$ second phase. It can be seen that the formation of the solid solution can improve the sinterability of Li_2ZrO_3 by decreasing the grain size and the porosity and producing more uniform microstructures. This can be explained as follows.

Since Li^+ ion transport is much faster than Zr^{4+} and O^{2-} ion transport, the densification rate at sintering temperatures is controlled by the diffusion of Zr^{4+} and O^{2-} ions. The formation of the solid solution raises the mobility of Zr^{4+} and O^{2-} ions since the lattice size is increased, as can be seen from XRD results and the average interaction between Zr^{4+} and O^{2-} ions is reduced upon substitution of Y^{3+} ions as reflected in IR spectra analysis. Also, the formation of the solid solution will decrease the boundary energy and reduce the driving force for grain growth. Therefore, the formation of the solid solution will increase the densification rate and retard grain growth leading to improved sinterability of Li_2ZrO_3. Since sample ZYNS4 with x= 0.1 falls in a 2-phase region, there will be a small amount of liquid phase present at sintering temperatures. This factor will improve the sinterability of Li_2ZrO_3 even more effectively.

Table 5.2. Densities of $Li_{2+x}Y_xZr_{1-x}O_3$ samples. The relative density of sample ZYNS4 with x=0.1 was calculated from the theoretical density of sample ZYSN3 since the amount of the $Li_6Zr_2O_7$ second phase is unknown.

sample	x value	theoretical density(g/cm^3)	measured density(g/cm^3)	relative density(%T.D.)
ZYNS1	0	4.167	3.368	80.8
ZYNS2	0.01	4.142	3.526	85.1
ZYNS3	0.05	4.119	3.895	94.6
ZYNS4	0.1		4.094	99.4

5-1-6 Conductivity measurement

A.C. complex impedances were measured on an HP 4192A computerized impedance analyzer in the frequency range from 2 Hz to 10 MHz for all samples. The typical ac complex impedance spectra for the samples of $Li_{2+x}Y_xZr_{1-x}O_3$ are shown in Fig.5.6. It can be seen that the shapes of the plots are very similar for all the samples, consisting of a curved part in

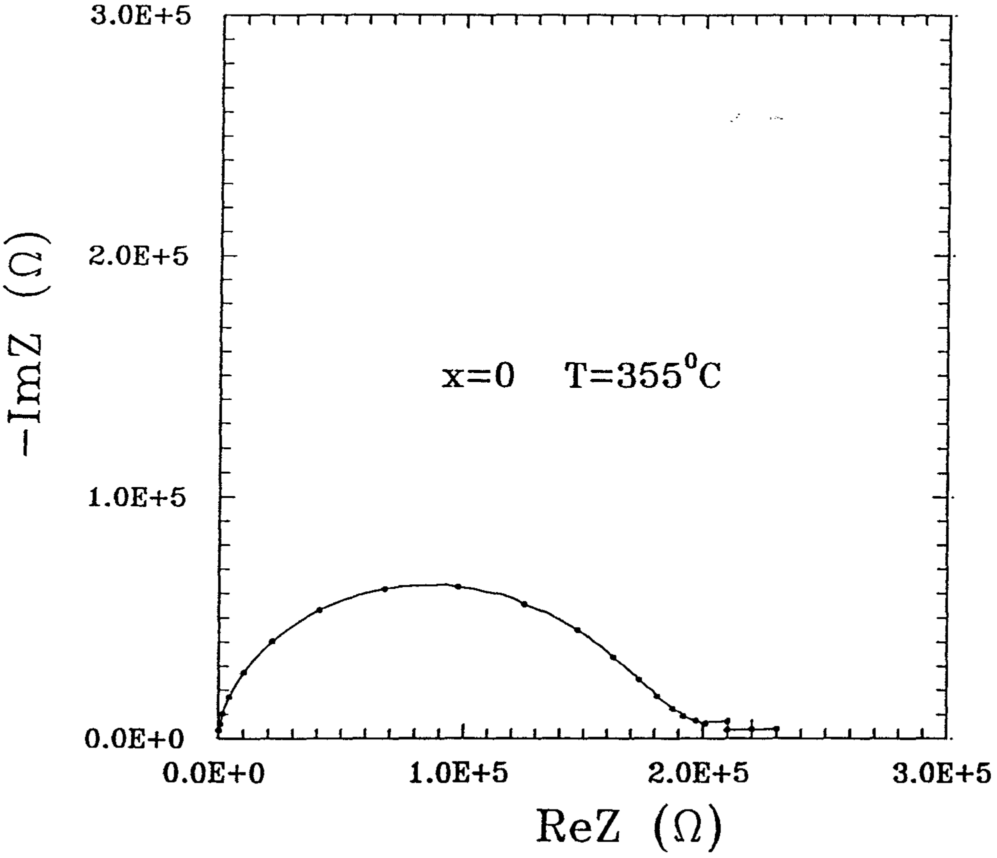

Fig.5.6a The ac impedance spectra in the frequency range of 2 Hz to 10 MHz for the ceramic samples of $Li_{2+x}Y_xZr_{1-x}O_3$ with x=0.

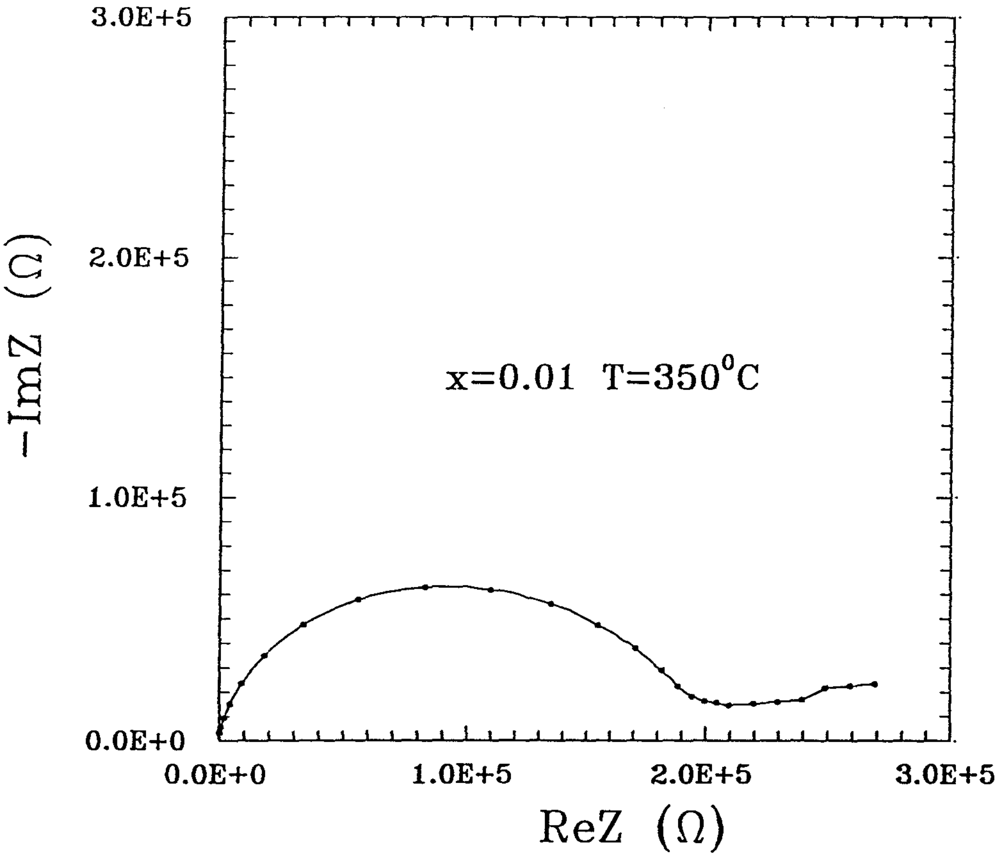

Fig.5.6b The ac impedance spectra in the frequency range of 2 Hz to 10 MHz for the ceramic samples of $Li_{2+x}Y_xZr_{1-x}O_3$ with x=0.01.

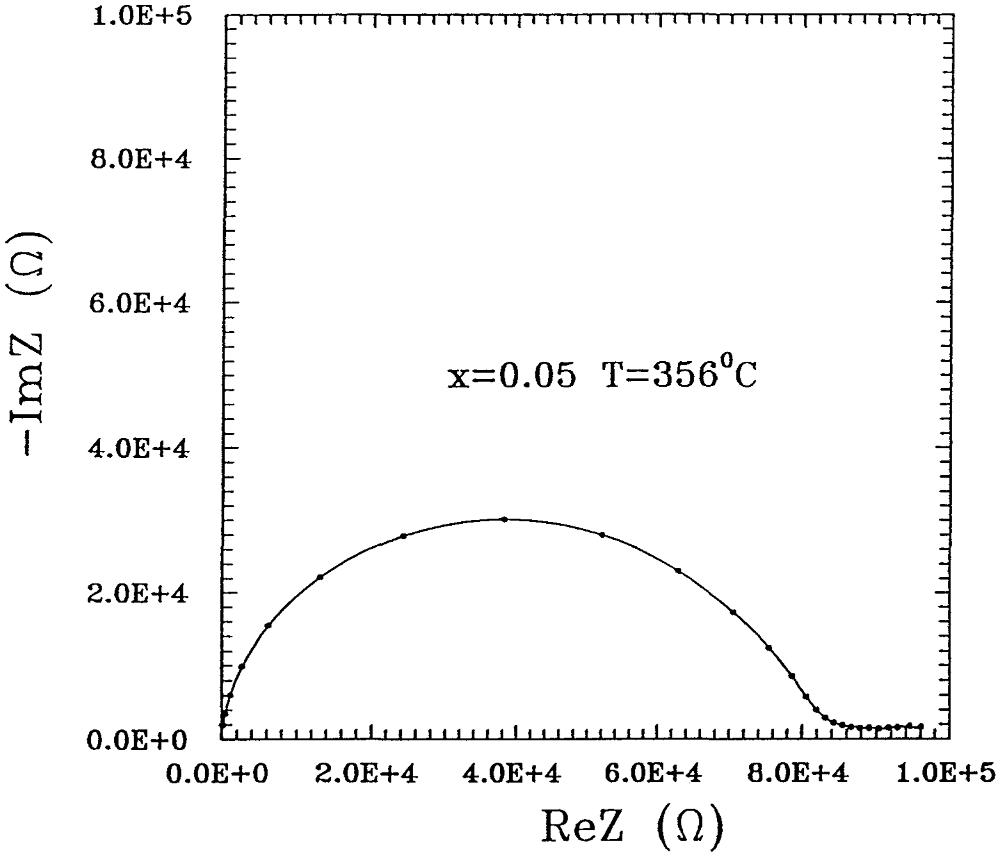

Fig.5.6c The ac impedance spectra in the frequency range of 2 Hz to 10 MHz for the ceramic samples of $Li_{2+x}Y_xZr_{1-x}O_3$ with x=0.05.

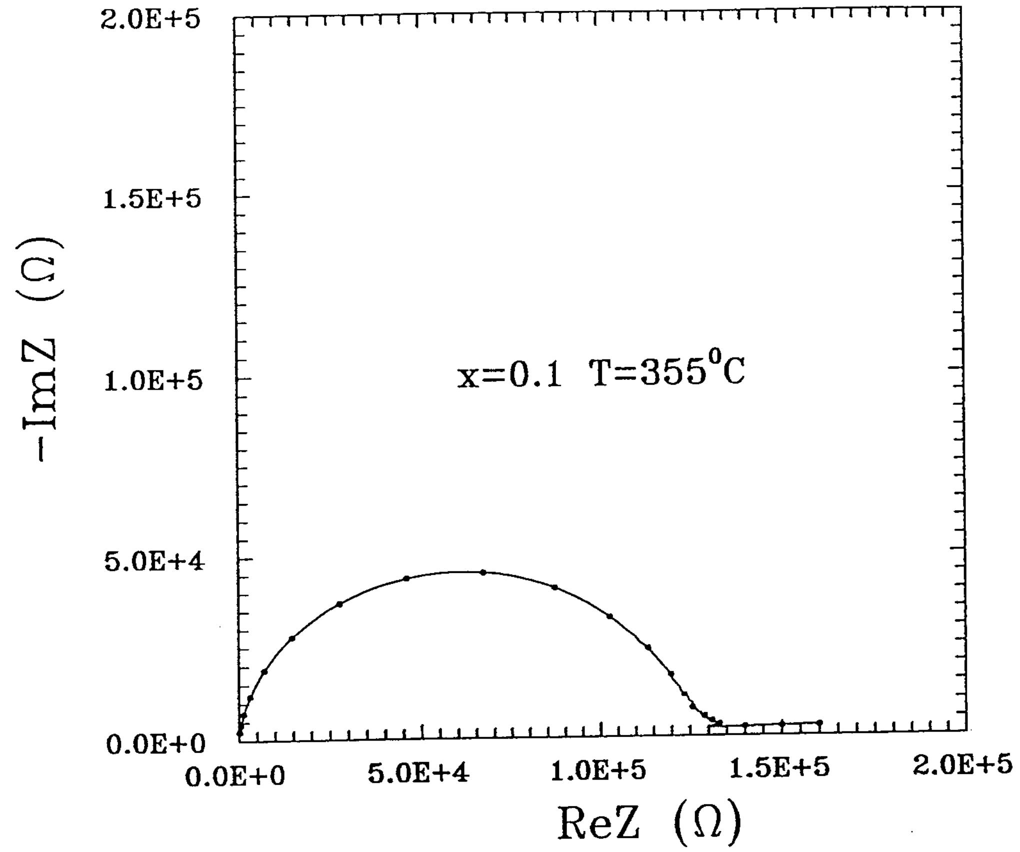

Fig.5.6d The ac impedance spectra in the frequency range of 2 Hz to 10 MHz for the ceramic samples of $Li_{2+x}Y_xZr_{1-x}O_3$ with x=0.1.

the higher frequency range and an approximately horizontal part at low frequencies. These impedances seem to be different from the common well-known Cole-Cole impedances discussed by Cole, Jonscher and Isard, etc. [62,63,73,76,77] at the low frequency end because of the extra horizontal linear part in these impedance spectra. And they are also different from the Warburg diffusion impedances discussed by McDonald and others [62,78,79] in the linear part at low frequencies. The horizontal part is due to the induction from the silver electrode reaction with lithium at the initial stage of the measurements. The curved part at high frequency comes from the superposition of the two depressed semicircles in the Cole-Cole plot from the grain and grain boundary. It is not easy to separate the overlapping grain and the grain boundary components of the impedances. The total conductivity was obtained by extrapolating the curved part to the real axis. Although the conductivity can be obtained by using the real component of the impedance at its closest approach to the real axis, the different procedures generally yield less than 5% relative errors. The conductivity dependence on temperature for all the samples is shown in Fig.5.7 in the range 250 to 400°C. When the temperature is lower than 250°C, the conductivity of the samples is too low to be determined accurately.

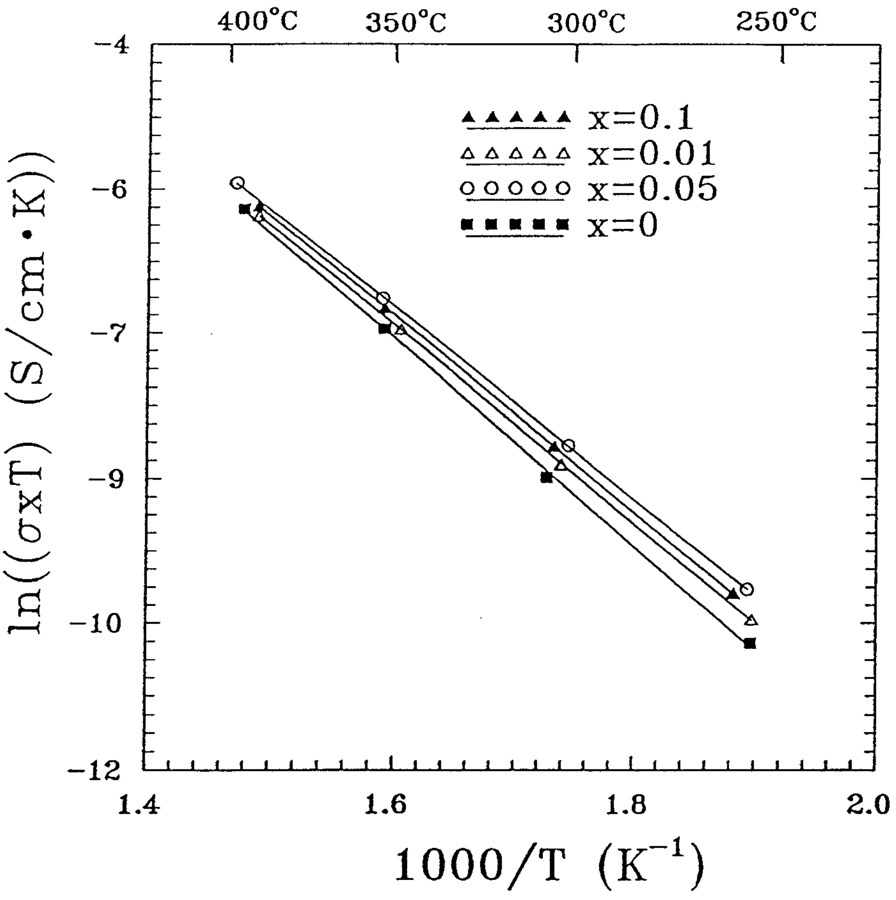

Fig.5.7 The dependence of the total conductivity on temperature for the samples of $Li_{2+x}Y_xZr_{1-x}O_3$.

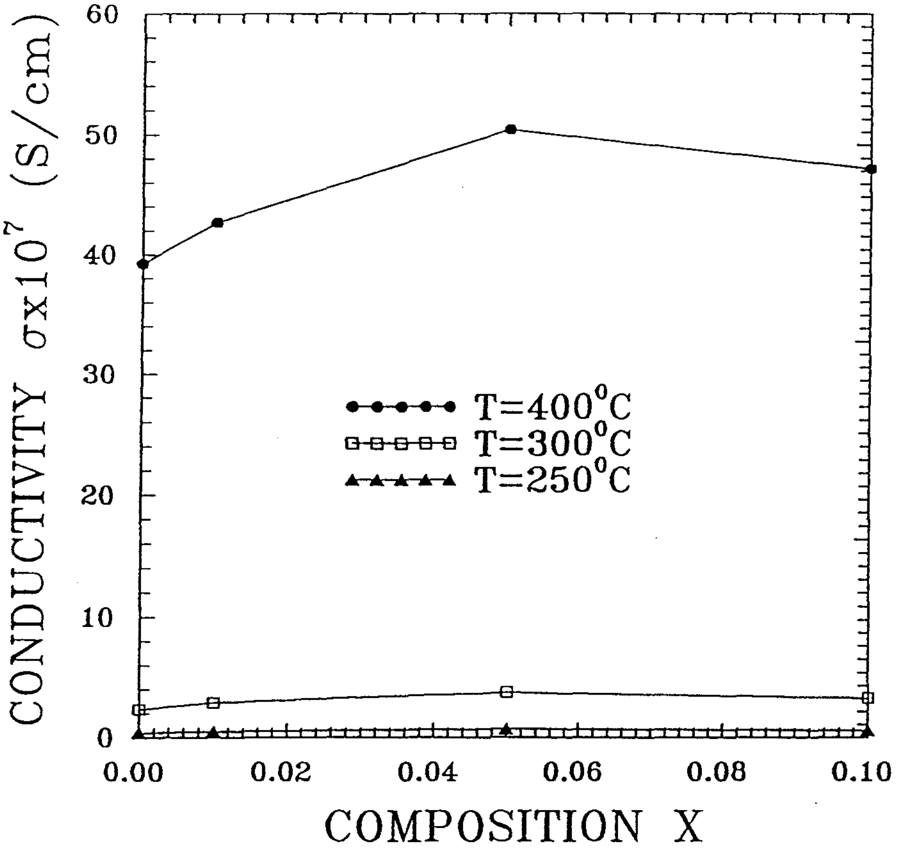

Fig.5.8 The dependence of the ionic conductivity on the composition x for the samples of $Li_{2+x}Y_xZr_{1-x}O_3$.

5-2 Yttrium-Doped Li_8ZrO_6

5-2-1 X-ray results

Power x-ray diffraction experiments were done using Cu-Kα radiation with Ni-filter for all sintered samples. The x-ray powder diffraction patterns for all the samples of $Li_{8+x}Y_xZr_{1-x}O_6$ are shown in Fig.5.9. From the patterns, it can be seen that when $x < 0.05$, all the diffraction peaks in the patterns match with that of Li_8ZrO_6. This shows the samples with x not larger than 5% are single phase with the same crystal structure of Li_8ZrO_6. But for the samples with $x > 0.10$, the diffraction pattern shows two phases exist, of which the major phase is still octalithium zirconate, and the minor phase is $LiYO_2$ with tetragonal structure.

In order to verify further that the added yttrium was dissolved into the crystal lattice of octalithium zirconate and study the effects of the yttrium doping on the crystal structure, the Guinier camera method was also used. The unit cell parameter a is shown in Fig.5.10. From Fig.5.10, it can be seen that the value of the a axis of the hexagonal structure for yttrium doped octalithium zirconate increases linearly with x until 5%, following Vegard's law. For the sample with $x=0.1$, the lattice parameter begins to deviate due

Fig. 5.9 X-ray diffraction patterns for $Li_{8+x}Y_xZr_{1-x}O_6$ Samples, A: with x=0, B: with x=0.01, C: with x=0.10, D: with x=0.05, E: with x=0.20, F: JCPDS card for monoclinic $LiYO_2$, G: JCPDS card for Li_8ZrO_6

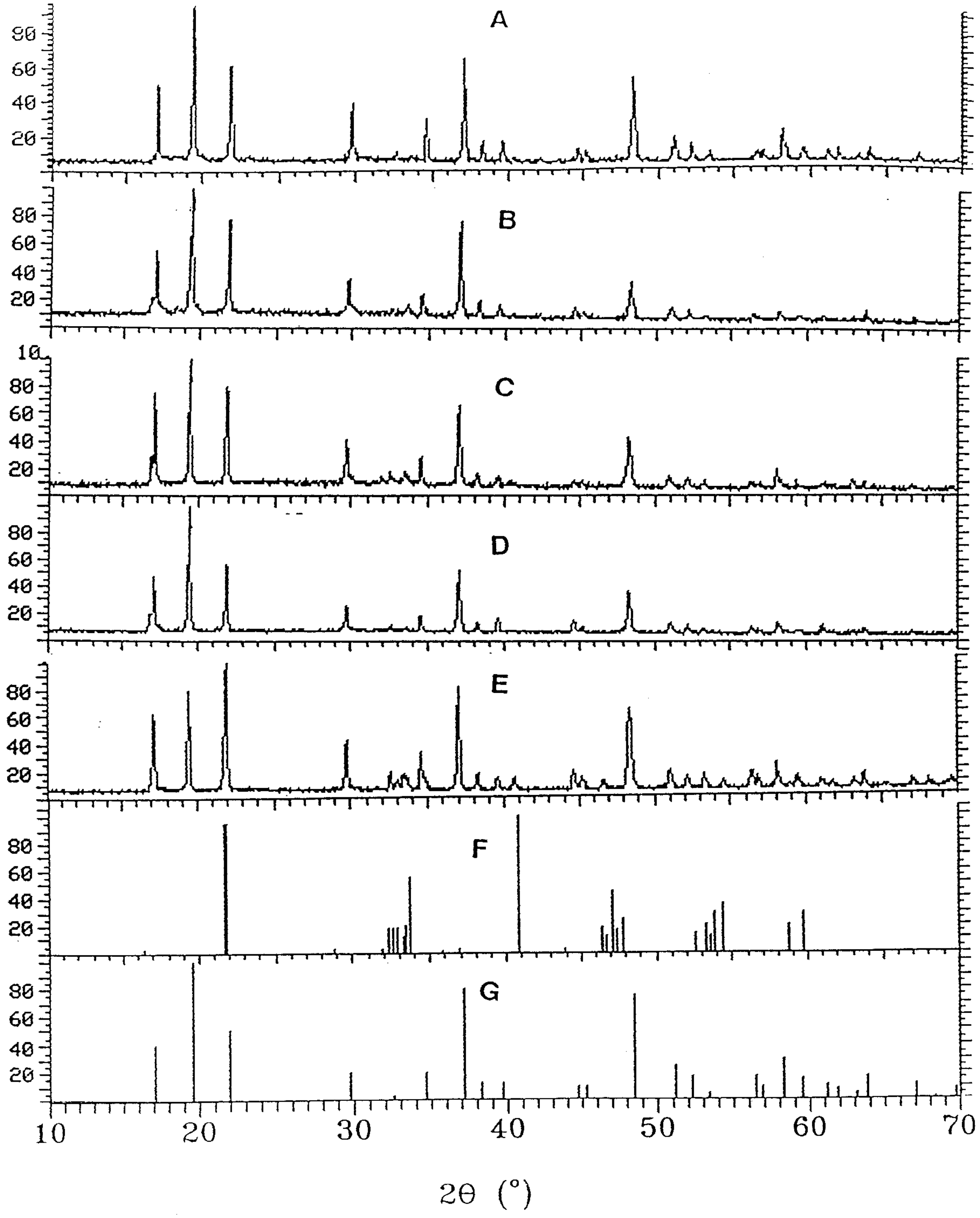
A
B
C
D
E
F
G
20
40
60
80
10
20
30
40
50
60
70
2θ (°)

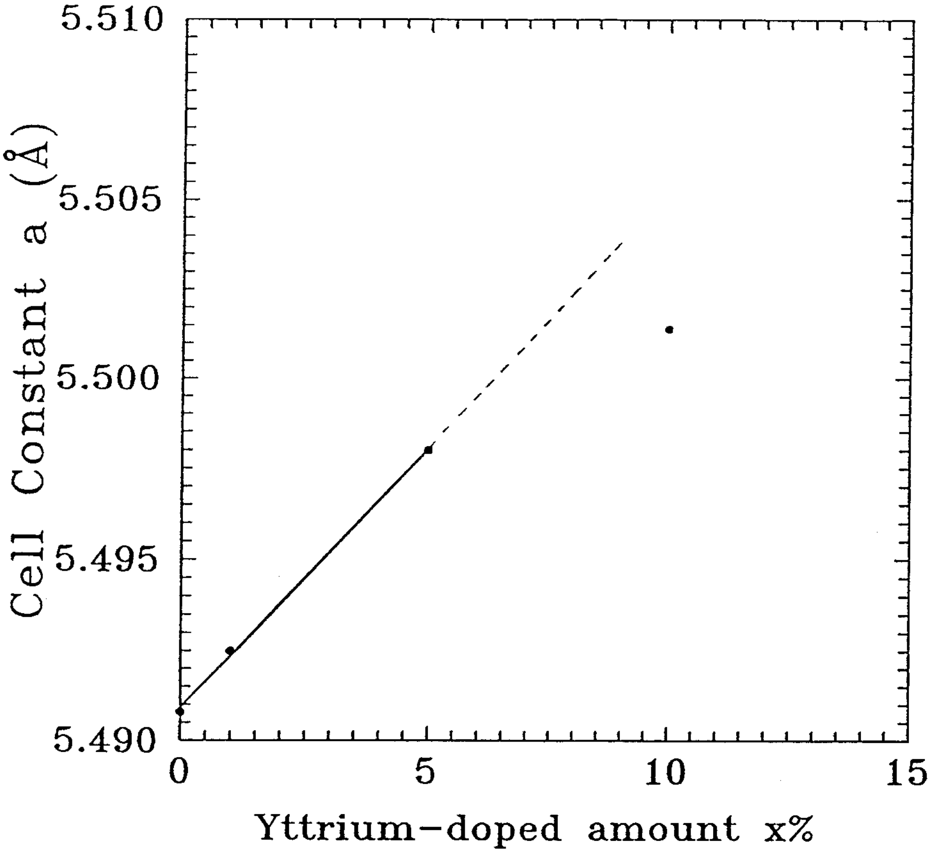

Fig.5.10 Cell Constant parameter (a axis) dependence on the yttrium-doped amount x for $Li_{8+x}Y_xZr_{1-x}O_6$ samples.

to formation of the $LiYO_2$ second phase. By extrapolation, the Y-doped amount in the lattice is 7%, i.e., 3% of the added yttrium has gone into the second phase.

The crystal structure of Li_8ZrO_6 [80,81] is shown in Fig.5.11. The oxygen ions form the stack of ABAB. Zirconium ions and some of the lithium ions(Li_I) occupy the octahedral sites. The other lithium ions(Li_{II}) occupy the tetrahedral sites. There are a number of possible ways to form a solid solution with yttrium in the Li_8ZrO_6 lattice. One typical way is that two yttrium ions substitute for two zirconium ions, resulting in an oxygen vacancy; another way is that four yttrium ions replace three zirconium ions, resulting in an interstitial yttrium ion; yet another way is that a yttrium ion substitutes for a zirconium ion combined with a lithium ion to form an interstitial lithium ion. However, from the consideration of the energy and kinetics, a Y^{3+} ion plus a Li^+ ion substituting for a Zr^{4+} ion is more favourable. The solid solution formed in the samples is $Li_{8+x}Y_xZr_{1-x}O_6$. A similar situation was verified for β-alumina doped with impurities by x-ray scattering, neutron scattering and electronic paramagnetic resonance of single crystals [82,83,84].

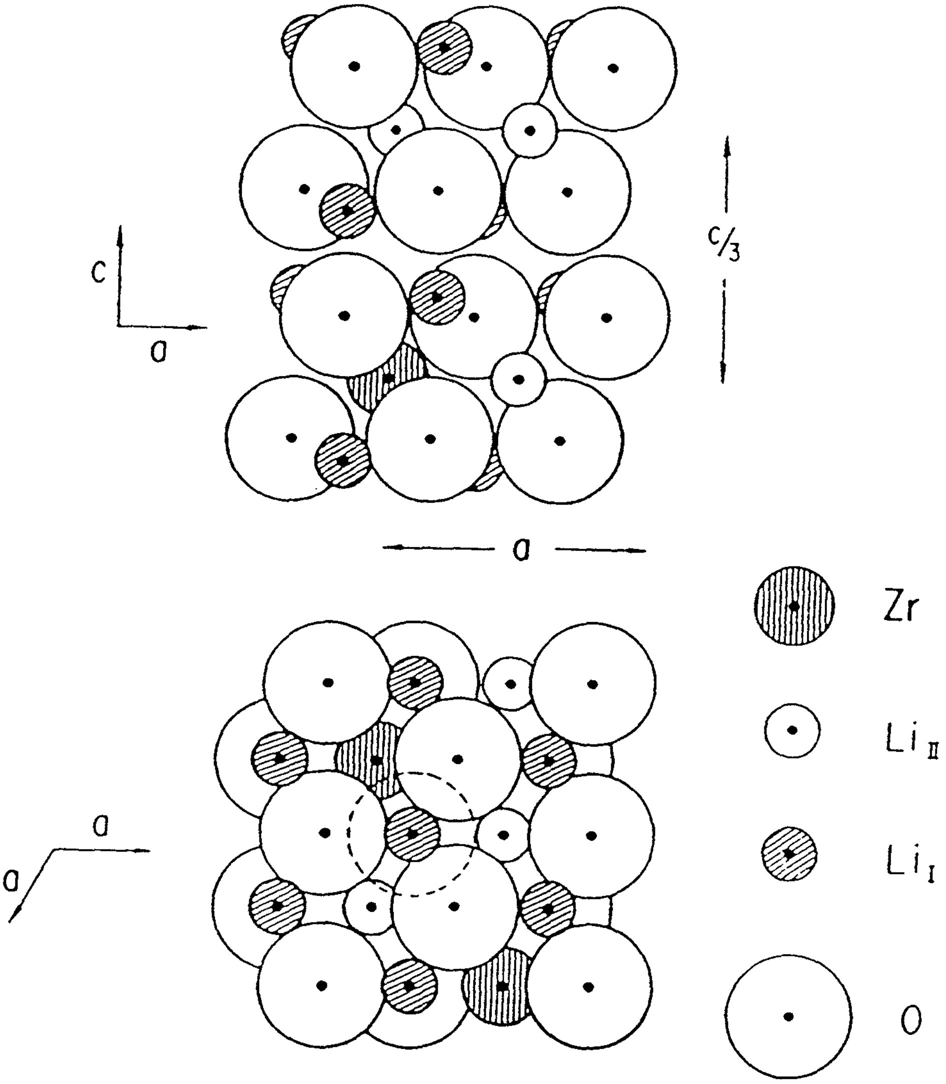

Fig.5.11 The arrangements of the ions in the crystal structure of Li_8ZrO_6. Lithium ions exist in octahedral (Li_I) and tetrahedral (Li_{II}) sites.

5-2-2 I.R. absorption spectrum analysis

The typical I.R. absorption spectra for the samples of $Li_{8+x}Y_xZr_{1-x}O_6$ after conductivity measurements are shown in Fig.5.12. From Fig.5.12, it can seen that in the wavenumber range 400-4000 cm^{-1}, there are 12 peaks. The peaks at 3436 and 3680 cm^{-1} are characteristic absorptions of lithium hydroxyl, especially the sharp peak of 3680 cm^{-1}[85,86,87], and 3570 cm^{-1} from $LiOH.H_2O$[88]. The peaks at 2500, 1090, 870 cm^{-1} are from the characteristic absorption of Li_2CO_3 [89,90]. The strong peaks at 1490 and 1440 cm^{-1} come from the superposition of the absorptions of Li_2CO_3 and LiOH [85,86,87,88,89]. The low wavenumber peaks at 600, 500, and 420 cm^{-1} may be from the $Li_{8+x}Y_xZr_{1-x}O_6$ solid solution.

From Fig.5.12, it can be seen that the characteristic peak of 3570 cm^{-1} from $LiOH.H_2O$ disappeared for sample PLZS3 with x=5%. This indicates that there is hardly any of the compound in the sample. Also, the peaks at 3680, 1440, 1490 cm^{-1} are significantly weaker than those of the PLZS12 sample without yttrium and of PLZS4 with a Y content of x=0.1. This shows that the relative contents of lithium carbonate and lithium hydroxyl in the sample with x=0.05 are much lower than those in the other samples.

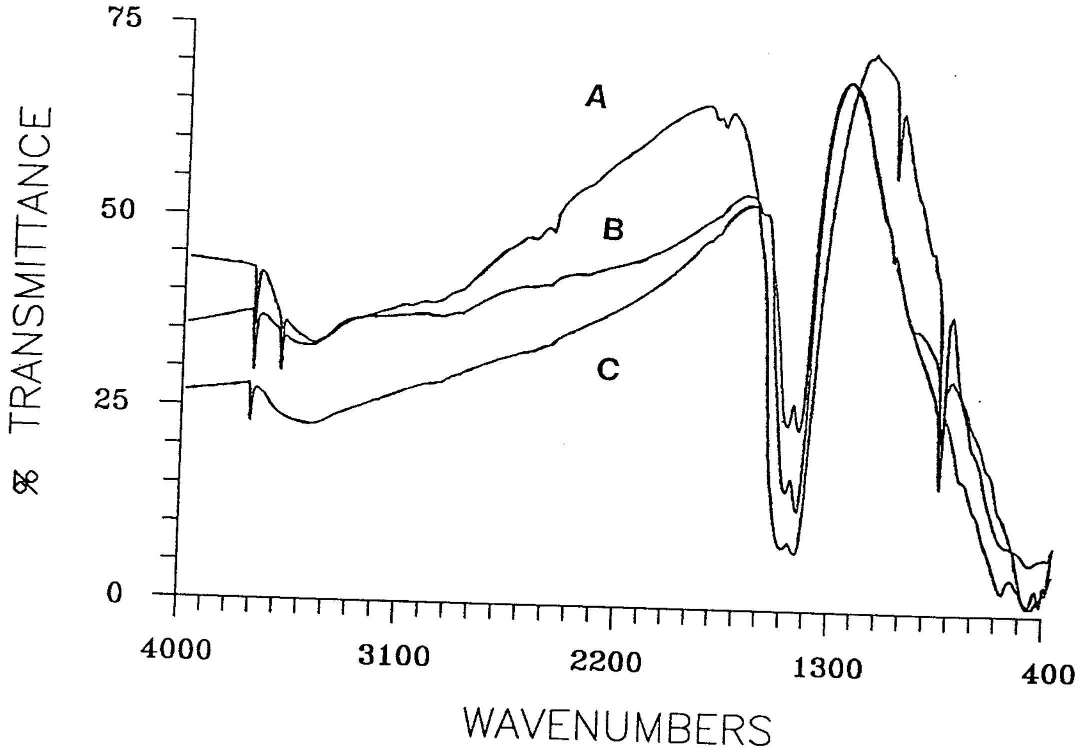

Fig.5.12 The I. R. Absorption spectra using KBr technique for $Li_{8+x}Y_xZr_{1-x}O_6$ samples after conductivity measurements, A: with x=0, B: with x=0.05, C: with x=0.10.

5-2-3 Thermal analysis

The typical DTA curves are shown in Fig.5.12 for the samples of $Li_{8+x}Y_xZr_{1-x}O_6$ after the conductivity measurement. From these curves, it is seen that there is one small endothermic peak near 430°C. From the previous I.R. absorption analysis, we know that LiOH, $LiOH.H_2O$ and Li_2CO_3 exist in the samples. The $LiOH.H_2O$ will decompose into LiOH and H_2O at 140°C [91]. Therefore, only LiOH and Li_2CO_3 mixtures exist in addition to the oxide phases. From the phase diagram of the binary system $LiOH-Li_2CO_3$ [92], it is known that there is one eutectic point at 418°C at a composition of 82.2 mol % LiOH. Therefore, the endothermic peak in the DTA curve comes from the melting of the mixtures of LiOH and Li_2CO_3. From the peak temperature and the phase diagram, it can also be estimated that the compositions of the mixtures in the samples are near the eutectic point.

5-2-4 SEM analysis

The typical SEM photo for the typical samples of ceramic $Li_{8+x}Y_xZr_{1-x}O_6$ after the conductivity measurements are shown in Fig.5.13. From the micrographs, it can be seen that the image from sample PLZS3 with x=0.05 is much different from the others. The grains in the PLZS3 sample are still clear and they form textured microstructures. Although it can be

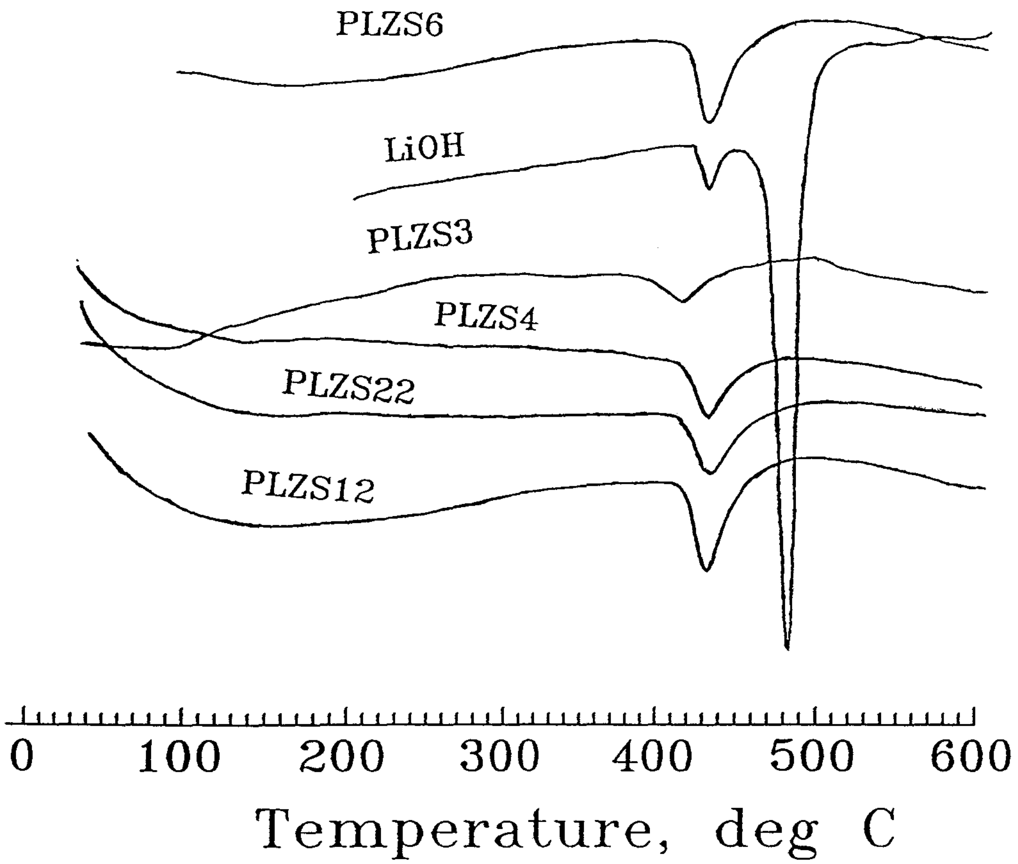

Fig.5.13 The DTA curves in argon atmosphere in the temperature range of 25 to 600°C for the samples of $Li_{8+x}Y_xZr_{1-x}O_6$ after conductivity measurements: PLZS12(x=0); PLZS22 (x=0.01): PLZS3(x=0.05); PLZS4(x=0.1): PLZS6(x=0.2).

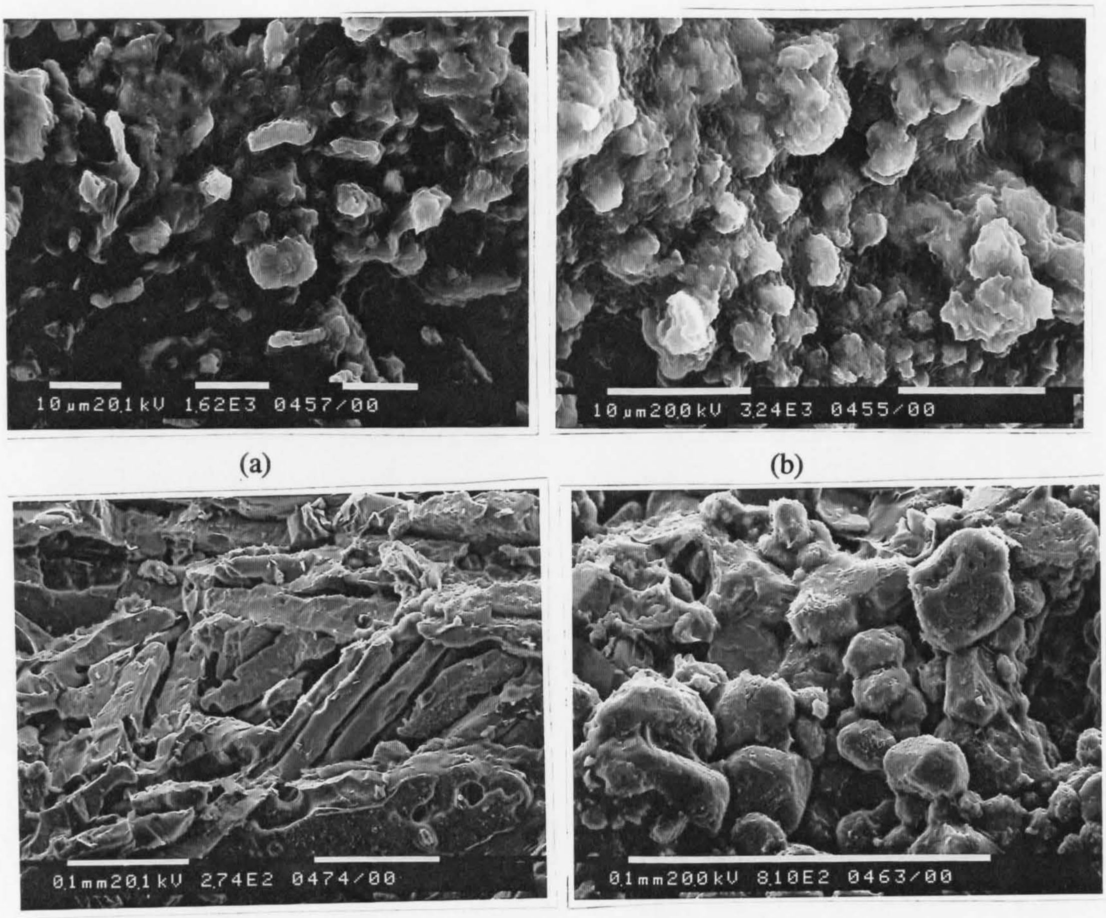

(a) (b)

(c) (d)

Fig.5.14 The SEM images of fracture surfaces for samples of $Li_{8+x}Y_xZr_{1-x}O_6$ after conductivity measurements with (a) x=0; (b) x=0.01; (c) x=0.05; and (d) x=0.10.

observed that some very fine particles exist on the surfaces and the grain boundaries of the solid solution particles, they did not cover the whole surface of the boundaries. But, for sample PLZS12 (without yttrium), sample PLZS22 (with x=0.01), and sample PLZS4 (with x=0.10), the particles are all not very clear, especially the PLZS12 and PLZS4 samples. It seems the very fine particles of lithium hydroxide and lithium carbonate have formed a continuous layer over the whole $Li_{8+x}Y_xZr_{1-x}O_6$ particles. This can be seen clearly in sample PLZS22. It can also be seen that all of the samples are not very dense, i.e., the porosities are large. The relative densities for all the samples are about 80% of theoretical density.

5-2-5 Conductivity results

The ac conductivity response of $Li_{8+x}Y_xZr_{1-x}O_6$ samples with silver electrodes in air when plotted in the complex impedance plane consisted, in order of decreasing impedance, of a low frequency spur downwards to the abscissa, and a high-frequency semicircular region which was centered below the axis. The intersection of these two regions was interpreted as the total conductivity of the samples, and is shown in Fig.5.15 as $\log(\sigma T)$ versus 1/T from 160°C to 440°C, and in Fig.5.16 at representative temperatures for all the samples.

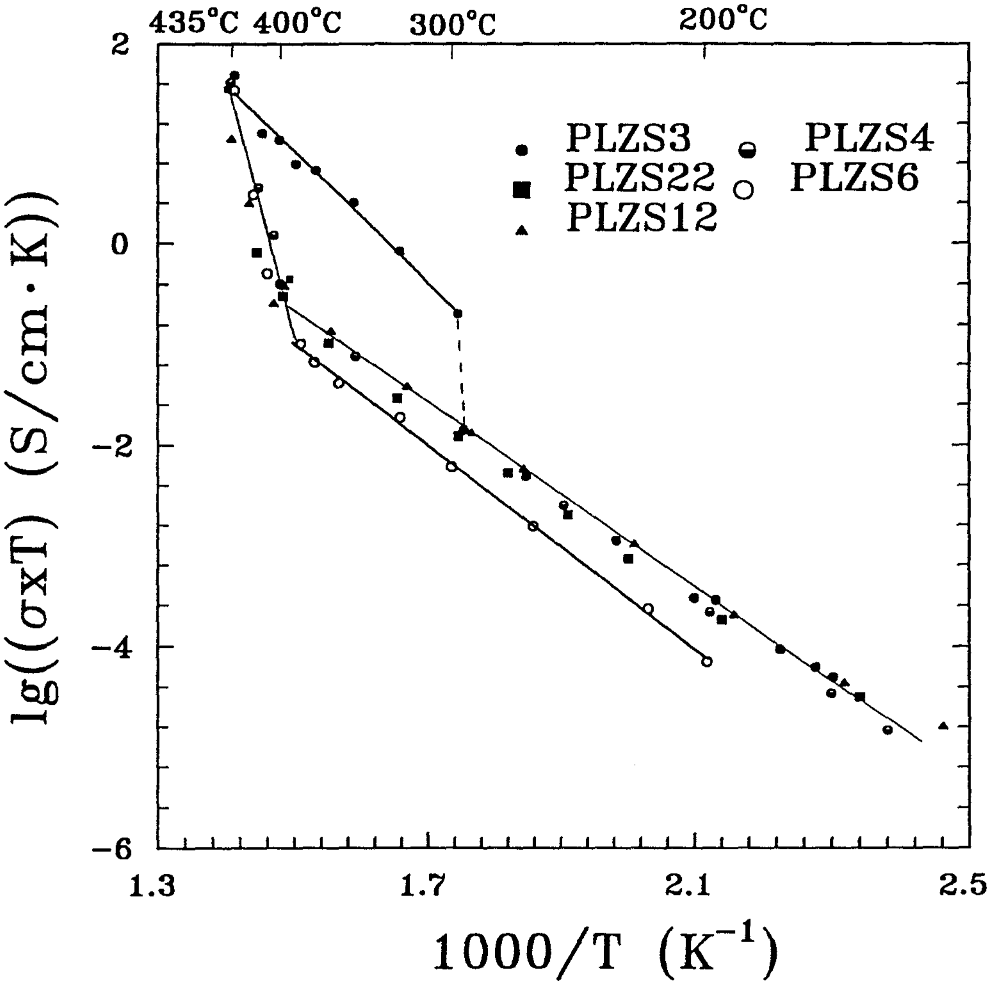

Fig. 5.15 The dependence of conductivity on temperature for the samples of $Li_{8+x}Y_xZr_{1-x}O_6$: PLZS12 (x=0); PLZS22 (x=0.01); PLZS3 (x=0.05); PLZS4 (x=0.10); PLZS6 (x=0.20).

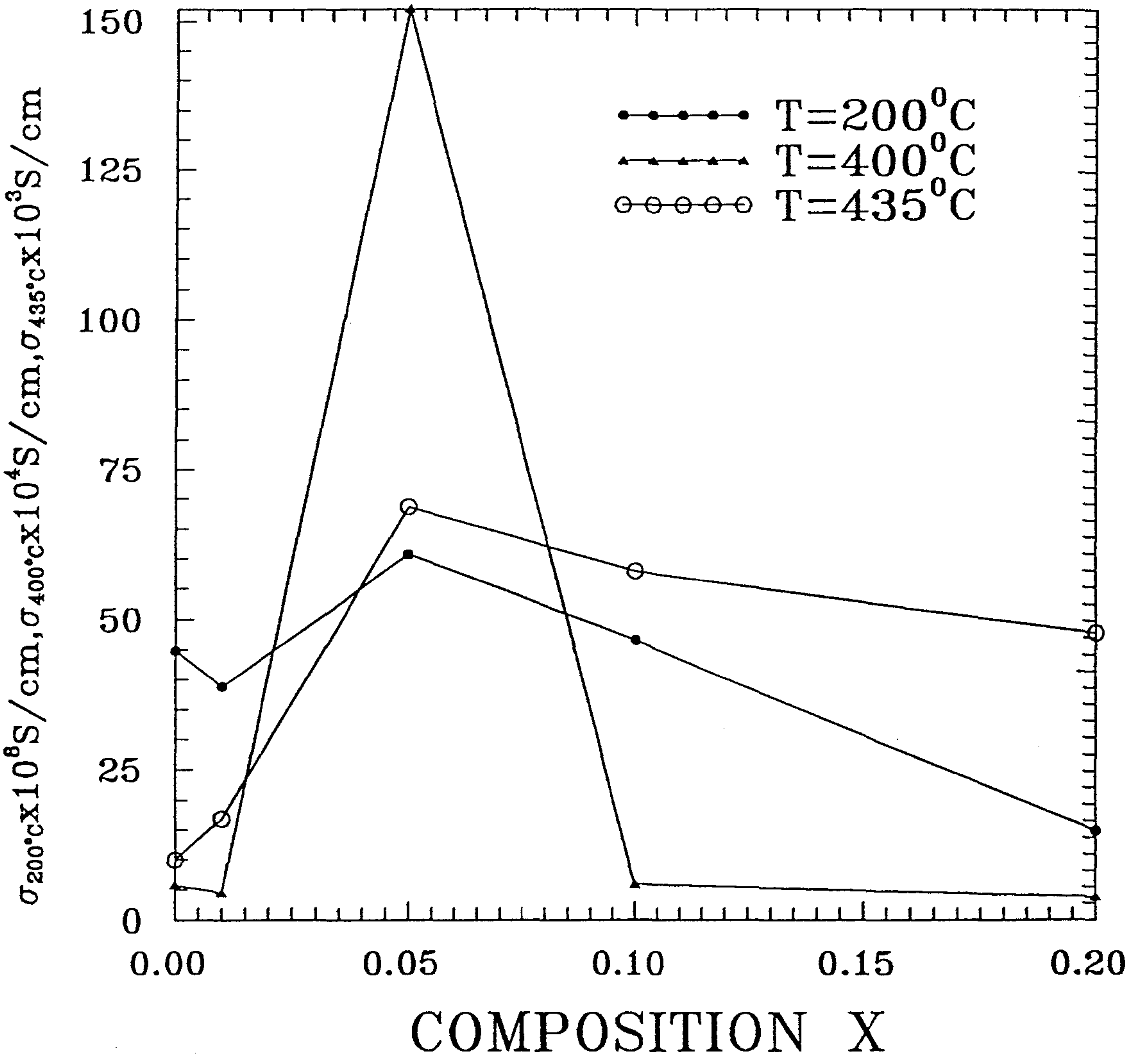

Fig.5.16 The ionic conductivity in the typical temperatures for samples of $Li_{8+x}Y_xZr_{1-x}O_6$.

In Fig.5.15, the linearly fitted lines are shown for samples PLZS12 (x=0) and PLZS6 (x=0.2) at low temperature ranges and for samples PLZS12 and PLZS3 (x=0.05) at high temperature ranges, respectively, in order to make the figure clear. But from Fig.5.15, it is seen that the log(σT) versus 1/T curves for all the samples can be fitted into two sets of straight lines. In other words, there is one transition point in the curves for the temperature range 160 to 440°C. For all the other samples except PLZS3 (x=5%) the transition temperature is around 400°C, while for sample PLZS3, the transition temperature is at 296 to 300°C. In the latter, the conductivity jumps by about one and half orders magnitude with a temperature increase from 296 to 300°C.

5-3 Zirconium-doped $LiYO_2$

5-3-1 XRD results

The X-ray powder diffraction pattern A shown in Fig.5.17, of undoped $LiYO_2$ was identical to the pattern of monoclinic $LiYO_2$ shown in JCPDS # 24-671. For the samples with compositions $Li_{1-x}Zr_xY_{1-x}O_2$, the XRD patterns depend on the x values when x is not larger than 0.1. When $0.1<x\leq0.2$ the second phase Y_2O_3 was detected, but the major peaks remained the same as those for $x<0.1$. However, when x reaches 0.3, another phase matching the $Zr_3Y_4O_{12}$ pattern from JCPDS file # 29-1389 was detected in addition to the $LiYO_2$ solid solution and Y_2O_3 phases. At $x\geq0.4$, Li_2ZrO_3(JCPDS # 20-647) appeared along with $Zr_3Y_4O_{12}$ and the solid solution phase.

Stewner and Hoppe [93] have discovered that $LiYO_2$ becomes tetragonal when impurity cations are present. In order to determine further the structure of Zr-doped $LiYO_2$, the sample with x=0.1 was studied by Guinier camera. The results show that the $LiYO_2$ with 10%(mol) ZrO_2 is tetragonal. The cell constants are as follows:

$a=4.396\pm0.004$ $c=10.443\pm0.002$

The diffraction data, both observed and calculated, are shown in Table 5.3.

Table 5.3 The diffraction data for Zr-doped $LiYO_2$ with composition of $Li_{0.9}Zr_{0.1}Y_{0.9}O_2$

$2\theta_{obs}$ (°)	d_{obs} (Å)	I/I_o	hkl	d_{cal} (Å)
			002	5.2217
21.96	4.0521	100	101	4.0521
29.18	3.0581	17	110	3.1088
32.80	2.7282	29	103	2.7292
33.51	2.6718	40	112	2.6108
34.30	2.6124	13	004	2.6108
41.01	2.1992	46	200	2.1982
			202	2.0260
			114	1.9993
46.99	1.9325	31	211	1.9322
48.24	1.8849	14	105	1.8866
			006	1.7406
53.46	1.7125	12	213	1.7120
54.52	1.6817	32	204	1.6816
59.38	1.5552	7	220	1.5544
61.01	1.5175	4	116	1.5187
			222	1.4898
64.10	1.4516	2	301	1.4513
65.13	1.4311	2	215	1.4316
			310	1.3903
			206	1.3646
69.54	1.3508	2	303	1.3507
69.99	1.3431	14	312	1.3435
70.46	1.3353	13	224	1.3356
72.37	1.3047	2	008	1.3054
			314	1.2271
79.02	1.2108	2	321	1.2111
79.88	1.1999	1	305	1.1997
			118	1.2036
			217	1.1885
			226	1.1594

Fig.5.17a X-ray diffraction patterns for the samples of $Li_{1-x}Zr_xY_{1-x}O_2$: A(x=0); B(x=0.005); C(x=0.01); D(x=0.01); E(x=0.1) and for JCPDS card :G($LiYO_2$, # 24-671).

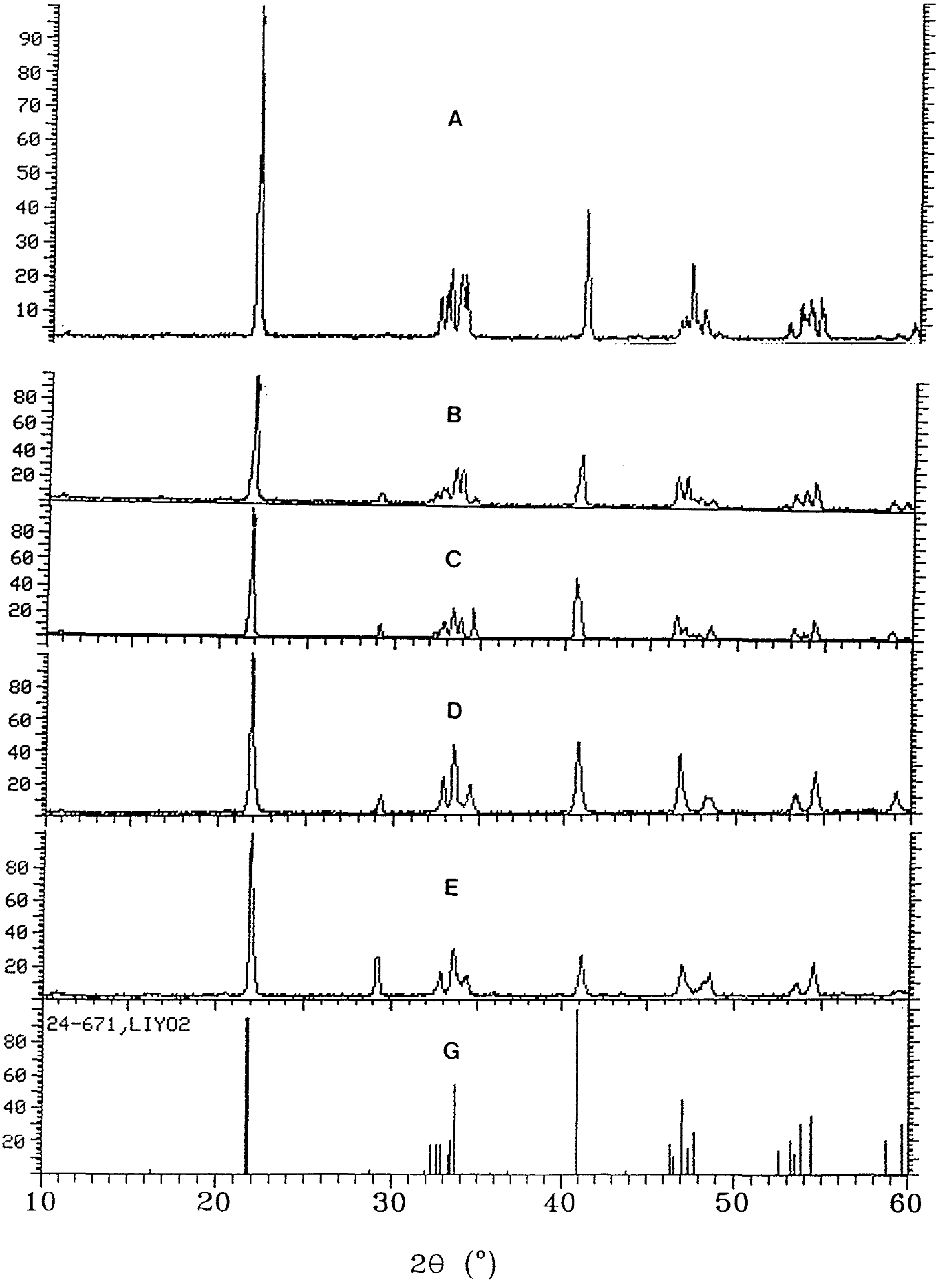
90
80
70
60
50
40
30
20
10
A
80
60
40
20
B
80
60
40
20
C
80
60
40
20
D
80
60
40
20
E
24-671,LIYO2
80
60
40
20
G
10
20
30
40
50
60
2θ (°)

Fig.5.17b X-ray diffraction patterns for the samples of $Li_{1-x}Zr_xY_{1-x}O_2$: H(x=0.15): I(x=0.2), and $Li_{1+x}Zr_xY_{1-x}O_{2+x}$: J(x=0.15); K(x=0.2); L(x=0.3) and for JCPDS cards: M($LiYO_2$, #24-671); N(Y_2O_3, #25-1200).

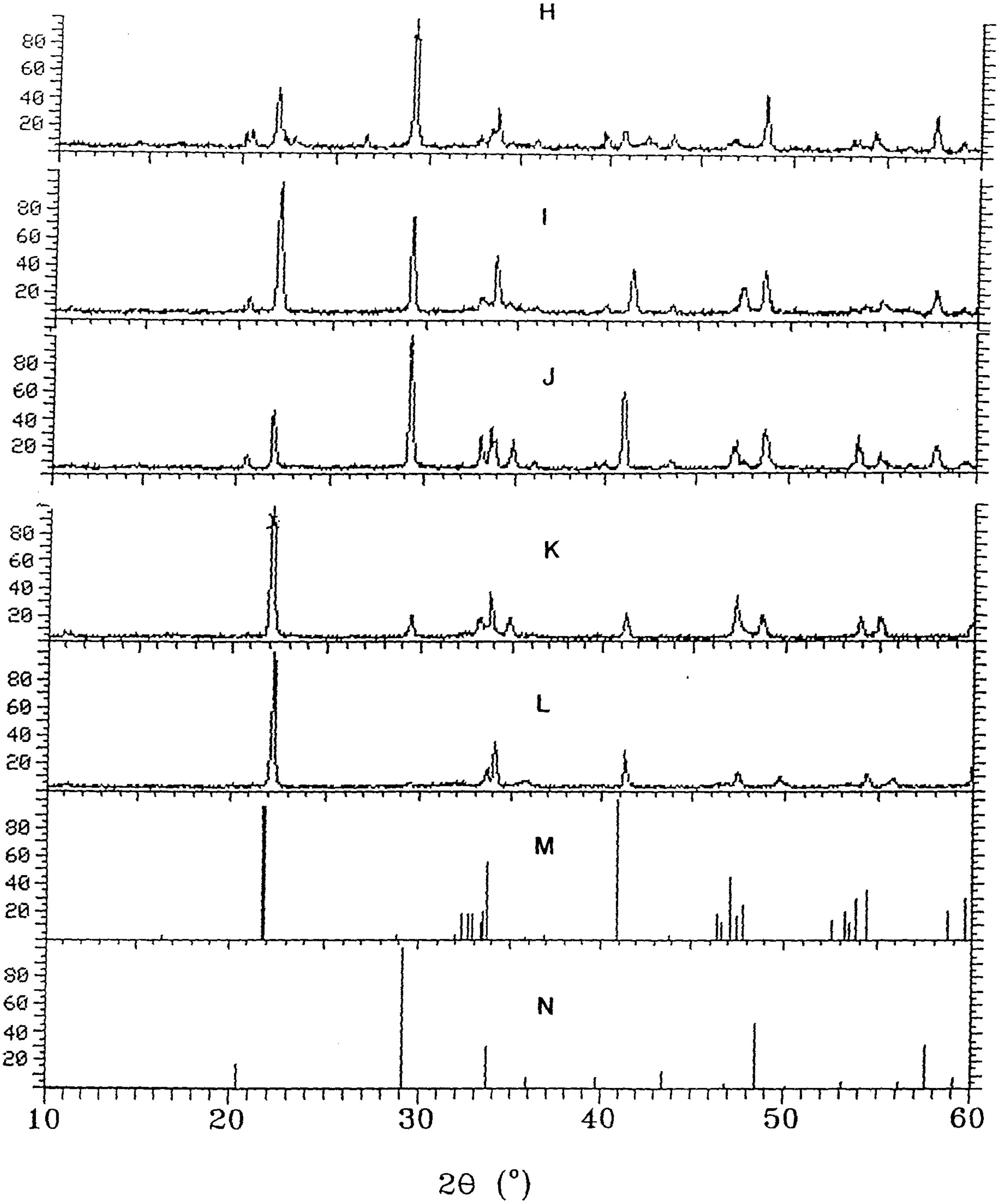
H
I
J
K
L
M
N
20
40
60
80
10
20
30
40
50
60
2θ (°)

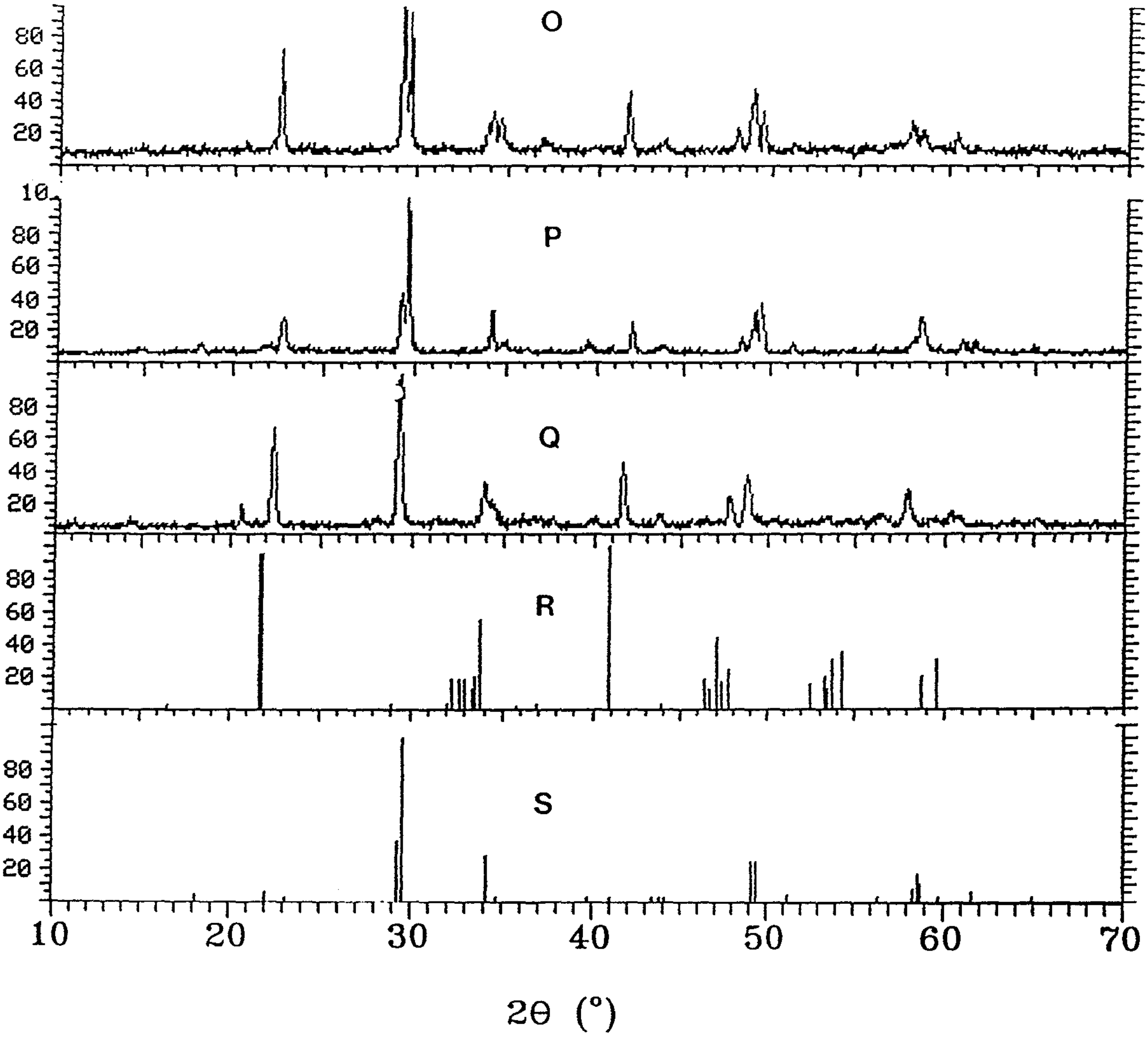

Fig.5.17c X-ray diffraction patterns for the samples of $Li_{1-x}Zr_xY_{1-x}O_2$: O(x=0.4); P(x=0.5); Q(x=0.3) and for JCPDS cards: R($LiYO_2$, #24-671); S($Zr_3Y_4O_{12}$, #29-1389).

Therefore, compared to pure $LiYO_2$ which is monoclinic, it is known that the samples of Zr-doped $LiYO_2$ form a solid solution $Li_{1-x}Zr_xY_{1-x}O_2$ with tetragonal structure at $0.005 \leq x \leq 0.1$, a two-phase region of the solid solution and Y_2O_3 at $0.15 \leq x \leq 0.2$, a mixture of three phases of the solid solution, Y_2O_3 and $Zr_3Y_4O_{12}$ at $0.3 \leq x < 0.4$, a mixture of three phases of the solid solution, and $Zr_3Y_4O_{12}$ and tetragonal Li_2ZrO_3 at $0.4 \leq x \leq 0.5$. The corresponding phase diagram is shown in Fig.5.1.

From the patterns in Fig.5.17 and Table 5.3, it is also known that the samples of $Li_{1+x}Zr_xY_{1-x}O_{2+x}$ are the tetragonal $LiYO_2$ phase at $0 < x \leq 0.3$. Then if the doping follows the $LiYO_2$-Li_2ZrO_3 line, the solubility of $Li_{1+x}Zr_xY_{1-x}O_{2+x}$ solid solution extends to at least 0.3.

From previous XRD results, it is known that pure $LiYO_2$ is monoclinic with $\underline{a}$=6.116 Å, $\underline{b}$=6.189 Å, $\underline{c}$=6.197 Å and β=118.6° (JCPDS #24-671). Therefore, it is a deformed cubic structure and also close to the tetragonal structure from the point of view of cell constants. The solid solution of $Li_{1-x}Zr_xY_{1-x}O_2$ ($0.005 \leq x \leq 0.1$) and $Li_{1+x}Zr_xY_{1-x}O_{2+x}$ ($0.15 \leq x \leq 0.3$) are tetragonal. The cell constants of tetragonal phase for x=0.1 and other solid solutions studied by Hoppe and Schepers[93], Bertaut and Gondrand[94] are listed in Table 5.4.

Table 5.4 Cell constants of tetragonal $LiYO_2$

	in this study[a]	by Hoppe and Schepers[93]	by Bertaut and Gondrand[94]
a(Å)	4.3965±0.004	4.38_8	4.44
c(Å)	10.443±0.002	10.60	10.3_5

a. the composition is $Li_{0.9}Zr_{0.1}Y_{0.9}O_2$.

From the above results, it is also known that the solution of zirconia in $LiYO_2$ changes from $Li_{1-x}Zr_xY_{1-x}O_2$ for $x \leq 0.1$ to $Li_{1+x}Zr_xY_{1-x}O_{2+x}$ for $x \geq 0.3$. This can be explained as follows. For the former solution, the corresponding substitution reaction is

$$Zr^{4+} = Y^{3+} + Li^{+} \qquad (5-1)$$

while for the latter solution, the corresponding reaction is

$$Zr^{4+} + Li^{+} + O^{2-} = Y^{3+} \qquad (5-2)$$

Since the ionic radius of Zr^{4+} is smaller than Y^{3+}, there will be larger deformation in the unit cell when zirconium substitution for yttrium follows reaction 5-1. However, the decrease from smaller Zr^{4+} for larger Y^{3+} will be counteracted by extra Li^+ and O^{2-} ions when the substitution follows reaction 5-2. Morever, the substitution reaction following reaction 5-2 is also more favourable from point of view of kinetics since mobility of lithium and oxygen ions are much larger than that of zirconium ions in the starting materials.

5-3-2 Conductivity

The typical ac complex impedance spectra for the sample of pure $LiYO_2$ are shown in Fig.5.18 for a frequency range from 2 Hz to 10 MHz. The impedance spectra for the other Zr-doped $LiYO_2$ samples are similar and are not shown. From Fig.5.18, it is seen that at high temperature, the impedance spectra only show the Warberg impedance. At the mid-temperature range, the spectra clearly show two parts. One is the Warberg impedance, the other is from the superposition of bulk and boundary impedances. At low temperature, the spectra are close to those at the middle temperature, consisting of

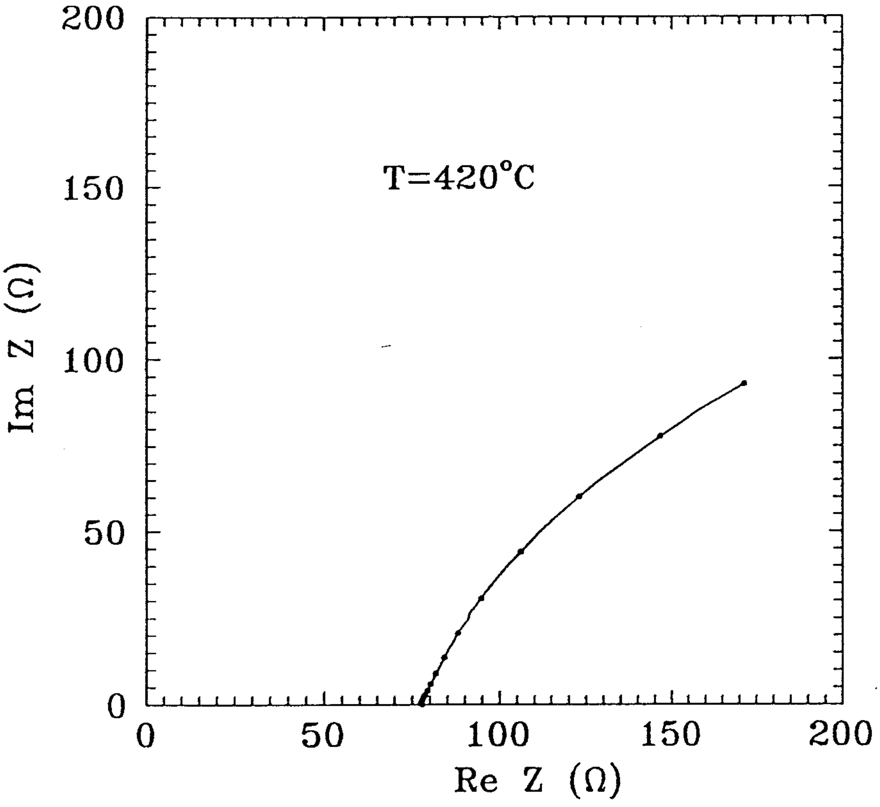

Fig.5.18a The ac impedance spectra for $LiYO_2$ in the frequency range of 2 Hz to 10 MHz at 420°C.

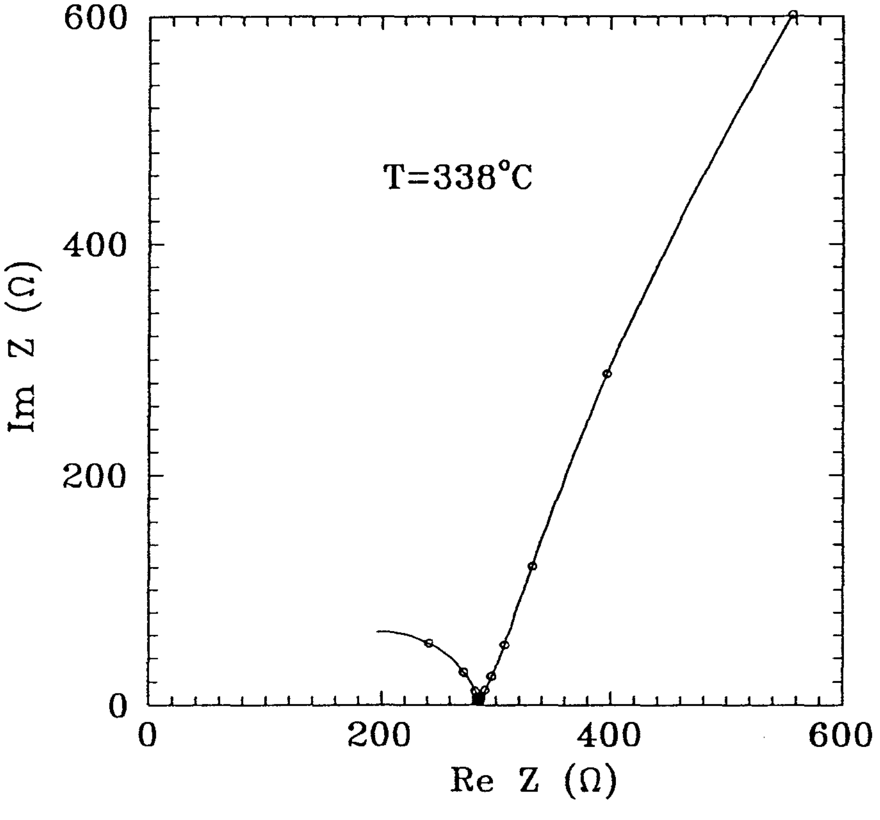

Fig.5.18b The ac impedance spectra for $LiYO_2$ in the frequency range of 2 Hz to 10 MHz at 338°C.

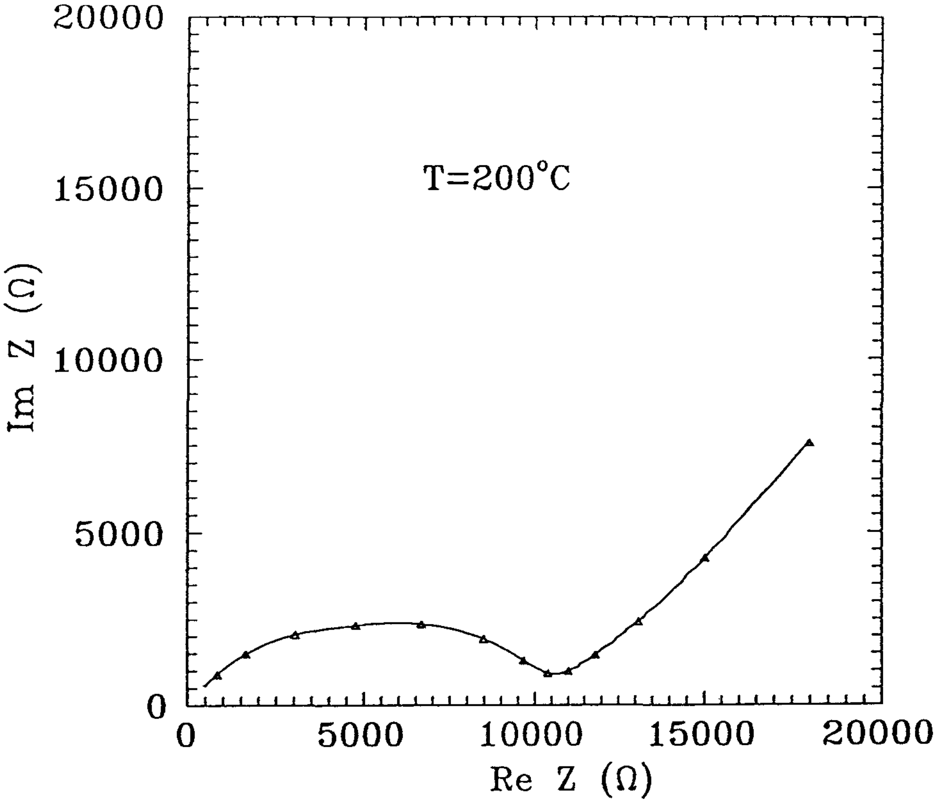

Fig.5.18c The ac impedance spectra for $LiYO_2$ in the frequency range of 2 Hz to 10 MHz at 200°C.

the Warberg impedance and the superposition of bulk and boundary impedances, but the superposition parts are more developed. In this present work, the separation of the bulk (grain) impedance and boundary impedance from their superposition is omitted. The total resistance is obtained from the natural intersection point of the Warberg part with the superposition part for low and middle temperatures, and from the natural intersection of the Warberg part with the real axis for high temperature since the superposition parts have not developed. Thus, the conductivity obtained is the total conductivity contributed from both grains and grain boundaries.

For the pure $LiYO_2$, and solid solutions of $Li_{1-x}Zr_xY_{1-x}O_2$ $(0<x\leq0.1)$ and $Li_{1+x}Zr_xY_{1-x}O_{2+x}$ $(0.2\leq x\leq0.3)$, the total conductivity dependence on temperature is shown in Fig.5.19. It is seen that there is a good linear relationship between conductivity times absolute temperature and reciprocal absolute temperature in the range measured. Thus, the correlation of conductivity and temperature follows Arrhenius' formula $\sigma T=\sigma_o\exp(E/RT)$. Also, it is seen that the undoped pure $LiYO_2$ has highest conductivity of all the samples. With the increase of doped amount x the conductivity of the solid solutions decreases significantly.

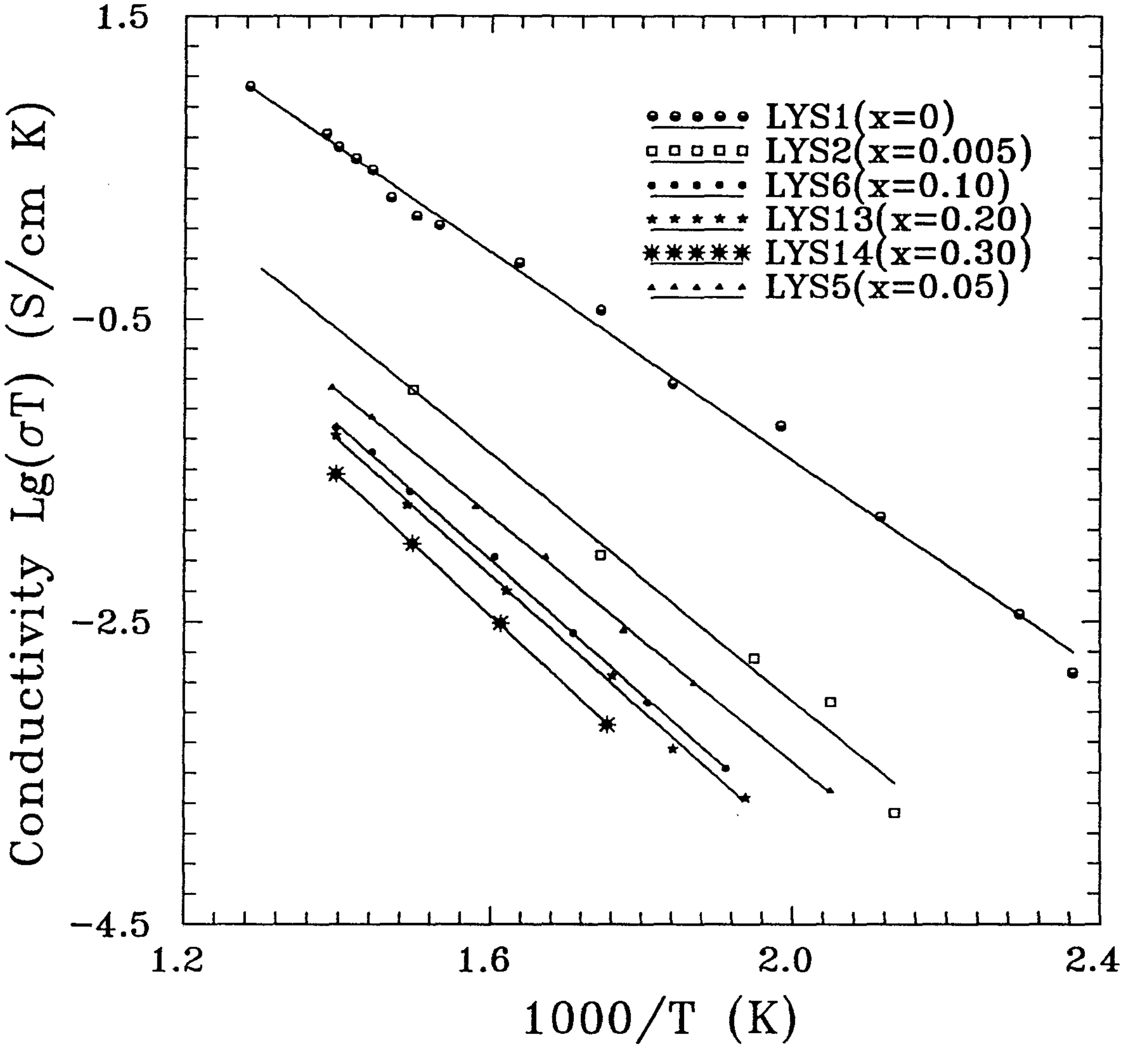

Fig.5.19 The dependence of conductivity on temperature for the samples of $Li_{1-x}Zr_xY_{1-x}O_2$ ($0\leq x\leq 0.1$) and $Li_{1+x}Zr_xY_{1-x}O_{2+x}$ ($0.15\leq x\leq 0.3$).

CHAPTER 6 DISCUSSION

The solubilities of yttrium in both Li_2ZrO_3 and Li_8ZrO_6 and zirconium in $LiYO_2$ have been reported in Chapter 5. The phase boundaries in the Li_2O-Y_2O_3-ZrO_2 ternary system and structures of the solid solutions have also been discussed. The conductivities of these materials have also been presented in the previous chapter. But the conductivity is affected by both crystal structure of the phases and microstructure of the sintered ceramics. A major effect is due to reaction of lithium compounds with the atmosphere, which results in the formation of hydroxide and carbonate eutectic. All of these effects will be considered further in this chapter.

6-1 Conductivity

6-1-1 Yttrium-doped Li_2ZrO_3

From Fig.5.7, it can be seen that there is a good linear relationship between the logarithm of conductivity σ times temperature T versus reciprocal temperature 1/T for all the samples. The relationship can be expressed by the formula

$$\sigma T = \sigma_0 \exp(-E/RT) \qquad (6\text{-}1)$$

where σ_0 is the preexponential factor, R is the gas constant and E is the activation energy. From the formula, the conduction activation energy for all the samples can be obtained. The results are given in Table 6.1.

It can also be seen from Fig.5.7 that the conductivity at 400°C increases from $3.9\text{x}10^{-6}$ to $5.0\text{x}10^{-6}$ S/cm as x varies from 0 to 0.05 and then decreases to $4.8\text{x}10^{-6}$ S/cm at x=0.1. Also the conductivity at 300 and 250°C increases slightly with x from 0 to 0.05, and then decreases slightly as x goes to 0.1. From Table 6.1, it can be seen that the conduction activation energy for the ceramic samples of $Li_{2+x}Y_xZr_{1-x}O_3$ decreases from 0.99 eV to 0.92 eV between x=0 and 0.05, and increases to 0.94 eV again for the sample with x=0.1.

For the sample with x=0, the conductivity and the activation energy are close to those reported by Hellstrom and Van Gool [95]. The discrepancies in the conductivity and activation energy may be caused mainly by different microstructures. From the dc measurements of Hellstrom and Van Gool [95], it is known that the maximum electronic transport number in Li_2ZrO_3 is less than 0.05 and that Li ion transport through the material is responsible for the conductivity. In the $Li_{2+x}Y_xZr_{1-x}O_3$ materials, the compositions under consideration all lie in the Li_2O-rich corner of the Li_2O -Y_2O_3 - ZrO_2 ternary system. Because of this, there is no free zirconia or

Table 6.1. The conduction activation energy of $Li_{2+x}Y_xZr_{1-x}O_3$

sample	composition x	conduction activation energy (kJ/mol)	conduction activation energy (eV)
ZYNS1	0	96±1	0.99±0.01
ZYNS2	0.01	90±0	0.94±0.00
ZYNS3	0.05	88±0	0.92±0.00
ZYNS4	0.1	90±0	0.94±0.00

zirconia-yttria solid solution which might give rise to oxygen conduction. Further, the temperatures under study would dictate that the oxygen ion contribution to conductivity remains negligible.

Combined with the previous results from XRD, IR, SEM and density determinations, the total conductivity change with composition x in $Li_{2+x}Y_xZr_{1-x}O_3$ ceramics comes from two contributions. One is from the crystal structure change because of the formation of the solid solution of $Li_{2+x}Y_xZr_{1-x}O_3$. The other is from microstructural changes such as the changes in the density (porosity), grain size, grain shape, and second phase effect. With the composition x increasing from 0 to 0.05, the density increases from 80.5 to 94.9 % T.D., while the conductivity at 400°C increases by 28.4%. Therefore, the formation of the solid solution does not significantly improve the lithium ion conductivity of Li_2ZrO_3. For the sample with x=0.1, although the density is higher than that of the sample with x=0.05, the conductivity is lower. This is mainly due to the second phase effect.

The increase of the bulk conductivity in the solid solution can be estimated from the effective medium theory. From the theory, the conductivity of the medium with porosity p is [96,97]

$$\sigma = 2\sigma_0(1-p)/(2+p) \qquad (6\text{-}2)$$

where σ_0 is the conductivity of the medium without pores. As an approximation, the porosity is taken as

$$p = 1 - \text{relative density} \qquad (6\text{-}3)$$

Then, from Table 5.2 in the previous chapter the following expressions are obtained:

for x=0, $\sigma_1 = 0.7372\sigma_{0,1}$ (6-4)

for x=0.01 $\sigma_2 = 0.7920\sigma_{0,2}$ (6-5)

for x=0.05 $\sigma_3 = 0.9211\sigma_{0,3}$ (6-6)

From equations 6-4, 6-5 and 6-6, we obtain

$$\sigma_{0,1} = 5.32\text{x}10^{-6} \text{ S/cm}$$

$$\sigma_{0,2} = 5.39\text{x}10^{-6} \text{ S/cm}$$

$$\sigma_{0,3} = 5.47\text{x}10^{-6} \text{ S/cm}$$

Thus, $\sigma_{0,2}$ is approximately 1% larger than $\sigma_{0,1}$ and $\sigma_{0,3}$ is 3% larger than $\sigma_{0,1}$. The conductivity increase may be due to the increase of lithium concentration in the lattice. The lithium conduction activation energy exhibits almost no change in the formation of the solid solution.

An essential part of any commercial fusion reactor will be a lithium-containing tritium breeder blanket. The breeder should have a wide operating temperature window and good thermal and mechanical properties, but perhaps the most important consideration is that the tritium inventory should be as low as possible. Thus the tritium release should be as high as possible. Tritium diffusion is a major factor controlling tritium release [98,99] and has a close relationship with lithium diffusion [100,101]. In addition to good heat and tritium conduction, the breeder blanket material must maintain its integrity over a long term. Therefore, a well-sintered material with small uniform grain size is essential [102]. All factors considered, the solid solution of $Li_{2+x}Y_xZr_{1-x}O_3$ and the two phase mixture of $Li_{2+x}Y_xZr_{1-x}O_3$ and $Li_6Zr_2O_7$ with composition $1.05Li_2O-0.05Y_2O_3-0.9ZrO_2$ show enhanced properties for tritium breeding applications.

6-1-2 <u>Yttrium-doped Li_8ZrO_6</u>

From Fig.5.15, the preexponential factors σ_o and conduction activation energy E are calculated from the Arrhenius formula $\sigma T = \sigma_o \exp(-E/RT)$, and the values are listed in Table 6.2 for all the samples.

The dc polarization experiments show the electronic conductivity for all the samples is less than $2.0\text{x}10^{-6}$ S/cm at 450°C, and $5.0\text{x}10^{-7}$ S/cm at 400°C. From the total conductivity data , shown in Figs.5.15 and 5.16, it can be seen that the electronic contribution to the total conductivity is less than 1% below 435°C.

Morever, the NMR experimental results for Li_8PbO_6 [81]

Table 6.2. The conduction activation energy and preexponential factors for $Li_{8+x}Y_xZr_{1-x}O_6$ samples.

		E (eV)		r_o(S/cm)	
Samples	x	HT$^{a)}$	LT$^{b)}$	HT	LT
PLZS12	0	5.2±0.3	0.89±0.02	$1.83x10^{38}$	$1.15x10^{6}$
PLZS22	0.01	4.0±0.9	0.96±0.02	$5.51x10^{39}$	$3.59x10^{6}$
PLZS3	0.05	1.3±0.0	0.89±0.01	$6.34x10^{10}$	$8.94x10^{5}$
PLZS4	0.1	5.5±0.3	0.98±0.02	$2.82x10^{40}$	$7.02x10^{6}$
PLZS6	0.2	5.2±0.3	0.95±0.02	$4.11x10^{38}$	$1.48x10^{6}$

a). HT means high temperature range which is from about 400 to about 440°C for all other samples except for PLZS3 for which it is from 300 to 440°C.

b). LT means low temperature range which is from about 160 to 400°C for all other samples except for PLZS3 for which it is from 160 to 400°C.

with the same crystal structure as Li_8ZrO_6 show that the conductivity is due to Li^+ ion conduction. From the XRD results, it is known that the crystal structures of the solid solutions of the yttrium-doped octalithium zirconate do not change except for a small shift in the lattice parameters. Therefore, the total conductivity for the yttrium doped octalithium zirconate conductors comes from the lithium ions, i.e. the contributions of the other ions and the electrons are neglected. The mobilities of the other ions, Zr^{4+}, Y^{3+}, and O^{2+} are much smaller than that of Li^+ ion because of the much larger ionic radii and higher electrical valences and lack of point defects below 450°C.

From Figs.5.15 and 5.16, it can be seen that the conductivity change with the amount of yttrium doping in the $Li_{8+x}Y_xZr_{1-x}O_6$ samples is not linear. Combined with XRD, DTA, IR spectra and SEM analyses, it can be seen that during the processing, the samples have absorbed some water vapour and carbon dioxide from the air and formed a LiOH + Li_2CO_3 mixture rich in LiOH. The melting point of the mixture is near 430°C. The phase diagram [92] is shown in Fig.6.1. At 435°C, the mixture of LiOH + Li_2CO_3 will be in a liquid state. It is also known that the mixture exists along the surfaces and grain boundaries of the $Li_{8+x}Y_xZr_{1-x}O_6$ particles. From Fig.5.11, it is seen that there are two kinds of Li^+ ions in the structure of Li_8ZrO_6, tetrahedral Li_I and octahedral Li_{II}. The Li_{II} ions have lower mobility than Li_I ions. Thus, the Li_8ZrO_6 is a pseudo-two-dimensional conductor[45]. As a result, the conductivity in the ceramic samples will depend to large degree on the microstructure as in β-alumina, but it will be more complicated because of the formation of the mixture of LiOH +

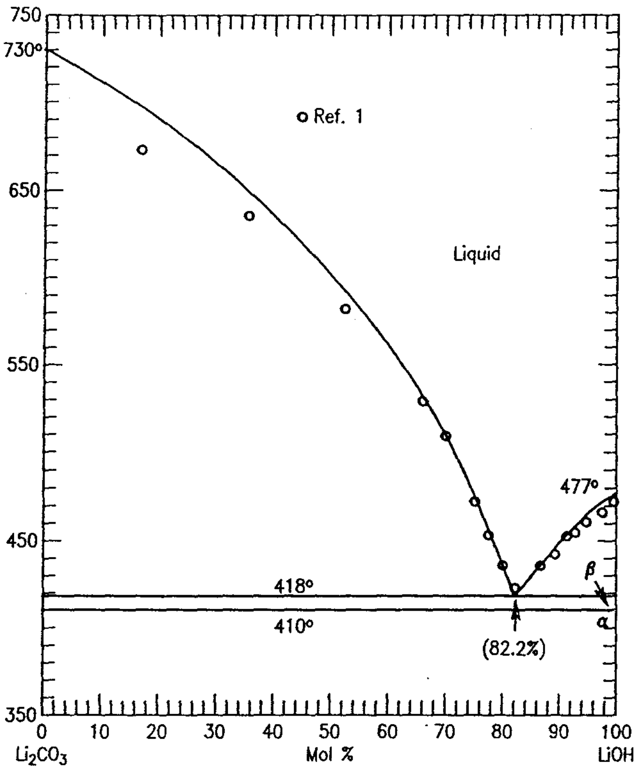

Fig.6.1 The phase diagram in the LiOH-Li_2CO_3 system.

Li_2CO_3 in processing of the Li_8ZrO_6. Then the lithium ion resistance consists mainly of four parts. One part, R_1, is from the solid solution crystals of $Li_{8+x}Y_xZr_{1-x}O_6$; the second part, R_2, is from the interphase interfaces between the oxides and the hydroxide-carbonate mixture; the third part, R_3, is from the contribution of the mixture phase and the other decomposed oxide phases; the fourth part, R_4, is from the contributions of the grain boundaries and interphase interfaces of the hydroxide-carbonate layer and the interphase interfaces between the mixture and the other decomposed compounds. But, for the samples of PLZS4(x=10%), and PLZS6(x=20%), there is one more contribution from the effects of the second phase of $LiYO_2$ on the resistivity.

At 435°C, the mixture of LiOH and Li_2CO_3 will be liquid, the total resistance in the $Li_{8+x}Y_xZr_{1-x}O_6$ samples will be mainly due to the contribution of the solid solution particles and also the $LiYO_2$ second phase (for sample PLZS4 and PLZS6) since the conductivity of molten LiOH is approximately 0.1 S/cm [46,103] and the solid solution and $LiYO_2$(for PLZS4 and PLZS6) are still dominant phases in the samples. From Fig.5.15, it is also known that with the increase of the yttrium doped amount x from 0 to 5%, the lithium ion conductivity at 435°C increases from $1.0x10^{-2}$ to $6.9x10^{-2}$ S/cm for the $Li_{8+x}Y_xZr_{1-x}O_6$ samples. The increase of the conductivity comes mainly from the effect of yttrium doping on the crystal structure of the solid solution of $Li_{8+x}Y_xZr_{1-x}O_6$. This increase may be due to the fact that the conductivity perpendicular to the c̲ axis in the pseudo-two-dimensional conductors of $Li_{8+x}Y_xZr_{1-x}O_6$ crystals improves due to the formation of interstitial Li^+ ions in the solid solution.

At around 400°C, it is known from the DTA results that the mixture of LiOH and Li_2CO_3 will begin to soften. Then the contributions to the total resistance from the R_2, R_3, and R_4 will dramatically decrease since the resistivity of LiOH will decrease drastically [46,103]. As a result, there exists a transition point at around 400°C in the $\log(\sigma T)$ vs. 1/T curves for the PLZS12(x=0), PLZS22(x=0.01), PLZS4(x=0.1) and PLZS6(x=0.2) samples. From the study on Li_5AlO_4 and other Li_2O-based materials by Johnson et al. [46,103], a similar increase in conductivities at about 400°C was observed.

But, for sample PLZS3(doped with 5% yttrium), the transition point is at 296°C and the conductivity dependence on the temperature is also significantly different from the others at $T \geq 300°C$, as shown in Fig.5.15 and Table 6.2. The exact reasons are not clear, but it might be explained as follows. From the SEM, IR spectra and DTA results, it is known that the plate-like particles form a textural microstructure with larger size whereas the hydroxide-carbonate mixture is more sparsely distributed than in the other samples. Although a continuous layer of the LiOH + Li_2CO_3 mixture was not seen, a very thin continuous film may have formed at the grain boundary during the processing. Therefore, the great difference in microstructures may account for the different conductivity behaviour at T>296°C.

At the low temperature range (T< 400°C for all the samples except PLZS3 for which it is at T<296°C), the contributions of R_2, R_3, and R_4 to the total resistance will be large since the conductivities even in pure LiOH [46,103], Li_2ZrO_3 and Li_4ZrO_4 [95] are much lower than that of Li_8ZrO_6[45] since Li_8ZrO_6 is a pseudo-two-dimensional lithium conductor. As a result, the conductivity behaviour of polycrystalline solid solution of $Li_{8+x}Y_xZr_{1-x}O_6$ was obscured by the effect of the mixture of LiOH + Li_2CO_3. Therefore the conductivities in the low temperature range overlap for samples PLZS12, PLZS22, PLZS3 and PLZS4. But, for sample PLZS6, the conductivity is significantly lower. This is mainly from the extra contribution of the second phase $LiYO_2$ to the total resistance.

The lithium conduction activation energies in the low temperature range for the $Li_{8+x}Y_xZr_{1-x}O_6$ samples are close to the result reported for Li_8ZrO_6 by Delmas and Hagenmuller el al [46]. But the conductivities are about one order magnitude lower than that reported in the low temperature range, while the conductivity for sample with x=5% is close to the values for Li_8ZrO_6 reported by them at temperatures above 300°C. Although they had measured the conductivity at temperatures up to 400°C, they reported data only below 360°C. This also implies that the conductivity in the samples is not dominated by the bulk behaviour of the $Li_{8+x}Y_xZr_{1-x}O_6$ grains below the melting point of the mixture of LiOH + Li_2CO_3.

6-1-3 Zirconium-doped $LiYO_2$

From Fig.5.19, the conductivity dependence on the Zr-dopant amount x can be obtained, as shown in Fig.6.2 for typical temperatures of 500, 400, and 200°C. From Fig.6.2, it can be seen that the conductivity drops from 1.3×10^{-2} to 1.2×10^{-4} S/cm at 500°C, from 3.2×10^{-3} to 1.8×10^{-5} S/cm at 400°C, and from 4.9×10^{-4} to 1.1×10^{-6} S/cm at 300°C with the increase of x from 0 to 0.3. Also the conductivity for the sample with x=0.005 is over one order magnitude lower than the corresponding one for pure $LiYO_2$ (x=0).

From Fig.5.19 and Arrhenius' formula $\sigma T=\sigma_o \exp(-E/RT)$, the preexponential factor σ_o and conduction energy E can be obtained for the pure $LiYO_2$ and solid solutions of $Li_{1-x}Zr_xY_{1-x}O_2$ ($0.005\le x\le 0.1$) and $Li_{1+x}Zr_xY_{1-x}O_{2+x}$ ($0.2\le x\le 0.3$), as shown

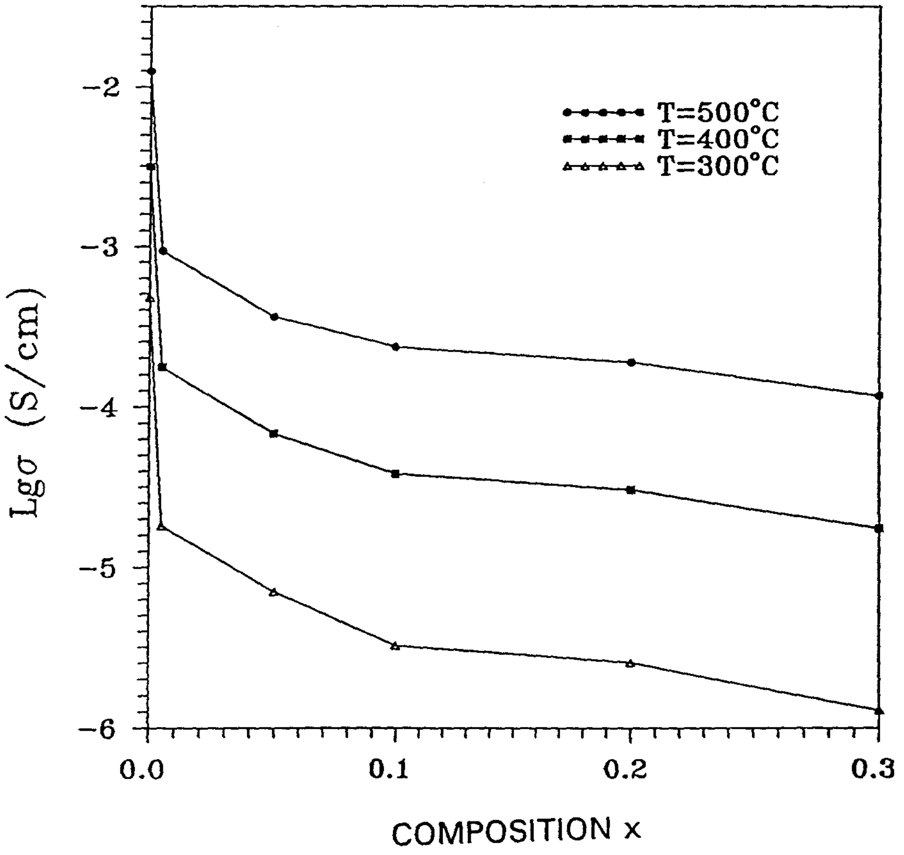

Fig.6.2 The depedence of conductivity on composition x for the samples $Li_{1-x}Zr_xY_{1-x}O_2$ ($0 \le x \le 0.1$) and $Li_{1+x}Zr_xY_{1-x}O_{2+x}$ ($0.2 \le x \le 0.3$).

in Table 6.3. From the table, it can be seen that the conduction energy for pure $LiYO_2$ is much smaller than those for the Zr-doped solid solutions. Also, the preexponential factor σ_o for pure $LiYO_2$ is larger than those for the Zr-doped solid solutions, but they have the same order of magnitude.

Biefeld and Johnson [46], also studied the conductivity of $LiYO_2$ and the mixture of $LiYO_2$ with Li_2O. They obtained totally different results. The activation energy for $LiYO_2$ was 0.82 eV in a dry environment and 0.96 eV in a wet environment, respectively. The conductivity was several orders of magnitude lower than that of our measurements for $LiYO_2$. They also found that the conductivity of $LiYO_2$ jumped suddenly at around 400°C in a wet environment. And they claimed that

Table 6.3 The preexponential factor σ_o and conduction activation energy for pure $LiYO_2$ and solid solutions of $Li_{1x}Zr_xY_{1x}O_2$ ($0.005 \leq x \leq 0.1$) and $Li_{1+x}Zr_xY_{1-x}O_{2+x}$ ($0.2 \leq x \leq 0.3$)

x	0	0.005	0.05	0.1	0.2	0.3
$r_o x10^{-4}$(S/cm)	26.8	13.9	5.13	9.12	7.97	8.61
E (eV)	0.68±0.01	0.81±0.03	0.81±0.01	0.87±0.002	0.88±0.01	0.92±0.01

this was caused by LiOH formed due to hydrolysis of $LiYO_2$ in the wet environment.

From our theoretical calculations in next section, it is shown that $LiYO_2$ is stable against hydration, even in an environment with a combination of water vapor and CO_2. Then, it is unlikely for $LiYO_2$ to react with water vapor and form LiOH and/or Li_2CO_3. The conductivity jump in their work may be explained by the reaction of Li_2O with water vapor and CO_2.

6-2 Thermodynamic Stability

6-2-1 Thermodynamic data calculations

Enthalpies of formation of $Li_6Zr_2O_7$ and $LiYO_2$ are not available, but the enthalpies for Li_2ZrO_3, Li_4ZrO_4 and Li_8ZrO_6 have been measured by Neubert and Guggi [44]. Based on the research on standard enthalpies of formation of inorganic compounds by Swalin [104] and Kubaschewski, Alcock and Evans [105], there is an excellent correlation between the enthalpies and the molar volume changes of the compounds formed from the elements (Fig.6.3). From this correlation and the values of the molar volume changes of Li_6ZrO_7 and $LiYO_2$, the standard enthalpies of formation of Li_6ZrO_7 and $LiYO_2$ were determined to be -2680 and -1420 kJ/mol, respectively. Good agreement was found when this method was applied to check the enthalpy of Li_5AlO_4, another lithium ion conducting compound. The experimental value of the standard enthalpy of formation was

-2365 kJ/mol [106], whereas the value obtained from the correlation in Fig.6.3 was -2366 kJ/mol.

The data for heat capacities and entropies of $Li_6Zr_2O_7$, Li_4ZrO_4, Li_8ZrO_6, and $LiYO_2$ are also not available. Since the heat capacities and entropies for Li_2ZrO_3, Li_2O, ZrO_2

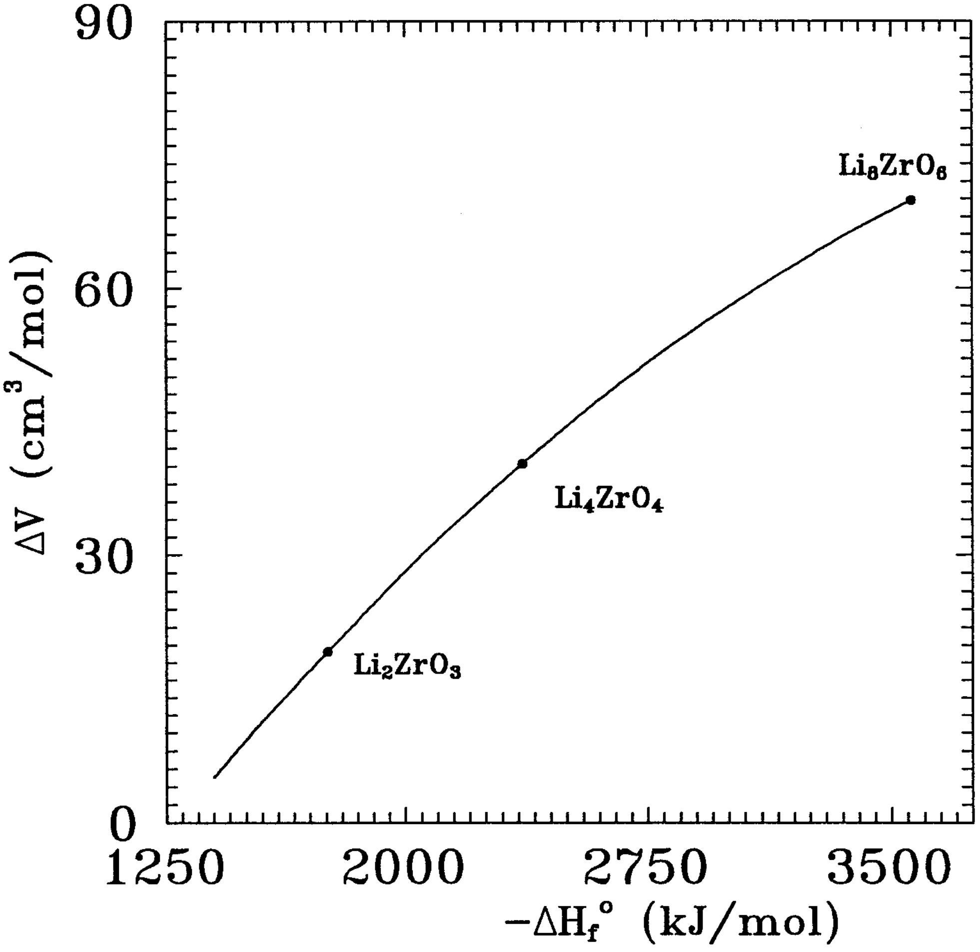

Fig. 6.3 The correlation between standard enthalpy of formation and molar volume change after forming compounds from their components for lithium compounds.

and Y_2O_3 are known [106], the missing values can be calculated from the Neumann-Kopp rule and the third law. The results are shown in Table 6.4. From Table 6.4, it is known that the relative errors of calculated C_p and S^o values for Li_2ZrO_3 are less than 5%, compared with the experimental values.

Table 6.4. Calculated or experimental thermodynamic data for lithium compounds at 298 K

	C_p (J/mol•K)	S^o (J/mol•K)	ΔH_f^o (kJ/mol)
Li_2ZrO_3	110.3	88.0	-1756[b]
	110.3[a]	91.6[a]	
$Li_6Zr_2O_7$	274.6	220.8	-2678
Li_4ZrO_4	164.4	129.2	-2364[b]
Li_8ZrO_6	272.6	204.4	-3562[b]
$LiYO_2$	78.3	68.3	-1423

a. these data are experimental values from reference [106].

b. these ΔH_f^o values are from experiments [44].

6.2.2 Thermal Stability Calculations

Li_8ZrO_6 will decompose on heating because of the evaporation of lithium oxide. The decomposition reactions are given as:

$$Li_8ZrO_6 = Li_4ZrO_4 + 2Li_2O(g) \quad (1)$$

$$Li_8ZrO_6 = 0.5Li_6Zr_2O_7 + 2.5Li_2O(g) \quad (2)$$

$$Li_8ZrO_6 = Li_2ZrO_3 + 3Li_2O(g) \quad (3)$$

$$Li_8ZrO_6 = ZrO_2 + 4Li_2O(g) \quad (4)$$

The decomposition reactions 3 and 4 are the combination of reactions 1 and 2 and the following reactions

$$Li_4ZrO_4 = Li_2ZrO_3 + Li_2O(g) \quad (5)$$

$$Li_2ZrO_3 = 2Li_2O(g) + ZrO_2 \quad (6)$$

From Table 6.4 and the thermodynamic data [106], ΔH^o, ΔS^o and ΔG^o can be calculated as shown in Table 6.5.

Table 6.5 Thermodynamic values for reactions 5 and 6

	ΔH^o_{298}(kJ)	ΔS^o_{298}(J/K)	ΔG^o_{298}(kJ)
reaction 5	447.7	306.8	356.3
reaction 6	497.9	252.7	422.2

Since the Gibbs free energies of reactions 3 and 4 will be larger than those for reactions 1 and 2, respectively, only reactions 1 and 2 need to be considered in thermal stability calculations. Furthermore, Li_2O vapour can decompose into lithium gas and oxygen gas according to decomposition reactions as follows:

$$Li_8ZrO_6 = Li_4ZrO_4 + 4Li(g) + 2O_2(g) \tag{8}$$

$$Li_8ZrO_6 = 1/2Li_6Zr_2O_7 + 5Li(g) + 5/4O_2(g) \tag{9}$$

For reaction 8, the equilibrium constant is expressed as

$$K_{p,1} = P^{4}_{Li}xP_{O}{}^{2} \tag{6-7}$$

In vacuum or an atmosphere with initial $P_{O_2}=0$, based on the assumption that the decomposition reaction is controlled by the effusion of the gas products at the steady state, from the Hertz-Knudsen equation [107], $K_{p,1}$ of the dynamic equilibrium of the steady decomposition can be expressed as

$$K_{p,1} = (M_{O_2}/M_{Li})^{1/2}xP_{Li}/4 \tag{6-8}$$

where M_i is the molar mass of species i. For reaction 9, in vacuum or an atmosphere with $P_{O_2}=0$, the corresponding equilibrium constant is

$$K_{p,2}=(M_{O}2\ /M_{Li})^{5/8}xP_{Li}^{25/4}/4^{5/4} \tag{6-9}$$

In air, since $P_{O_2}=0.2$ atm, the equilibrium constants of reactions 1 and 2 are

$$K_{p,1}=0.2P_{Li}^{4} \tag{6-10}$$

$$K_{p,2}=(0.2)^{5/4}P_{Li}^{5} \tag{6-11}$$

From the thermodynamic data in Table 6.5 and reference 106, the equilibrium vapor pressure values of lithium oxide and lithium for Li_8ZrO_6 can be calculated (Table 6.6), based on equations 6-8 to 6-11.

For the decomposition of $LiYO_2$, the reaction is

$$2LiYO_2 = Li_2O(g) + Y_2O_3 \qquad (10)$$

Then the lithium oxide vapor pressure for the decomposition of Li_2ZrO_3 and $LiYO_2$ can be calculated similarly as for Li_8ZrO_6, and the values are listed in Table 6.6.

Table 6.6. Lithium and lithium oxide vapor pressure at different temperatures for Li_8ZrO_6, Li_2ZrO_3 and $LiYO_2$

T(K)	1173	1273	1373	1473	1673	1773
P_{Li_2O}(atm)	7.86×10^{-10}	2.50×10^{-8}	4.93×10^{-7}	6.46×10^{-6}		
$P_{Li,8}$(atm)[a]	7.70×10^{-10}	1.49×10^{-8}	1.87×10^{-7}	1.67×10^{-6}		
$P_{Li,8}$(atm)[b]	5.18×10^{-12}	1.40×10^{-10}	4.00×10^{-9}	8.00×10^{-8}		
$P_{Li,9}$(atm)[a]	8.92×10^{-15}	2.53×10^{-13}	7.15×10^{-12}	1.27×10^{-10}		
$P_{Li,9}$(atm)[b]	1.78×10^{-18}	2.29×10^{-16}	1.50×10^{-14}	5.48×10^{-13}		
$P_{Li_2O,6}$(atm) (for Li_2ZrO_3)	2.21×10^{-13}	1.53×10^{11}		8.00×10^{-9}	1.14×10^{-6}	8.56×10^{-6}
$P_{Li_2O,10}$(atm) (for $LiYO_2$)	1.93×10^{-25}	2.45×10^{-18}		4.71×10^{-14}	8.41×10^{-11}	1.80×10^{-9}

a. in vacuum or an atmosphere with $P_{O_2}=0$.

b. in air.

From the previous thermodynamic calculations, it is known that reaction 1 is more favourable than the others for the decomposition of Li_8ZrO_6. Then for the lithium loss due to evaporation, only reactions 1 and 8 will need to be considered. Based on the Hertz-Langmuir expression [108] and Table 6.6, the maximum lithium loss through reactions 1, 5, 8 and 10 can be calculated as listed in Table 6.7.

Table 6.7. The maximum lithium loss rates ($g \bullet h^{-1} \bullet cm^{-2}$) for Li_8ZrO_6, Li_2ZrO_3 and $LiYO_2$ at different temperatures

T(K)	1173	1273	1373	1473	1673	1773
Li_8ZrO_6 (reaction 1)	2.00×10^{-6}	6.11×10^{-4}	1.16×10^{-2}	1.47×10^{-1}		
Li_8ZrO_6 (reaction 8 in vacuum)	9.47×10^{-6}	1.76×10^{-4}	2.13×10^{-3}	1.83×10^{-2}		
Li_8ZrO_6 (reaction 8 in air)	6.63×10^{-8}	1.65×10^{-6}	4.55×10^{-5}	8.78×10^{-3}		
Li_2ZrO_3 (reaction 5)	5.6×10^{-9}	3.74×10^{-7}		1.82×10^{-4}	2.43×10^{-2}	0.18
$LiYO_2$ (reaction 10)	4.92×10^{-21}	2.45×10^{-18}		4.71×10^{-14}	8.41×10^{-11}	1.8×10^{-9}

From reaction 8, it can be seen that 8.73 g Li_8ZrO_6 will decompose for 1 gram lithium loss and 4.07 g Li_8ZrO_6 will decompose for 1 gram lithium oxide loss from reaction 1. From

Table 6.7, it is seen that the decomposition rate of Li_8ZrO_6 through reaction 1 (into Li_2O vapour and Li_4ZrO_4) is several orders of magnitude larger than that through reaction 8 (into Li_4ZrO_4, Li vapour, and O_2 gas) in air. Therefore, the decomposition of Li_8ZrO_6 will follow reaction 1, or decompose to Li_4ZrO_4 and Li_2O gas if the temperature is not very high and the time is not very long. Table 6.7 also shows that the decomposition rate of Li_8ZrO_6 in vacuum or in atmospheres with initial $P_{O_2}=0$ through reaction 1 is also larger than the corresponding one through reaction 8.

Considering a spherical Li_8ZrO_6 crystal with initial radius of R_o, and assuming the decomposition is uniform in all radial directions and the products do not affect the reaction, the minimum time of the full decomposition of the crystal through reaction 1, (decomposed into Li_4ZrO_4 and Li_2O vapour) can be derived as follows

$$t = \varrho R_o/v \qquad (6\text{-}12)$$

where ϱ is density of Li_8ZrO_6, and v is the effusive rate of Li_2O vapour. From equation 6-12 and Table 6.7, the minimum time that a 1 gram spherical crystal Li_8ZrO_6 decomposes completely at different temperature can be calculated, as listed in Table 6.8.

Table 6.8. The minimum time for a 1 gram spherical crystal of Li_8ZrO_6 to decompose completely

temperature (K)	1173	1273	1373	1473
time (hour)	$6.5x10^4$	$2.1x10^3$	$1.1x10^2$	8.8

In the preparation of Li_8ZrO_6 by solid reactions, the temperature chosen is as high as possible in order to reduce the preparation time and get dense pure phase material. Based on Table 6.7 and 6.8, the reaction temperature in the preparation of Li_8ZrO_6 is suggested to be below 1100°C. In the present work, the solid state formation parameters of Li_8ZrO_6 from Li_2O_2 and ZrO_2 raw materials were chosen as 900°C, and 72 hours. XRD results in Fig.6.4 show that pure phase Li_8ZrO_6 was obtained after the reaction.

The decomposition experiments for Li_8ZrO_6 sintered discs with diameter 13 mm and thickness 2 to 3 mm were carried out in air at 1000 and 1200°C. The XRD results shown in Fig.6.4 indicate that the sample heated at 1200°C for 8 hours in air retains Li_8ZrO_6 as a minor phase. For the sample heated at 1000°C for 20 hours, Li_4ZrO_4 appeared. The lithium loss at

1000°C in air was measured for a sample with 13 mm diameter and 3.5 mm thickness (1.1585g). The experimental and calculated values are shown in Table 6.9. From Table 6.9, it is seen that they are close to each other though the calculated values are slightly larger. Therefore, the theoretical calculations on the thermal stability are quite successful.

Table 6.9 The experimental and calculated values of the lithium loss at 1000°C for a sintered Li_8ZrO_6 sample with 13 mm diameter and 3.5 mm thickness (1.1585g)

Time (hours)	10	20	30	50	72
Experimental (g)	0.0131	0.0231	0.0336	0.0528	0.0821
Calculated (g)	0.0168	0.0336	0.0504	0.0840	0.1210

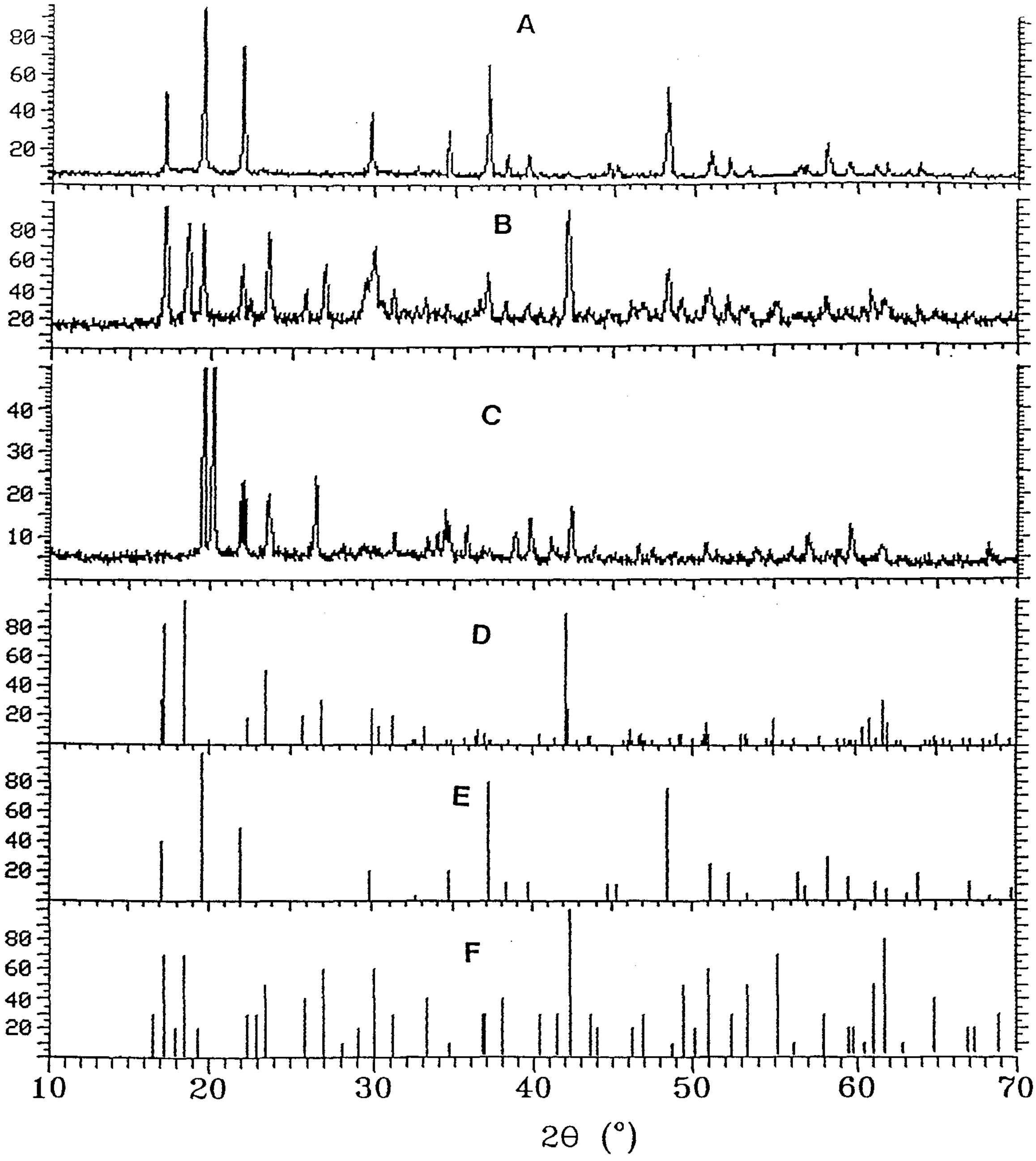

Fig.6.4 The x-ray diffraction patterns for Li_8ZrO_6 heated at different temperatures, A: before heating; B: 1000°C for 20 hours, C: 1200°C for 8 hours; D, E and F are from JCPDS cards for Li_4ZrO_4(#20-645), Li_8ZrO_6 (#26-867) and Li_2ZrO_3(#33-843), respectively.

6.2.3 Stability Against Water Vapor

Many lithium compounds tend to be attacked by water vapor in air or wet atmospheres. The worst case is the complete hydrolysis of a lithium compound to form LiOH. In order to study the stability against water vapor for lithium zirconates due to hydrolysis, the following reactions have to be considered:

$$1/2Li_8ZrO_6 + H_2O(g) = 2LiOH + 1/2Li_4ZrO_4 \quad (W1)$$

$$2/5Li_8ZrO_6 + H_2O(g) = 2LiOH + 1/5Li_6Zr_2O_7 \quad (W2)$$

$$1/3Li_8ZrO_6 + H_2O(g) = 2LiOH + 1/3Li_2ZrO_3 \quad (W3)$$

$$1/4Li_8ZrO_6 + H_2O(g) = 2LiOH + 1/4ZrO_2 \quad (W4)$$

$$Li_4ZrO_4 + H_2O(g) = 2LiOH + Li_2ZrO_3 \quad (W5)$$

$$Li_6Zr_2O_7 + H_2O(g) = 2LiOH + 2Li_2ZrO_3 \quad (W6)$$

$$Li_2ZrO_3 + H_2O(g) = 2LiOH + ZrO_2 \quad (W7)$$

$$2LiYO_2 + H_2O(g) = 2LiOH + Y_2O_3 \quad (W8)$$

From the thermodynamic data in Table 6.5 and reference 107, the standard Gibbs free energies of the above reactions were calculated and listed in Table 6.10.

Table 6.10 Standard Gibbs free energies in the reactions of lithium zirconates with water vapor

---

$\Delta G^{o}_{W1} = -78.72+1.149\times10^{-2}T-1.149\times10^{-2}T\ln(T/298)$ (kJ)

$\Delta G^{o}_{W2} = -215.10+1.149\times10^{-2}T-1.149\times10^{-2}T\ln(T/298)$ (kJ)

$\Delta G^{o}_{W3} = -75.69+1.149\times10^{-2}T-1.149\times10^{-2}T\ln(T/298)$ (kJ)

$\Delta G^{o}_{W4} = -62.15+1.149\times10^{-2}T-1.149\times10^{-2}T\ln(T/298)$ (kJ)

$\Delta G^{o}_{W5} = -69.02+1.149\times10^{-2}T-1.149\times10^{-2}T\ln(T/298)$ (kJ)

$\Delta G^{o}_{W6} = -1511+1.149\times10^{-2}T-1.149\times10^{-2}T\ln(T/298)$ (kJ)

$\Delta G^{o}_{W7} = -21.62+1.149\times10^{-2}T-1.149\times10^{-2}T\ln(T/298)$ (kJ)

$\Delta G^{o}_{W8} = 161.58+1.149\times10^{-2}T-1.149\times10^{-2}T\ln(T/298)$ (kJ)

From Table 6.10, the equilibrium water vapor pressure for the lithium zirconates in the above reactions can be calculated as listed in Table 6.11.

Table 6.11 The equilibrium water vapor pressure for lithium zirconates and yttrate

P_{H2O} T(K)	298	373	473	673	773	873
P_{W1}(atm)	$6.29\text{x}10^{-14}$	$8.22\text{x}10^{-10}$	$2.21\text{x}10^{-6}$	$1.24\text{x}10^{-2}$	$1.67\text{x}10^{-1}$	0.21
P_{W2}(atm)	$1.27\text{x}10^{-37}$					
P_{W3}(atm)	$2.16\text{x}10^{-13}$	$3.00\text{x}10^{-9}$	$4.82\text{x}10^{-6}$	$2.15\text{x}10^{-2}$	0.27	0.76
P_{W4}(atm)	$5.07\text{x}10^{-11}$	$2.30\text{x}10^{-7}$	$1.57\text{x}10^{-5}$	0.26	1.01	
P_{W5}(atm)	$2.58\text{x}10^{-12}$	$4.60\text{x}10^{-8}$	$2.30\text{x}10^{-7}$	$6.43\text{x}10^{-2}$	0.70	4.30
P_{W6}(atm)	$5.13\text{x}10^{-265}$					
P_{W7}(atm)	$6.56\text{x}10^{-4}$	$9.06\text{x}10^{-2}$	5.35			
P_{W8}(atm)	$6.87\text{x}10^{57}$					

In air, the typical water vapor pressure is $1.0\text{x}10^{-2}$ atm. The Gibbs free energies of reactions W1 to W8 based on this value are listed in Table 6.12.

Table 6.12 The Gibbs free energies of the reactions of lithium zirconates with water vapor in air with P_{H_2O}=0.01 atm

T(K)	298	373	473	673	873
ΔG^o_{W1}(kJ)	-127.9	-101.3	-66.4	2.2	69.3
ΔG^o_{W2}(kJ)	557.6	592.1	629.6	709.0	786.2
ΔG^o_{W3}(kJ)	-182.6	-147.8	-90.3	12.5	113.1
ΔG^o_{W4}(kJ)	-234.9	-132.7	-65.7	72.1	205.4
ΔG^o_{W5}(kJ)	-54.7	-38.2	-24.1	10.3	43.9
ΔG^o_{W6}(kJ)	-1481	-1463	-1440	-1393	-1346
ΔG^o_{W7}(kJ)	-6.78	6.78	24.6	59.6	93.9
ΔG^o_{W8}(kJ)	170.7				

Table 6.11 can be used to predict whether lithium zirconates are attacked by water vapor in specific situations and also to indicate the final products of the reaction of lithium zirconate with water vapor. This information is very useful for the preparation, processing and applications of lithium zirconates.

From Tables 6.10, 6.11 and 6.12, it is known that if the partial pressure of water vapor is larger than 6.29×10^{-14} atm, Li_8ZrO_6 will be thermodynamically unstable with regard to water vapor at room temperature. At 400°C, Li_8ZrO_6 will unstable when the partial pressure of water vapor is larger than 0.0124 atm. In air, since the water vapor content is quite variable up to 5% (vol), Li_8ZrO_6 could be unstable in air even at 400°C. However, Li_8ZrO_6 should be stable against water vapor in air when the temperature is above 500°C.

From Tables 6.10, 6.11 and 6.12, it is also known that at room temperature the final products in the reaction of Li_8ZrO_6 with water vapor in air will be ZrO_2 and LiOH (in fact LiOH will react with CO_2 and form Li_2CO_3). Tables 6.10, 6.11 and 6.12 also show the $LiYO_2$ is thermodynamically stable against water vapor even at room temperature. In order to know whether $LiYO_2$ is stable in an environment with a combination of CO_2 and water vapor, consider the following reaction:

$$2LiYO_2 + H_2O(g) + CO_2 = Li_2CO_3 + Y_2O_3 + H_2O(l)$$

From the thermodynamic data in Table 6.5 and reference 107, we obtain a standard Gibbs free energy of 156.7 kJ at 298 K, and an entropy change less than 0. The Gibbs free energy will be even more positive at higher temperature. Therefore, $LiYO_2$ is thermodynamically stable in an environment of both CO_2 and water vapor.

The hydrolysis rate of Li_8ZrO_6 and yttrium-doped Li_8ZrO_6 in air at room temperature was studied by the weight-gain experiment. The hydrolysis products were studied by XRD, IR spectra and DTA. The dependence of the relative weight-gain values of these materials on time are shown in Fig.6.5. The XRD patterns for samples of Li_8ZrO_6 before and after exposure to air are shown in Fig.6.6. It seen that the background of the patterns for the samples exposed to air are raised, and the extra peaks appear, but the phases are very difficult to determine except Li_8ZrO_6 itself. However, the IR spectra and DTA results show that LiOH and Li_2CO_3 are present in the samples.

From Fig.6.5, it is seen that the rate of weight increase in the fresh sample is much larger than that in the sample stored in dry air for 2 months. This may be caused by the fact that Li_8ZrO_6 will form a compact layer of carbonate on the surface during the stored period to protect it from attack by water vapor when exposed to air. It is also seen that the rates of weighs gain for samples of yttrium-doped Li_8ZrO_6 are smaller than that of pure Li_8ZrO_6.

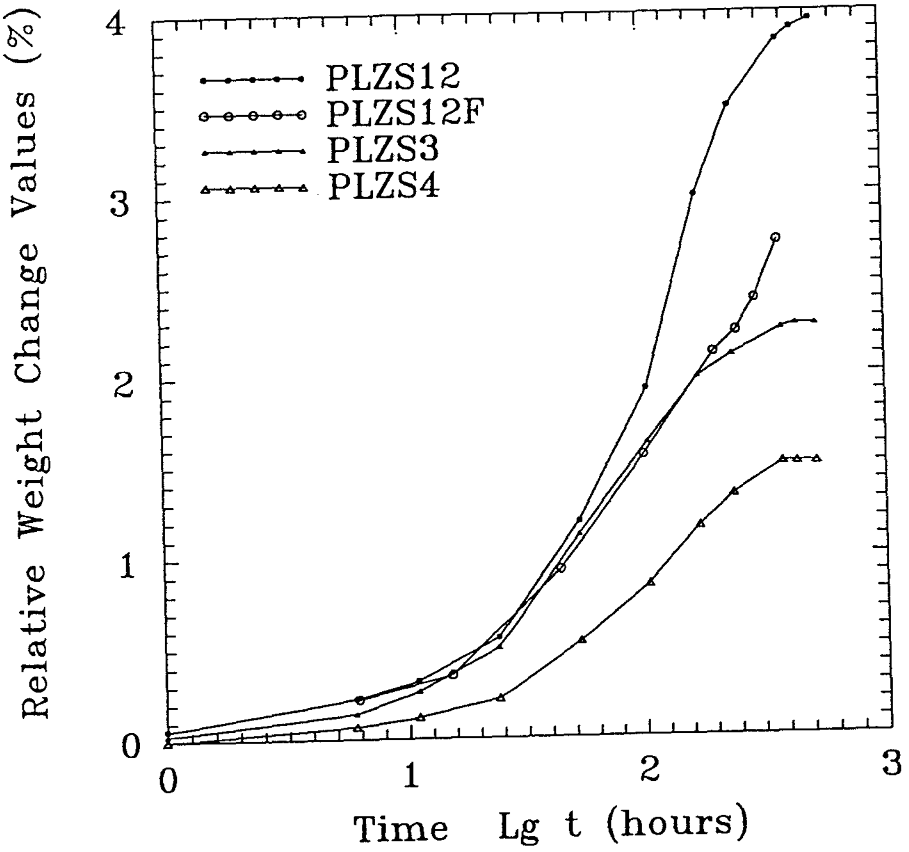

Fig.6.5 The dependence of the relative weight-increase values on time in air for yttrium-doped $Li_8ZrO_6(Li_{8+x}Y_xZr_{1-x}O_6)$ stored in dry air for several months, PLZS12 withx=0, PLZS3 with x=0.05, PLZS4 with x=0.1, where PLZS12F is fresh sample without yttrium and the weight-increase values were multiplied by 0.1.

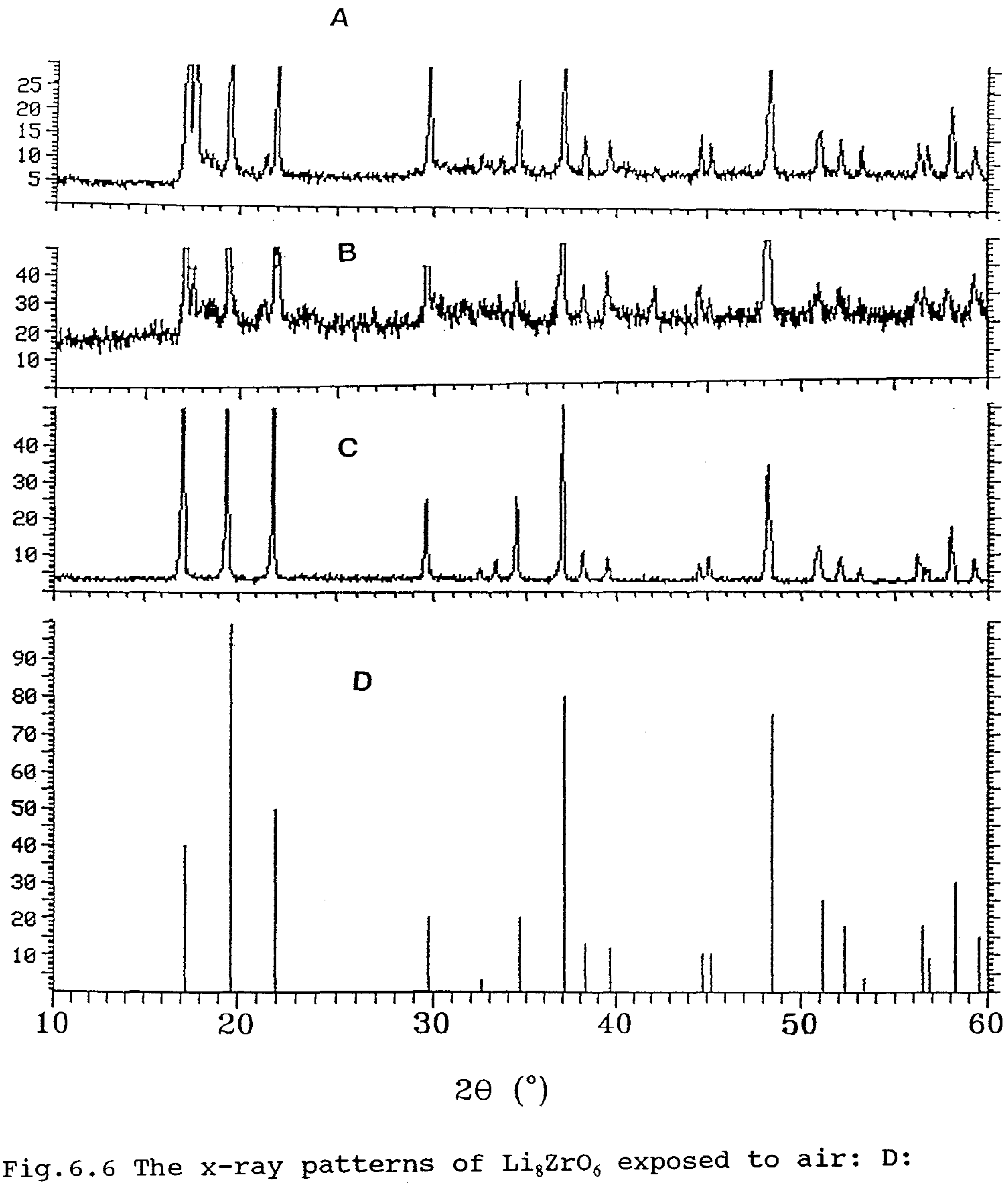

Fig.6.6 The x-ray patterns of Li_8ZrO_6 exposed to air: D: JCPDS card for Li_8ZrO_6(#26-867); C: before exposing to air; B: after 24 hours, A: after 440 hours using a sample stored in dry air for several months.

CHAPTER 7 CONCLUSION

From the previous experimental results in chapter 5 and discussions in chapter 6, it is known that the conductivities of yttrium-doped Li_2ZrO_3 and Li_8ZrO_6 are not significantly improved relative to corresponding pure Li_2ZrO_3 and Li_8ZrO_6 and the conductivities of zirconium-doped $LiYO_2$ are much lower than pure $LiYO_2$. However, a number of important results have been derived in this investigation and the following conclusions can be drawn :

1. With small amounts of yttrium substitution for zirconium in Li_2ZrO_3, a solid solution can be formed. The solubility in the solution of $Li_{2+x}Y_xZr_{1-x}O_3$ is x is not larger than 0.05, whereas at x=0.1, a small amount of $Li_6Zr_2O_7$ second phase will appear. The lattice parameters increase slightly with the amount of dissolved yttrium.

2. The formation of the solid solution can improve significantly the sinterability of Li_2ZrO_3, and the density of the ceramic samples increases from 80.8% to 94.6% theoretical density as x varies from 0 to 0.05. For the sample with x=0.1, the density reaches 99.4% theoretical density.

3. The total lithium ion conductivity of the ceramic samples of solid solution $Li_{2+x}Y_xZr_{1-x}O_3$ increases slightly from 3.93×10^{-6} to 5.04×10^{-6} S/cm at 400^0C as x varies from 0 to 0.05, and the activation energy decreases slightly from 0.99 to 0.92 Ev over the same range of the composition. For the sample with x=0.1, the total conductivity decreases relative to the sample with x=0.05 because of the effects of the second phase. From the estimation based on the effective medium theory, the lithium ion conductivity of the solid solution $Li_{2+x}Y_xZr_{1-x}O_3$ increases by only 1% and 3% for x=0.01 and 0.05, respectively, compared with Li_2ZrO_3. Generally, the lithium ion conductivity is not significantly enhanced by doping with Y_2O_3.

4. When small amount of yttrium is introduced into octalithium zirconate to substitute some zirconium, a solid solution of yttrium-doped octalithium zirconate forms. The solubility in the solution of $Li_8Y_xZr_{1-x}O_6$ is $0.05 \leq x < 0.1$ via conventional solid reactions. The cell constant parameters in the hexagonal structures for the solid solution change slightly with the dissolved amount of yttrium.

5. In the processing and conductivity measurements of the yttrium-doped solid solution in air and the mixture of the solid solution with $LiYO_2$, the materials will absorb some water vapour and carbon dioxide from air and form some mixture of LiOH($LiOH.H_2O$) and Li_2CO_3, which melts at around 430°C. The

mixture affects significantly the lithium conductivity behaviours of the materials.

6. The electronic contribution to the conductivity in the materials is less than 1% below 435°C.

7. The lithium conductivity at 435°C in the solid solution increases from 1.0×10^{-2} to 6.9×10^{-2} S/cm with the dissolved amount of yttrium increasing from 0 to 5%. At 10% yttrium addition, the lithium conductivity decreases because of the second phase effects of $LiYO_2$.

8. The yttrium doped octalithium zirconate materials are suggested to be potential solid electrolytes for Li/S batteries and high temperature lithium batteries at operating temperatures around 435°C.

9. With zirconium substitution for yttrium in $LiYO_2$, solid solutions of Zr-doped $LiYO_2$ can be formed. The solubilities are $x\leq0.1$ in the solution of $Li_{1+x}Zr_xY_{1-x}O_2$ and $x\geq0.3$ in the solution of $Li_{1+x}Zr_xY_{1-x}O_{2+x}$. The crystal structures are changed from monoclinic for pure $LiYO_2$ to tetragonal for Zr-doped solid solutions.

10. The electronic contribution to the total conductivity is less than 1% in the pure and Zr-doped $LiYO_2$ till 500°C.

11. The lithium ion conductivity at 500°C for pure $LiYO_2$ is quite high (1.2×10^{-2} S/cm), but the conductivity for

ceramic Zr-doped $LiYO_2$ decreases drastically from $1.3x10^{-2}$ to $1.2x10^{-4}$ S/cm at 500°C as x increases from 0 (pure $LiYO_2$) to x=0.3 in the solution, while the ionic conduction activation energy increases significantly from 0.68 to 0.92 Ev with x increasing from 0 to 0.3.

12. Based on the Neumann-Kopp rule and the third law, the results of the calculations for thermal stability of Li_8ZrO_6 are in good agreement with the experimental ones.

13. Li_8ZrO_6 will decompose rapidly above 1100°C. But, it is stable, or decomposes very slowly below 900°C. Li_3ZrO_3 will decompose fast above 1500°C, but it is stable below 1200°C. $LiYO_2$ is thermally stable till 1500°C.

14. Li_8ZrO_6 is thermodynamically unstable against water vapor in the air with more than 1% (vol) water vapor below 400°C and Li_2ZrO_3 is thermodynamically unstable against water vapor at room temperature, while $LiYO_2$ is thermodynamically stable against water vapor even in an environment with a combination of water vapor and CO_2 at room temperature. But, Li_8ZrO_6 will be stable against water vapor above 500°C in air. The hydrolysis rate of Li_8ZrO_6 stored in dry air for long periods is much slower than that of the fresh samples. Also the rate of hydrolysis of yttrium doped Li_8ZrO_6 solid solutions is slower that of pure Li_8ZrO_6.

15. The temperature for the synthesis and preparation

in air of Li_8ZrO_6 should be in the range of 500 to 1100°C in order to obtain pure phase Li_8ZrO_6. In processing of Li_8ZrO_6 in air, the temperature also should be in this range in order to prevent its decomposition and hydrolysis.

CHAPTER 8 FUTURE WORK

In this investigation, the focus has been on forming new lithium ion conductors in the LiO_2-Y_2O_3-ZrO_2 system by doping lithium zirconates and lithium yttrate and studying the structures, conductivities and thermodynamic stabilities. There was little emphasis on the ion conduction mechanisms and applications of these materials. A number of topic are suggested for future work:

1). Further analyzing ac impedance results by curve fitting to get the grain conductivity and conduction activation energy data, then establishing lithium ion conduction models for lithium zirconates and lithium yttrate based on the crystal structures and conductivity data. This is very useful for exploring new lithium ion conductors and also for improving the lithium conductivity in these materials.

2). Fabricating Li probes with Y-doped or pure Li_2ZrO_3 and Li_8ZrO_6 and pure $LiYO_2$ and testing the properties of lithium alloys.

3). Fabricating galvanic cells of using Y-doped Li_8ZrO_6 and pure $LiYO_2$ ion conductors to measure their dynamic properties.

4). Testing the radiation properties of pure $LiYO_2$ and tritium invention property to verify whether it can be used in applications for tritium blankets in a fusion reactor.

5). Exploring new lithium ion conductors in the Li_2O-Al_2O_3-ZrO_2 and Li_2O-Al_2O_3-Y_2O_3 systems since Li_5AlO_4 is also a lithium ion conductor thermodynamically stable in the presence of pure Li.

REFERENCES

1. E. J. Cairns and J.S. Dunning, Pro. and Workshop on Adv. Battery Research and Design, ERDA-ECS Report No. ANL-76-8, Argonne National Laboratory(1976).
2. R.K. Stenunenberg, Lithium/Metal Sulphide Battery Development, in " Fast Ion Transport in Solids, Eds by P. Vashishta, J.N. Mundy and G.K. Shenoy, Elsevier North Holland Inc., 1979, P23.
3. J.R. Birk and R.K. Steunenberg in New Users of Sulphur, J.R. West, ed., Adv. Chem. Ser. 140, ACS, Washington (1975).
4. M.V. Smirnov and N.P. Padlesnyak, Zh. Prikl. Khim. 43, 1463(1970).
5. N. Watanabe, Kogyo Kagaku Zasshi, 71, 1599(1968).
6. R.N. Seefurth and R.A. Sharma, J. Electrochem. Soc., 122, 1049(1975).
7. R.C. Weast, S.M. Selby, and C.D. Hodgman, eds., Handbook of Chemistry and Physics, 45th Ed., Chemical Rubber Co., Cleveland (1964).
8. E.E. Hellstrom and W. Van Gool, Rev. Chim. Minerale, 17, 263 (1980).

9. S. Chandra, in " Superionic Solids Principles and Applications", North-Holland Publishing Co., Amsterdam, 1981, P23.

10. R.A. Huggins, J. Electrochem. Soc., 118, 79(1971).

11. D.N. Bose and D. Majumdar, Bull. Mater. Sci., 6, 223(1984).

12. J.T.S. Irvine and A.R. West, in " High Conductivity Solid Ionic Conductors, Recent Trends and Applications", Takehiko Takahashi, Editor, World Scientific, Singapore, 1989, P.201.

13. Tetsuichi Kudo and Kazuo Fueki, in" Solid State Ionics", Kodansha Ltd., Tokyo(Japan), 1990, p90.

14. E. Warburg, F. Togetmeier , Wiedemann Ann. Phys., 32, 455 (1888).

15. W. Nernst, Z. Electrochem., 6, 41(1899).

16. C. Wagner, Naturwissenschaften, 31, 265(1943).

17. C. Tubandt, Z. anorg. allgem. chem., 115, 105(1921).

18. C. Tunandt, H. Reinhold, Z. Electrochem., 29, 313(1923).

19, L. W. Strock, Z. phys. chem., B31, 132(1935).

20. A. Joffe, Ann. Phys.(Leibzig), 72, 461(1923).

21. J. Frenkel, Z. Phys., 35, 652(1926).

22. C. Wagner, W. Schottky, Z. Phys. Chem., B11, 163(1930).

23. J. N. Bradly, P. D. Green, Trans. Faraday., 62, 2069 (1965).

24. J. B. Goodenough, H. Y. P. Hong, I. A. Kafalas, Mat. Res.

Bull., 11, 203 (1976).

25. N. Weber, J. T. Kummer, Proc. Ann. Power Sources Conf., 21, 37 (1967).
26. A. Benrath and K. Drekopf, Z. Phys. Chem., 99, 57 (1921).
27. S. Pizzini, J. Appl. Electrochem., 1, 153 (1971).
28. U. Van Alpen, A. Rabenau, and G. H. Talat, Appl. Phys. Lett., 30, 621 (1977).
29. A. Kvist and A. Lunden, Z. Naturforsch., 20a, 235 (1965).
30. A. Kvist, Z. Naturforsch., 21a, 1221 (1966).
31. A. Lunden, Solid State Ionics, 25, 231 (1987).
32. V. K. Deshpande, and K. Singh, Solid State Ionics, 6, 151 (1982).
33. P. G. Bruce and A. R. West, J. Solid State Chem., 44, 354 (1982).
34. J. G. Kamphorst, and E. E. Hellstrom, Solid State Ionics, 1, 187 (1980).
35. U. Von Alpen, M. F. Bell, W. Wichelhaus, K. Y. Cheung and Dudley, Electrochim. Acta, 23, 1395 (1978).
36. Y. M. Polezhaev and V. G. Chnukhlantsev, J. Inorg. Mater., 1, 718 (1965).
37. R. Scholder, D. Rade and H. Schwarz, Z. anorg. allg. chem., 362, 149 (1968).
38. L. Enreguez, Trans. Br. Ceram. Soc., 81, 17 (1982).
39. G. Dittrich and R. Hoppe, Z. anorg. allg. chem., 371, 306 (1969).

40. B. Rasneur, A. J. Flipot, E. Brauns, and P.H. Diels, in "Fabrication and Properties of Lithium Ceramics II," Glenn W. Hollenberg and Ian J. Hastings, Editors, The American Ceramic Society, Inc., Westerville, Ohio, 1990, p. 63.

41. C. E. Johnson, C.H. Wu, N Huet, L. Montanaro, C. Alvani, J.P. Lecompte, and A. Negro. in "Ceramics Today-Tomorrow's Ceramics", P. Vincenzini, Editor, Elsvier Science Publishers B.V., 1991. Pro. of 7th International Meeting on Modern Ceramic Technologies, Montecatini, Terme, Italy, 1990. p.3029.

42. P. Kennedy, S. Broughton and S.D. Preston, in "Ceramics Today-Tomorrow's Ceramics", P. Vincenzini, Editor, Elsevier, 1991. Proc. of 7th International Meeting on Modern Ceramic Technologies, Montecatini, Terme, Italy, 1990, p.3059.

43. Von R. Hoppe and R. M. Braun, Z. anorg. allg. chem., 433, 181 (1977).

44. A. Neubert and D. Guggi, J. Chem. Thermodynamics, 10, 297 (1978).

45. C. Delmas, A. Maazaz, F. Guillen, C. Fouassier, J.M. Reau and P. Hagenmuller, Mater. Res. Bull., 14, 620 (1979).

46. R.M. Biefeld and R.T. Johnson, Jr., J. Electrochem. Soc., 126, 1 (1979).

47. E. F. Bertaut and M. Gondrand, Compt. Rend., 225, 1135 (1962).

48. C. F. Stewner and R. Hoppe, Z. anorg. allg. chem., 380, 250 (1971).

49. G. Herzberg, "Molecular Spectra and Molecular Structure", Part II, Van Nostrand-Reinhold, Princeton, New Jersey, 1945.

50. R. N. Jones and C. Sandorfy, in "Chemical Applications of Spectroscopy", W. West, ed., Vol. IX, Chapter IV, Wiley Interscience, New York, 1956.

61. A. B. F. Duncan, in "Chemical Applications of Spectroscopy", W. West, ed., Vol.IX, Chapter III, Wiley Interscience, New York, 1956.

52. L. J. Bellamy, "The Infrared Spectra of Complex Molecules", Acedemic Press, New York, 1964.

53. C. N. R. Rao, "Chemical Applications of Infrared Spectroscopy", Acedemic Press, New York, 1964.

54. N. B. Colthup, L. H. Daly, and S. E. Wiberley, "Introduction to Infrared and Raman Spectroscopy", Academic Press, New York, 1964.

55. L. J. Bellamy, "Advances in Infrared Group Frequencies", Methuen, London, 1968.

56. H. Siebert, "Anwendungen der Schwingungsspektroskopie in der Anorganischen Chemie", Springer, Berlin, 1966.

57. S. D. Ross, Inorganic Infrared and Raman Spectra, McGraw-Hill, London, 1992.

58. V. C. Farmer, in"The Infrared Spectra of Minerals",

Mineral Soc. London, 1974.

59. A. N. Lazarev, "Vibrational Spectra and Structure of Silicates", Consultants Bureau, New York, 1972.

60. J. E. Bauerle, J. Phys. Chem. Solids, 30, 2657 (1969).

61. J. R. MacDonald, J. Chem. Phys., 61, 3977 (1974).

62. J. R. MacDonald, in "Solid State Ionics", M. Kleitz and J. Dupuy, D. Reidel, eds., Dordrecht/Boston, 1976, p.149.

63. A. K. Jouscher, J. Mater. Sci., 13, 553 (1978).

64. J. R. MacDonald, in "Superionic Conductors", G. D. Maham and W. L. Roth, eds., Plenum Press, New York, 1976, p.81.

65. E. Schouler, M. Kleitz and C. Deportes, J. Chim. Phys., 70, 923 (1973).

66. E. Schouler, G. Giroud, and M. Kleitz, Mater. Res. Bull., 11, 1137 (1976).

67. S. H. Chu and M. A. Seitz, J. Solid State Chem., 23, 1137 (1976).

68. A. Hooper, J. Phys. D: App. Phys., 10, 1487 (1977).

69. R. D. Armstrong and R. Mason, J. Electroanal. Chem., 41, 231 (1973).

70. R. W. Powers and S. P. Mitoff, J. Electrochem. Soc., 122, 226 (1975).

71. R. D. Armstrong, in "Solids State Ionics", M. Kleitz, J. Dupuy, and D. Reidel, eds., Dordrecht/Boston, 1976, p.261.

72. S. R. De Groot, "Thermodynamics of Irreversible Processes", North-Holland, Amsterdam, 1951.

73. K. S. Cole and R. H. Cole, J. Chem. Phys., 9, 341 (1941).

74. M. Kleitz and J. H. Kennedy, in" Fast Ion Transport in Solids", P. Vashishta, J. N. Mundy and G. K. Shenoy, eds., North-Holland, Amsterdam, 1979, p.185.

75. R. A. Nyquist and R.O. Kagel, in " Infrared Spectra of Inorganic Compounds," R.A. Nyquist and R.O. Kagel, Editors, Academic Press, New York, 1971. p.10.

76. J.O. Isard, Solid State Ionics, 31, 187 (1988).

77. J.O. Isard, D. Kruschke, and W. Muller, Solid State Ionics, 45, 157 (1991).

78. D.R. Franceschetti and J.R. MacDonald, J. Electroanal. Chem., 53, 1 (1974).

79. J.R. MacDonald and J.A. Garber, J. Electrochem. Soc., 124, 1022 (1977).

80. Van R. Hoppe and R.M. Braun, Z. Anorg. Allg. Chem., 433, 181 (1977).

81. S. Konishi, H. Ohno, T. Hayashi, and K. Okuno, Diffusion of Lithium and Tritium in Li_8PbO_6, in "Fabrication and Properties of Lithium Ceramics II", Glenn W. Hollenberg and Ian J. Hastings, Editors, The America Ceramic Society, Inc., Westerville, Ohio, 1990, p.173.

82. P.D. Dernier, and J.P. Remeiks, J. Solid State Chem., 17, 245 (1976).

83. J. Antoine, D. Vivien, J. Livage and J. Thery, Mater. Res.

Bull., 10, 865 (1976).

84. R. Collongues, J. Thery, J.P. Boilot, β-alumina in " Solid Electrolytes, General Principles, Characterization, Materials and Applications", Paul Hagenmuller and W. Van Gool, Academic Press, 1978, p.271.

85. L.H. Jones, J. Chem. Phys., 22, 217 (1954).

86. K.A. Wickersheim, J. Chem. Phys., 31, 863 (1959).

87. R.M. Hexter, J. Chem. Phys., 34, 941 (1961).

88. E. Drouard, Compt. rend., 249, 665 (1959); 247, 68 (1958).

89. R.A. Nyquist and R.O. Kagel, in "Infrared Spectra of Inorganic Compounds", Acedemic Press, New York, 1971.

90. "Standard Infrared Prism Spectra", vol. 87, edited and published by Sadtler Research Laboratories, Division of Bio-Red Laboratories, Inc., USA, 1987, No 72728.

91. " Handbook of Preparative Inorganic Chemistry", vol. 1, 2nd ed., Georg Brauer, ed., Reed F. Riley, translated ed., Acedemic Press, New York, 1983, p.983.

92. Lawrence P. Cook and Howard F. McMurdie, eds., "Phase Diagrams for Ceramists", vol.VII, the American Ceramic Soc., Inc., 1989, p.66.

93. Von F. Stewner and R. Hoppe, Z. anorg. allg. chem., 380, 250 (1977).

94. E. F. Bertaut and M. Gondrand, C.R. hebd. Seances Acad. Sci., 225, 1135 (1962).

95. E. E. Hellstrom and W. Van Gool, Solid State Ionics, 2, 59

(1981).

96. H.J. Juretchke, R. Landauer, and J.A. Swanson, J. Appl. Phys., 27, 838 (1956).
97. M.H. Cohen, Phys. Rev. Lett., 30, 696 (1973).
98. C. Bertone, J. Nucl. Mater., 151, 281 (1986).
99. W. Breitung, H. Elbel, J. Lebkucher, G. Schumacher, and H. Werle, J. Nucl. Mater., 155-157, 507 (1988)
100. S. Konishi and H. Ohno, J. Nucl. Mater., 152, 9 (1988).
101. H. Ohno, S. Konishi, T. Nagasaki, T. Kurasawa, and H. Watanabe, J. Nucl. Mater., 133 & 134, 181 (1985).
102. C. E. Johson, K. R. Kummerer, E. Roth, J. Nucl. Mater., 155-157, 188 (1988).
103. R.T. Johnson, Jr., R.M. Biefeld and J.D. Keck, Mater. Res. Bull., 12, 577 (1977).
104. "Thermodynamics of Solids", Richard A. Swalin, ed., John Wiley & Sons, 1972, p.83.
105. O. Kubashewski, C. B. Alcock and E. Evans, "Metallurgical Thermochemistry", 4th ed., Pergamon, London, 1967, p.328.
106. "Lange's Handbook of Chemistry", John A. Dean, Norbert Adolph Lange, eds., McGraw-Hill Book Co., 1985.
107. A. W. Searay, W. S. Williams and P. O. Schissel, J. Chem. Phys., 32, 957 (1960).
108. "Thermodynamics of Solids", R. A. Swalin, ed., John Wiley & Sons, 1972, p.117.